Magnetic resonance and Stark spectroscopy of Coulomb bound states

Kamila Yunusova

NNT : 2019SACLS547

Magnetic resonance and Stark spectroscopy of Coulomb bound states

Thèse de doctorat de l'Université Paris-Saclay
préparée à l'Université Paris-Sud

École doctorale n°564 Physique en Île de France (EDPIF)
Spécialité de doctorat : physique

Thèse présentée et soutenue à Orsay, le 16 décembre 2019, par

KAMILA YUNUSOVA

Composition du Jury :

Patrice Bertet Directeur de recherche, CEA Saclay	Président
Mark Oxborrow Professeur, Department of Materials, Imperial College	Rapporteur
Marek Potemski Directeur de recherche, LNCMI, UMR 3228	Rapporteur
Michel Dyakonov Professeur, Laboratoire Charles Coulomb, UMR 5221	Examinateur
Hélène Bouchiat Directrice de recherche, LPS Orsay, UMR8502	Directrice de thèse
Alexei Chepelianskii Directeur de recherche, LPS Orsay, UMR8502	Co-encadrant

Thèse de doctorat

Magnetic resonance and Stark spectroscopy of Coulomb bound states

Kamila M. Yunusova

Synthèse en français

Dans cette thèse, nous présentons l'étude de deux systèmes de nature différente mais dont la physique dans les deux cas est dominée par les interactions coulombiennes: les excitons dans les photoconducteurs organiques dont le spin peut être manipulé par un champ magnétique et les électrons à 2 dimensions sur l'hélium liés à leur charge d'image et dont le moment dipolaire est fortement couplé au champ électrique. Nous montrerons dans les deux cas que des modèles simples de mécanique quantique permettent de bien comprendre leurs propriétés physiques. Cette thèse est divisée en deux parties. Dans la première partie, nous étudions la structure fine des bi-excitons et les aspects géométriques de leur formation dans les semi-conducteurs organiques. Dans la deuxième partie, nous démontrons une nouvelle façon de réaliser un système électrodynamique quantique (QED) d'un atome en interaction avec un oscillateur. En dépit des systèmes physiques différents explorés, les deux sujets sont liés par les méthodes spectroscopiques expérimentales développées dans cette thèse.

Les matériaux présentant de la fission d'excitons singlets en deux excitons triplets présentent une grande richesse de phénomènes physiques, liés à la diffusion et l'annihilation, leur couplage par interactions dipolaires et d'échange. Nous présentons ici des études approfondies de la physique du spin du TIPS-tétracène liées à la formation de bi-excitons après la fission de singlets. Nous nous sommes concentrés sur deux aspects de la composition du spin dans le TIPS-tétracène. Dans un premier temps, nous présenterons des études de couplage intra-triplet. Pour cela, nous avons utilisé la résonance magnétique détectée optiquement, afin de sonder les différentes espèces de spin et de suivre leur évolution en fonction des paramètres physiques pertinents.

En effet, en utilisant une technique de résonance électronique détectée optiquement "ODMR" relativement simple et peu couteuse, on peut avoir directement accès aux principales interactions intervenant dans le couplage dipôlaire entre les excitons et dans leur dynamique. Cette interaction est de très faible amplitude et a typiquement une portée de quelques nanomètres. Nous avons effectué ces expériences d'ODMR en champ magnétique nul permettant de mettre en évidence des états excitoniques triplet ou quintets dont la dégénerescence en champ nul est levée par des effets de champ cristallin caractérisés par les échelles d'énergie $D_t = 1.414$ GHz et $E_t = -10.3$ MHz dans le cas d'excitons triplet, $D_q = 482.1$ MHz et $E_q = 22.3$ MHz pour les bi-excitons quintets mesurées ainsi pour la première fois. La détermination du spectre de ces différents états en champ magnétique nul constitue une sonde très sensible de la structure des molécules (Fig. 1).

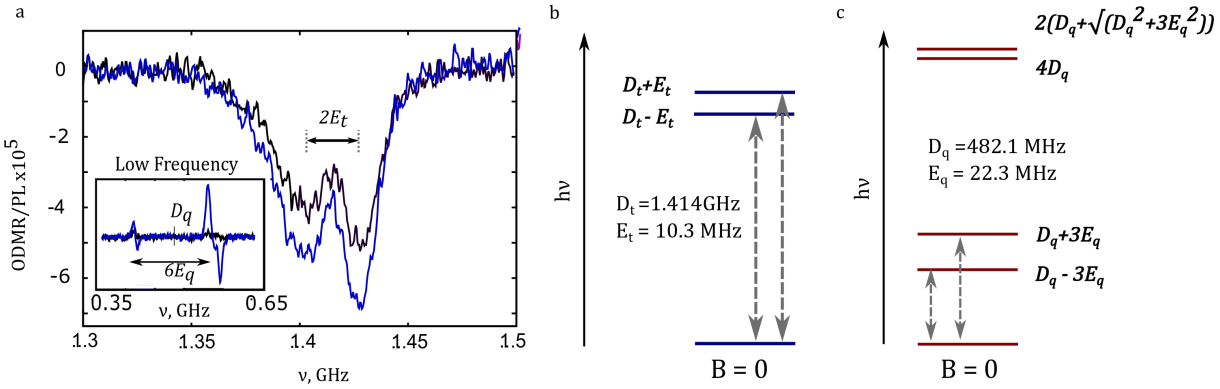

Figure 1: **a** Spectre de résonance magnétique détectée optiquement mesuré en champ magnétique nul (composante en phase en bleu, hors phase en noir). La différence en énergie des deux transitions triplets voisines est donnée par le paramètre de structure fine E, alors que le centre des deux transitions donne le paramètre D. **Insert**: Transitions à basse fréquence du bi-exciton quintet avec les valeurs des paramètres de structure fine (D_q, E_q). **b,c** Diagramme énergétique des niveaux triplet et quintet à champ magnétique nul montrant la position des niveaux en fonction des paramètres de structure fine D et E obtenue à partir de l'expérience.

En utilisant la différence existant entre la cinétique de spin des excitons triplets et quintets nous avons réussi à séparer leurs spectres et ainsi déterminer les paramètres caractéristiques de ces deux familles excitoniques. La détermination du couplage dipôlaire entre états triplets nous a permis de déterminer de façon non ambigüe la morphologie des molécuales dans le TIPS-tetracene. En particulier, l'orientation dipôlaire des états triplets par rapport a un champ magnétique extérieur a pu être déterminée et permet une caractérisation directe du désordre. Alors que la compréhension des états triplets était déjà bien avancée nous avons pu explorer en plus grand détail la formation des états quintets constitués de bi-excitons triplets.

Pour cela nous avons développé à la fois les outils théoriques et expérimentaux permettant de relier la structure inter-moléculaire à la localisation de ces bi-excitons. Tout d'abord nous avons confirmé la nature de l'état de spin $S = 2$ de ces bi-excitons par l'analyse des spectres ODMR. Outre leurs dynamiques différentes donnant lieu à des signaux séparables en phase après modulation du champ radiofréquence à une fréquence adéquate, les transitions triplet et quintet se comportent différemment en champ magnétique du à leurs multiplicités différentes. L'ajustement des spectres dans une large gamme de champ magnétique permet d'extraire les paramètres de leurs hamiltoniens respectifs.

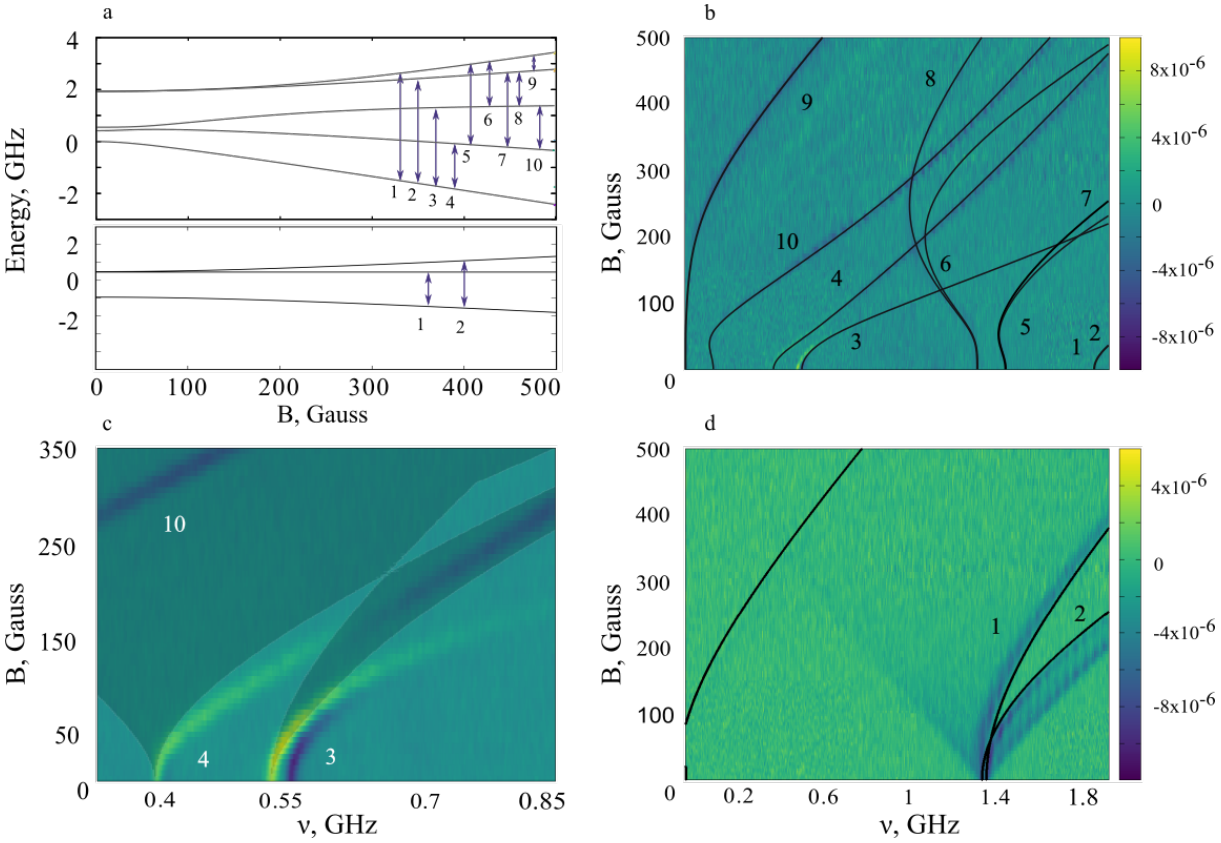

Figure 2: **a** Énergies des transitions entre les sous niveaux magnétiques de l'exciton triplet et du bi-exciton quintets en fonction du champ magnétique B. Les flèches indiquent les transitions qui correspondent au lignes numérotées dans les sous figures (b) et (d). **b** Carte bi-dimensionnelle de la réponse ODMR en fonction de la fréquence d'excitation et du champ magnétique avec sur imposée la dépendance théorique des énergies de transition en fonction du champ magnétique. **c** Agrandi de la carte ODMR à basse fréquence autour des transitions 3, 4 et 10 de la sous-figure (a) mesure à forte puissance micro-onde. Les zones avec un ombrage correspondent à la région où l'énergie de transition peut correspondre à une transition entre sous niveaux triplets reproduisant l'énergie de la transition à champ nul. Les positions des transitions expérimentales dépassent clairement les zones ombrées montrant qu'elles ne correspondent pas à un état triplet. **d** Composante hors phase de la carte ODMR, montrant les transitions triplet avec en sur-imposition l'énergie des transitions théoriques en noir.

Nous avons utilisé les paramètres caractéristiques du tenseur décrivant le couplage dipôlaire des états quintets obtenus à partir des expériences en champ magnétique nul pour obtenir l'orientation de l'axe dipôlaire par rapport à celui du champ magnétique caractérisé par les angles pôlaire et azimuthal θ et ϕ comme paramètres de fit des expériences en champ variable. Les valeurs trouvées sont $\phi = 30°$, et $\theta = 90°, \pm 5°$. Un très bon accord entre théorie et expérience a été obtenu pour ces fits (Fig. 2).

De plus, en confrontant la caractérisation structurale des cristaux moléculaires de TIPS-tetracene par rayons X avec nos résultats obtenus pour différentes orientations de champ magnétique, nous avons pu à partir des calculs des paramètres du tensor dipôlaire sur les différents appariements possibles de sites moléculaires, réussi à déterminer la géométrie et la localisation exacte des sites moléculaires des bi-excitons quintets contribuant aux signaux ODMR mesurés. (Fig. 3).

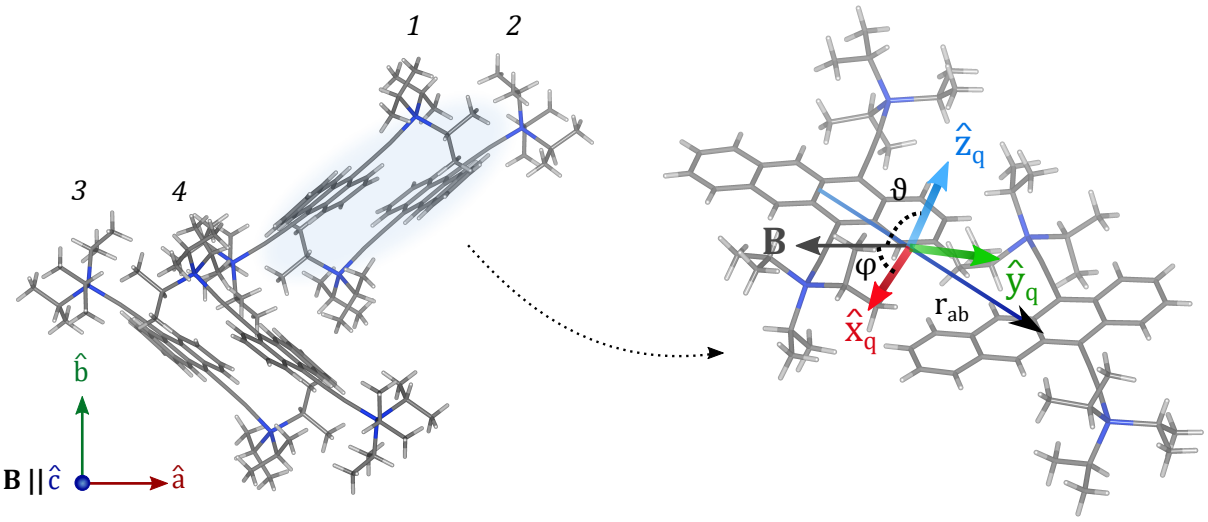

Figure 3: Orientation de échantillon 2. **a** Cellule cristalline du TIPS-tetracene, contenant 4 molécules inéquivalentes (numérotes), $\hat{a}$, $\hat{b}$ et $\hat{c}$ sont les axes cristallins. La simulation des niveaux magnétiques montre que **B** est parallèle à $\hat{c}$. **b** Les axes $\hat{x}_q$, $\hat{y}_q$ et $\hat{z}_q$ correspondent aux axes principaux des états quintets formés par une paire d'excitons triplets localisés sur les molécules voisines *1* et *2* ($T_{1,2}$). Nous avons observé un angle θ entre **B** et $\hat{z}_q$ d'environ 90° ainsi qu'un angle ϕ entre **B** et $\hat{x}_q$ cd $\sim 30°$ en accord avec les calculs théoriques.

Le gaz d'électrons bidimensionnel (2DEG) à la surface de l'hélium liquide est intéressant à la fois pour la recherche fondamentale et les sciences appliquées. Sa physique a déjà été très largement étudiée. Nous sommes toutefois les premiers à avoir réussi à réaliser un couplage ajustable entre deux degrés de liberté quantiques dans ce type de système. Nous avons en effet profité des caractéristiques extraordinaires de ce système pour réaliser un système fondamental QED, dans lequel un atome interagit avec une cavité électromagnétique. L'utilisation de la haute pureté du 2DEG est en effet une approche originale de la QED avec ses avantages et ses difficultés propres. Nous avons exploité la quantification du mou-

vement des électrons dans la direction perpendiculaire à la couche en présence d'un champ électrique $E_\perp$ donnant lieu à une série de type spectre de Rydberg liée à la présence d'une charge image induite dans l'hélium liquide. Par ailleurs un champ magnétique vertical B_z génère une force de Lorentz sur les électrons qui décrivent des orbites cyclotron et induit la quantification du mouvement dans le plan avec la formation d'un spectre discret de niveaux de Landau. Ces deux degrés de liberté décrivant respectivement le mouvement transverse et longitudinal des électrons sont indépendants mais peuvent être couplés par l'application d'un champ parallèle B_y (Fig. 4). Dans ce cas la force de Lorentz acquière une composante verticale et perturbe les composantes de Rydberg du système. Ce couplage entre les degrés de liberté transverses et longitudinaux peut être ajusté simplement grâce à l'amplitude de cette composante horizontale du champ magnétique.

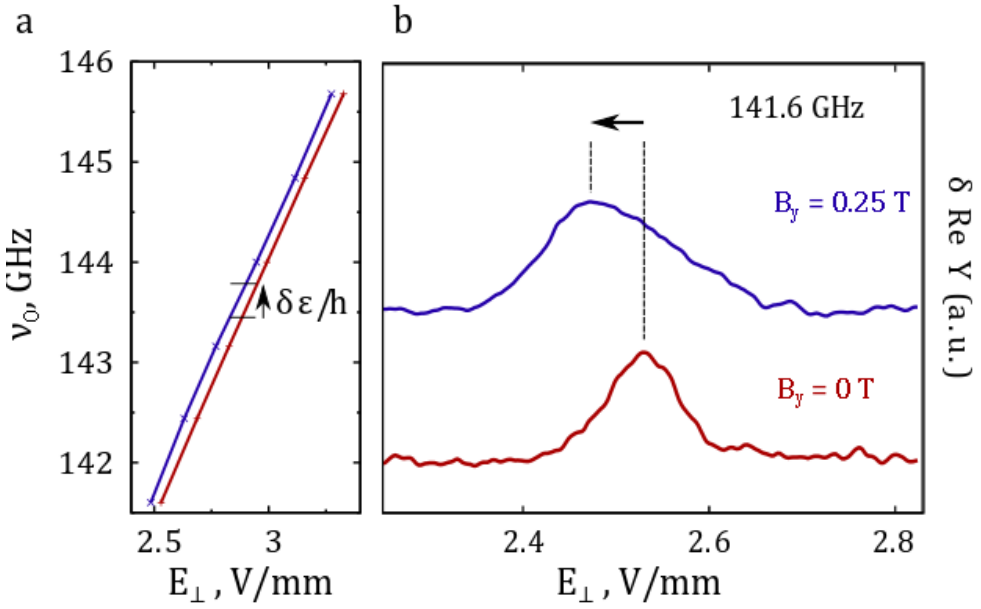

Figure 4: **a**, Mesure d'effet Stark linéaire de l'énergie de transition entre les deux premiers niveaux de la série de Rydberg en fonction du champ électrique perpendiculaire pour deux valeurs de champ magnétique $B_y = 0.25$ T (bleu) et $B_y = 0$ T (rouge), le décalage entre les deux courbes montres l'effet du champ magnétique sur l'énergie de la transition Rydberg. Nous introduisons $\delta\epsilon$ comme le décalage en énergie de la transition avec le champ magnétique, la valeur de $\delta\epsilon/h$ pour $B_y = 0.25$ T illustrée sur la figure. **b**, Exemples de spectres pour 141.6 GHz à $B_y = 0$ et 0.25 T, $B_z = 0.73$ T.

Nous avons dérivé pas à pas une description théorique de ce couplage entre états de Rydberg et niveaux de Landau. Nous avons écrit un Hamiltonien de type Jaynes-Cummings pour le gaz d'électrons 2D confiné en présence d'un champ magnétique avec une petite composante longitudinale en fonction de laquelle nous avons calculé l'évolution du spectre. (Fig. 5). Un bon accord entre les prédictions numériques de ce modèle et les expériences a été obtenu sans paramètre ajustable.(Fig. 6).

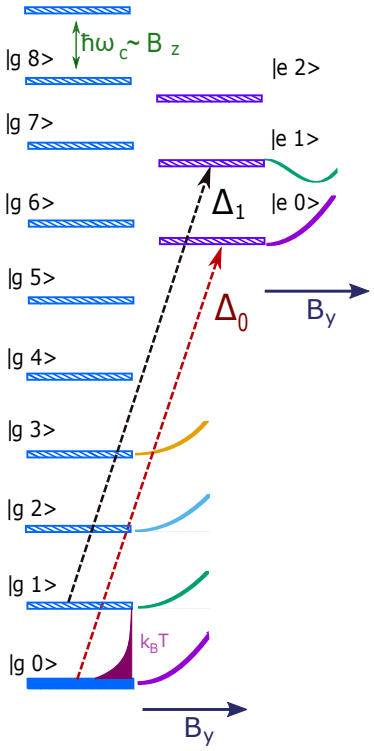

Figure 5: Diagramme des niveaux d'énergie du gaz d'électrons 2D. Les états sont désignés par $|n, m\rangle$, où le premier nombre quantique donne l'état atomique et m est le nombre de Landau (nombre de photons dans la cavité). La distance entre les niveaux de Landau est définie par B_z. Les pics de résonance Δ_0 et Δ_1 correspondent à la conservation des nombres quantiques m ($\Delta m = 0$) $|g, 0\rangle \rightarrow |e, 0\rangle$ et $|g, 1\rangle \rightarrow |e, 1\rangle$ transitions. L'évolution calculée des niveaux individuels (redimensionnés pour la visibilité) avec B_y jusqu'à 1 T est indiquée par des lignes colorées.

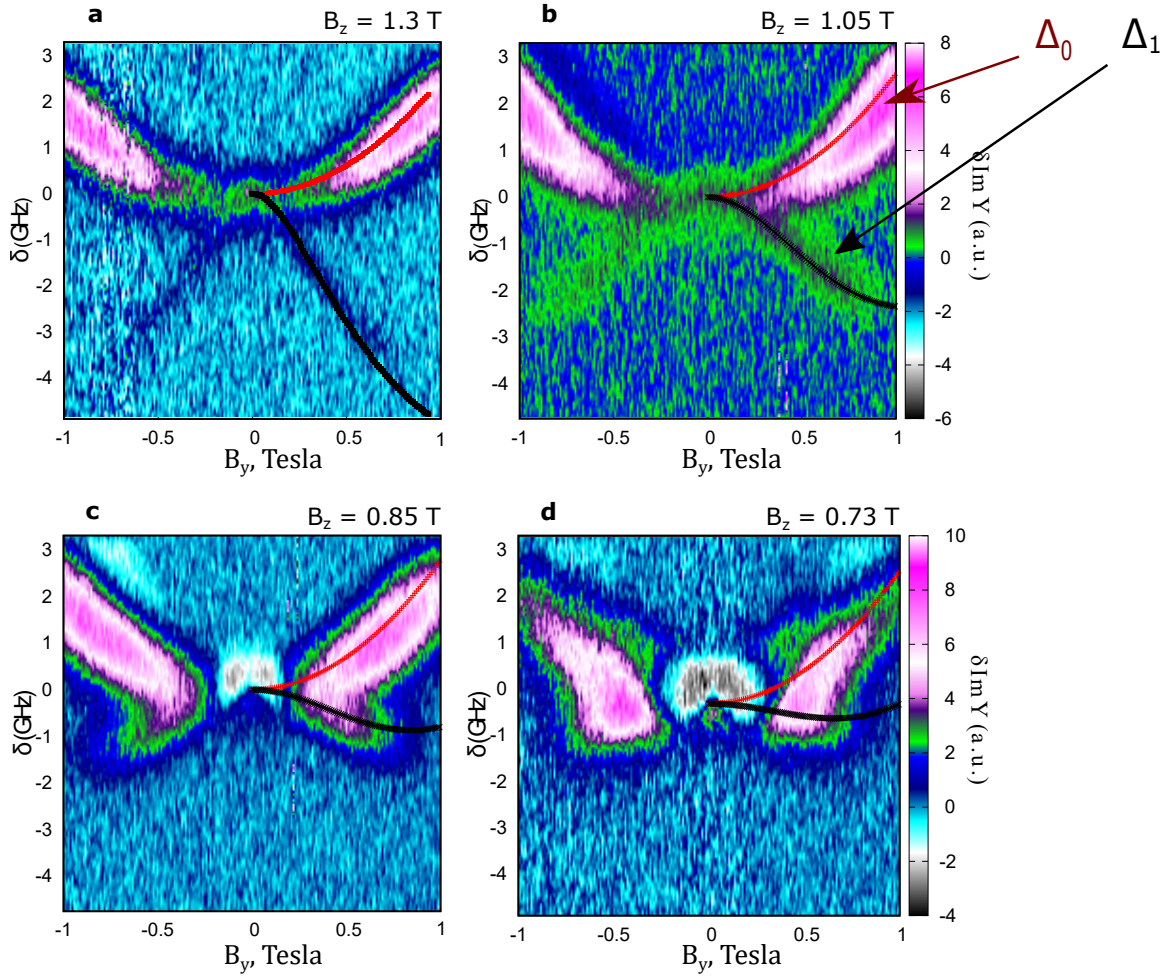

Figure 6: Résultats des calculs de l'hamiltonien d'électrodynamique quantique en cavité sur-imposé au cartes expérimentales montrant l'évolution des niveaux avec le champ magnétique parallèle B_y. Les courbes rouges et noires montrent les prédictions de l'Hamiltonien pour l'énergie des transitions Δ_0 et Δ_1 entre les etats $|g,0\rangle \rightarrow |e,0\rangle$ et $|g,1\rangle \rightarrow |e,1\rangle$ respectivement.

Nous avons donc obtenu un nouveau système pouvant être décrit par analogie avec un atome interagissant avec une cavité électromagnétique dans le régime quantique. Dans la mesure où il s'agit d'un système très propre dont les seules perturbations sont constituées par les modes de ripplons dont l'effet est négligeable dans nos conditions expérimentales, en contrôlant les populations des de Rydberg états quantiques on peut imaginer la réalisation d'un laser accordable dans le domaine micro-onde.

Acknowledgements

I would love to thank Alexei Chepelianskii, my supervisor who taught me basically everything about physics, for all his efforts and patience and for leading me through this years to the point when my Dissertation is written. I am extremely lucky to have worked with a real genius in both experimental and theoretical physics.

My thanks also to my supervisor famous Helene Bouchiat, brilliant physicist and the head of our MESO group in LPS, for comprehension, care, attention to details, kindness and support. Her curiosity, administrative skills, deep understanding of complex physics, great leader qualities, decisiveness and intelligence are truly inspiring.

During last years I had a great chance to learn from such bright minds as Sam Bayliss and Leah Weiss, passionate and hard working young scientists, whose contribution to the first part of this Dissertation is indispensable. I also want to thank Dmitriy Shepelyansky and Denis Konstantinov for their ideas which gave rise to the studies presented in the second part of this Dissertation. Many thanks to Vadim Derkach, my dear friend, who helped to set up the experiments, to John Anthony for providing samples and necessary information, to Paulina Plochocka and her group in LNCMI for collaborative experiments and nice stay in Toulouse, to Thierry Chaneliére for helping to develop optical part of the experiment, his support and courage, to Julien Gabelli for providing us with a strip-line for our measurements.

I would also love to express my gratitude to my family for encouraging my curiosity, supporting me at every step of my life, endless love they give me and for respecting my choice to make my PhD in France. Thanks to Murat Tagirov, the head of my former department of Quantum Electronics and Radiospectroscopy in Kazan, and EPR and NMR groups for their promotion.

In the hardest times I had great friends in the laboratory: Bastien Dassonneville, Marko Kuzmanovic, Mathieu Fechant, Jonas Miguet, Diana Watfa and Rebeca Diaz. Their help and friendship are very appreciated. Thanks to the whole MESO group for all the help whenever it was needed: Sandrine Autier Laurent, Sophie Gueron, Meydi Ferrier, Richard Deblock, Alik Kasumov, Taro Wakamura, Alexandre Bernard. Also many thanks to Fabrice Bert and Loic Rondin for their care.

Last but not least I want to thank my friends from Kazan, who stayed by my side despite of thousands of kilometers separating us: Ed Madirov, Dilyara Khamidulina, Katya Voronina, all the OPRST and near-OPRST, Grigoriy Sergeevich and many others. Also many thanks to my Parisian friends for their love and support: Valeria Volkova, Mickael Mehou-Loko, Kamil Akmaldinov, Alexandra Ermakovich, Vladimir Veksler, Maeva Dayras, Manohar Kumar, Valeriy Panin, Herve Vast, Pavel Kononov and others.

Contents

Chapter 1

Introduction

In this dissertation we present studies of two Coulomb bound systems of very different nature: triplet excitons which are neutral strongly bound states possesing a long lived spin which can addressed by magnetic field and electrons on helium bound to their image charge inside liquid helium owning large dipolar momentum and which are thus sensitive to electric field. In the sense these two systems are complementary and we will show that in both cases simple quantum mechanical models allow to gain a deep insight in the system structure. Therefore this Dissertation is divided in two parts. In the first part we investigate bi-exciton fine structure and geometrical aspects of their formation in organic semiconductors. In the second part we demonstrate a new way to realise a quantum electrodynamics system of an atom interacting with an oscillator. Thus we start with rather applied research and then continue with fundamental physics. Despite of very different physical systems explored, both subjects are linked by the experimental spectroscopic methods which are developed in this Dissertation.

1.1 Spintronics in organic semiconductors

New organic materials with designable properties can satisfy researchers needs, promissing a bright new world of eco-technologies. Meanwhile silicon semiconductors seem to have reached the honorable end of their career, organic semiconductors come into play. Indeed, their application offers new appealing features such as bio-compatibility, easy-fabrication, rich physics and controllable properties, so recently engineering and technologies tend to become more organic.

One of the most significant for the humanity applications of molecular semiconductors is definitely the green energy. Even though for many countries exhaustible resources based energy remains the defining sector of economics, it is time when people become overall more responsible about the planet and ecological situation getting worse faster and faster.

Organic semiconductors show unprecedented properties for solar energy and gather more and more attention in past decades due to implying lower cost, light weight, efficient, flexible and multiform alternative to inorganic solar cells. Particular type of molecular semiconductors - singlet fission materials - provide outstanding opportunities for such application due to their inherent capacity to yield twice as many change carriers per one absorbed light photon as conventional inorganic semiconductors. In this Dissertation we study exactly this kind of materials - TIPS-tetracene.

However, for any type of application of new materials one needs to understand their inner properties and fundamental physical phenomena defining them. Singlet fission materials exhibit great richness of such phenomena and combine processes and effects occurring in many various physical systems, like photoluminescence, spectral hole burning, excitons formation, diffusion and annihilation, dipolar and exchange coupling, photon up- and down-conversion *etc.*

We present here careful studies of such an intrinsic spin property of TIPS-tetracene as the bi-exciton formation following singlet fission. We focused on two aspects of spin composition in TIPS-tetracene. First, we will present intra-triplet coupling studies. For that we used optically detected magnetic resonance, to probe different spin species and follow their evolution in varying conditions. From those measurements we obtain dipolar coupling parameters for triplet and quintet excitations, examine samples' morphology and determine not only triplet excitons orientations in the samples, but also establish inner geometry of bi-exciton formation by two exchange-coupled triplet excitons - identify specific molecular sites on which quintet (bi-exciton) states reside via correlating experimentally extracted spin structure with the molecular crystal structure.

Then another aspect concerns the coupling actually forming a quintet state of two triplets - we present collaborative results on inter-triplet exchange coupling investigated by means of high field magneto-photoluminescence measurements. They allow us to assign certain exchange-coupling strength values to various triplet pairs and specify photoluminescence spectra corresponding to each pair.

1.2 2 dimensional electron gas

Meanwhile everything in the Universe tends towards equilibrium, the fundamental physics aspires to simplicity. Same old story - theoretical assumptions start with 1 dimension, 1 particle, 1 interaction, neglecting everything which is excessive. One object motion is easy to follow, a dance of a pair is then more twisted, but still understandable. But as in a love triangle, where the compound of emotions becomes intricate, many-body case rises a problem with a right approach not found yet. Therefore we take the route we already

know and map it to another goal - to understand the complicated we need first to descend to a simplicity, unwrapping messy threads of phenomena revealing their inner logic, then once the milestone of purity is reached, building a Babylon tower by increasing back the complexity brick by brick is the second phase of the way towards the comprehensive understanding.

Simplicity means the minimum of interactions, which implies the purity. High purity systems allow to probe experimentally various fundamental phenomena. Then elementary particles - electrons - confined on the surface of liquid helium-4 perform a perfect example of such a system. Electrons on the liquid helium surface have very high mobilities, thus giving an access to study Wigner crystallization, correlated charges transport, topological magnetoplasmons, many-body physics effects *etc.*

Therefore 2 dimensional electron gas (2DEG) on the liquid helium surface is interesting for both fundamental research and applied science (in particular, for quantum computing) at the same time.

For both interests one needs to be able to manipulate the system and to tune it finely. We profit from extraordinary characteristics of this system to build a famous fundamental quantum electrodynamics (QED) system, in which an atom interacts with an electromagnetic field.

Using high purity 2DEG is indeed an original approach to QED with its' proper advantages and difficulties we managed. We applied perpendicular electric field to confine the electrons, thus inducing Rydberg energy levels series, which then plays role of a hydrogen-like atom. Then perpendicular magnetic field quantized the electrons' in-plane motion, resulting in equidistant Landau levels - an oscillator for the QED system. Further to couple the atom to the oscillator we mixed perpendicular and in-plane motion degrees of freedom by applying parallel magnetic field. Energy levels are monitored using Stark spectroscopy measurements. In order to describe this coupling between Rydberg series and Landau levels we derived Jaynes-Cummings type Hamiltonian with no fitting parameters and it showed perfect agreement with the experimental results. Thus we realised experimentally coupling between quantum objects easily tunable by the parallel magnetic field strength.

Part I

Spectroscopical studies of bound excited states formation in organic semiconductors

Chapter 2

Physics of organic semiconductors

2.1 Interest

Recently material science focuses a lot of attention on organic semiconductors [1]. They underlie numerous revolutionary technologies for various applications. In terms of consumption application organic printable thin-film transistors (OTFT) first reposted in 1986 [2] are designed, for example, for flexible displays [3, 4], electronic paper [5, 6, 7, 4], memory storage [8, 9], pentacene thin-film transistors appear to be sensitive to humidity, whereas can be used as sensors [10], organic transistor based circuits are useful for chemical vapor sensing [11]. Furthermore OTFT are easier to fabricate than their silicon-based analogues. All that is possible due to a scalable printing process, which is way less complex than silicon-based analogues fabrication by deposition [4, 12].

In terms of engineering applications organic semiconductors are also promising for aqueous batteries with long cycle life [13] (for example, due to high chemical stability, quinone based rechargeable batteries showed 50 stable charge-discharge cycles [14]), circuits [12] and new hybrid materials design [15, 16]. Apart from that in 2017 easy-fabrication surface-enhanced Raman spectroscopy (SERS)-active nanostructured organic semiconductors were reported, revealing unprecedented Raman signal enhancements (up to $3.4 \cdot 10^3$ for the probe molecule methylene blue) [17]. Since nowadays the synergy of different fields of science expands our vision of progress, organic semiconductors' application for biocompatible devices compound another wide full-fledged domain of studies. Full-organic devices make transhumanistic future start today. Indeed, many incredible inventions have been already reported, such as dopamine sensing by a neuro-inspired device platform [18], electronic sensors based on the organic electrochemical transistor for *in vitro* monitoring of living cells [19], organic electrochemical transistors (OECTs) used to record the electrical activity of cells, changes in ion permeability of cell layer, detect analytes interacting with receptors or to perform artificial neural networks [20, 21].

Markedly triplet excitons in organic semiconducting materials are being studied since their reactions can determine efficiencies in light-emitting diodes and photovoltaics [22, 23, 24, 25, 26].

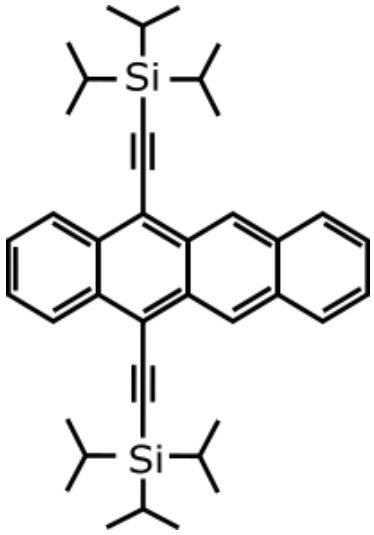

Figure 2.1: Schematic illustration of a TIPS-tetracene molecule.

2.1.1 Singlet fission

The singlet fission (SF) is a process somehow analogous to quantum cutting for inorganic chromophores where one high energy photon is converted into two low energy photons [27, 28, 29] and multiple exciton generation (MEG) in quantum dots for inorganic semiconductors [30], although energy losses through electronic to vibrational energy conversion are inevitable.

SF materials remain of a particular interest despite of being discovered a half of a century ago [31], due to peculiar physics and possible applications in various systems and devices.

In tetracene SF being a singlet excitons' decay channel was first proposed already in 1968 [32]. And the TIPS-tetracene remains of a particular interest for its high SF efficiency [33].

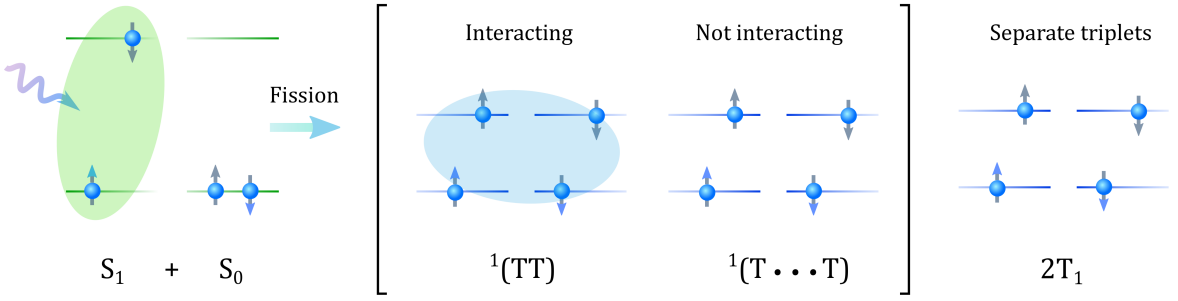

Figure 2.2: Schematic illustration of SF process. Photon absorption excites a singlet $S = 0$ state on a TIPS-tetracene molecule. Then this molecule shares half of it's energy with a neighbouring molecule resulting in two triplet excitons with $S = 1$.

Photon absorption induces singlet excitons $S = 0$ on TIPS-tetracene chromophores. This excitation may be shared with a neighbouring molecule's chromophore in its' ground state, thus forming two triplet $S = 1$ excitons on these chromophores (which takes ~ 100 fm) (Fig. 2.2) [34, 35]. Initially formed bound state $^1(TT)$ first spatially separates (~ 1 ps) into intermediate state $^1(T \cdots T)$ and then decaying into individual triplets, who can fuse into a singlet ($\gg 1$ ns) [36, 37].

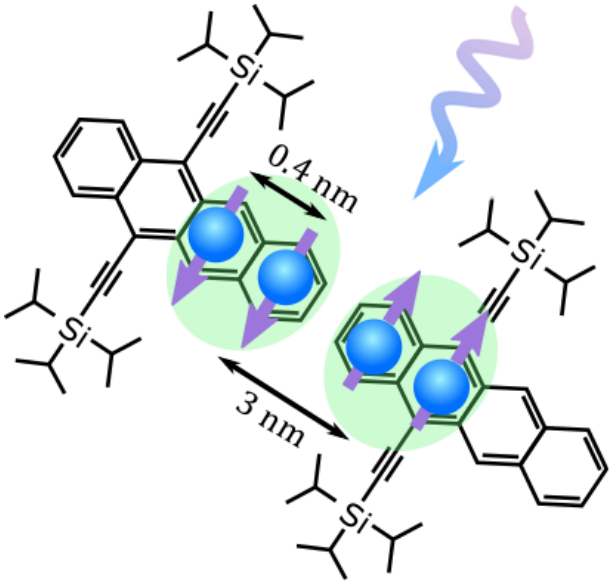

Figure 2.3: Schematic illustration of triplet pair formation on neighbouring chromophores adapted from [38]

SF is allowed due to being spin-conserving and thus has fast kinetics [39], competing singlet state relaxation through a photon emission. Thus SF converts almost 100% of photons absorbed into triplet excitations [40, 41, 42, 43].

2.1.2 Solar cells efficiency

One of the most appealing applications of SF materials is photovoltaics. In particular, SF can be used to increase solar cells efficiency [34, 35, 1]. Indeed, single-junction solar cells are restricted by thermodynamic limit (Shockley-Queiseer limit) of $\approx 33\%$ [44], while generation of multiple excitons can be a solution for this problem [45, 46, 47].

Spin-allowed processes of the SF and the subsequent separation of the triplets are intensively studied and inorganic semiconductors remain the most popular base for solar cells [48, 49, 50, 51, 52, 50, 53, 54, 55, 52]. They have certain bandgap and yield a charge carrier once a photon of large enough energy is absorbed (Fig. 2.4a). This implies low efficiency, since even if a photon is absorbed, then it generates one charge carrier, no matter what was the photon's energy:

$$E_{obt}^{sg} = \begin{cases} 0, & E < E_0, \\ \\ E_0, & E \geq E_0 \end{cases} \tag{2.1}$$

Combining single-gap materials with SF semiconductors in the same device in order to increase photon absorption by covering different spectral ranges is considered to be a solution. Implementation requires donor/acceptor interface to ionize triplet excitons, such devices have shown great results - up to 126% external quantum efficiencies (EQEs, charge carriers per second to photons per second ratio) and about 200% internal quantum efficiencies (IQEs, charge carriers per second to absorbed photons per second ratio) [56, 57].

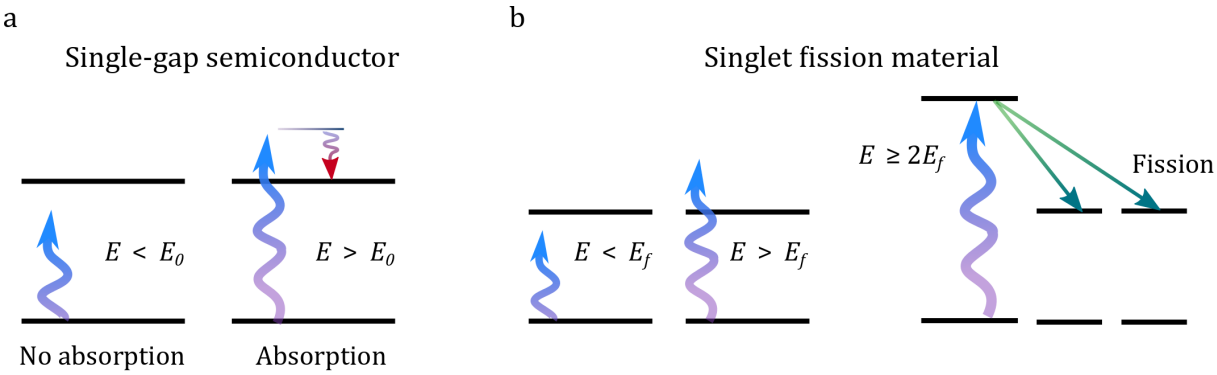

Figure 2.4: Solar cells' photons absorption sketch. **a**, in ordinary semiconductors a photon is absorbed only if its' energy exceeds the bandgap E_0. It leads to a waste of lower energy photons ($E < E_0$) and for those with larger energy ($E > E_0$) the excess is wasted via carriers thermalisation. **b**, combining SF material of $2E_f$ bandgap with a single-gap semiconductor of E_f bandgap to perform SF solar cell. Efficiency of such a system should be higher as here less photons are wasted: single-gap absorbs photons of energies $[E_f, 2E_f)$ and fission material absorbs all the photons that are $E \geq 2E_f$ yielding two charge carriers per photon.

Here one needs to choose two materials to fit an obvious criteria: for SF material's bandgap to be twice as large as the ordinary semiconductor's one. If we consider single-gap materials bandgap to be E_f, SF semiconductor will have $2E_f$ (Fig. 2.4b). Then lower energies photons will remain missed, whereas the single-gap part will absorb photons in energy range $[E_f, 2E_f)$ yielding a charge carrier and the SF part will convert higher energy photons into two charge carriers, decreasing the excessive photon energy loses through the thermalisation:

$$E_{obt}^{fm} = \begin{cases} 0, & E < E_f, \\ E_f, & E_f \leq E < 2E_f, \\ 2E_f, & 2E_f \leq E \end{cases} \tag{2.2}$$

2.1.3 Combining materials

Various realisations of such a combined solar cells have been reported. And even though perovskite solar cells form another branch of photovoltaics, tunability of perovskites' bandgap is a useful feature to implement to singlet fission devices. In 2017 Sangsu Lee *et al.* investigated triplet excitons transfer from organic semiconductor to perovskite film [58]. Using TIPS-pentacene/$MAPbI_3$ perovskite bilayer films they succeeded to get singlet fission formed triplets into conduction band of $MAPbI_3$ (Fig. 2.5). On the top of that their femtosecond transient absorption measurements revealed electron transfer in the bilayer film.

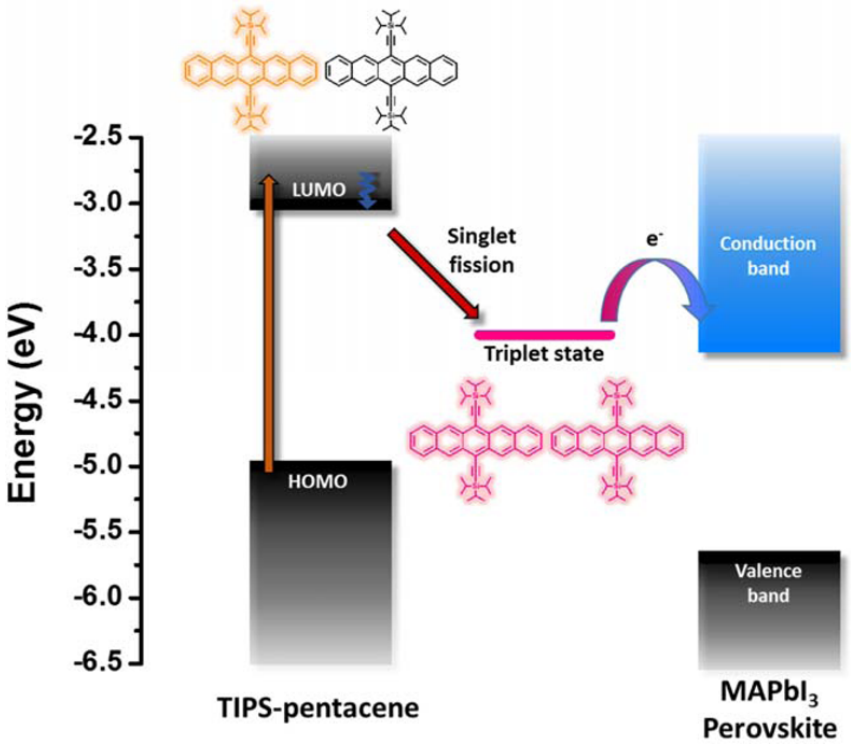

Figure 2.5: Schematic representation of TIPS-pentacene/$MAPbI_3$ perovskite electron transfer by S. Lee *et al.*. Illustration is taken from Ref. [58].

Another approach is to combine singlet fission organic semiconductors with quantum dots [59, 60]. In that case organic molecules are attached to a quantum dot as ligands, they absorb photons and then directly transfer singlet fission formed triplets inside the dot. N.J.L.K. Davis *et al.* reported that this technique had increased PbS quantum dots photoluminescence quantum efficiency twice with using TIPS-tetracene in comparison with the case when photons are absorbed in the quantum dot itself, revealing very high efficiencies for both singlet fission and triplet transfer processes [59].

Recently the same collaborative group of scientists have presented an improved version of singlet fission-to-quantum dot triplet transfer [60]. They performed a mixture of highly soluble singlet fission photon multiplication system. TIPS-tetracene was used to absorb photons and to form triplets by singlet fission, these triplets were then transfered to modified TIPS-tetracene ligand molecules, which could bound to PbS quantum dots and thus transfer triplets to them (Fig. 2.6), thus downconverting original optical photon energy to IR range.

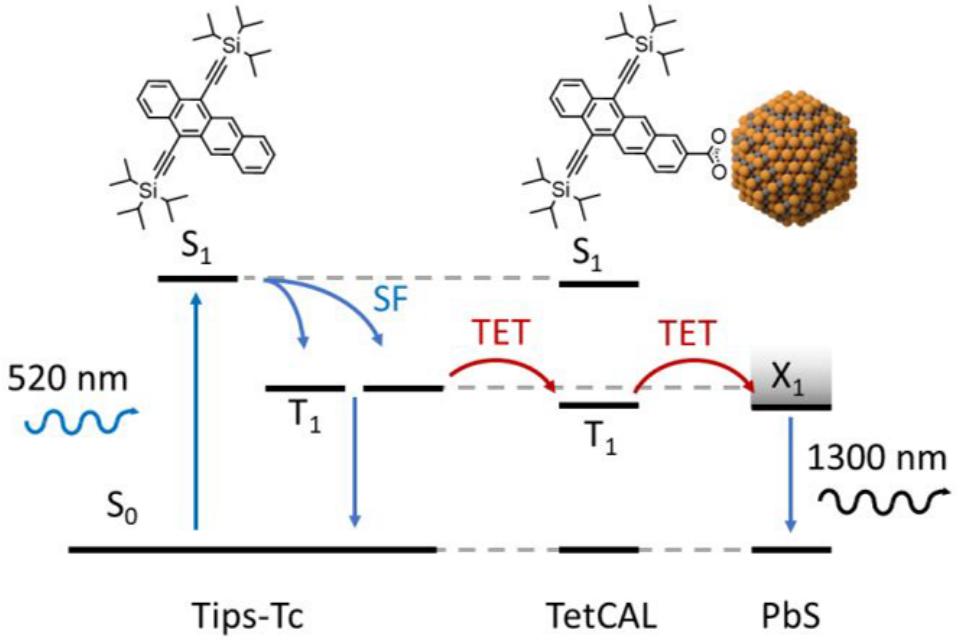

Figure 2.6: Triplet energy transfer (TET) scheme for TIPS-tetracene + Tetracene ligand (TetCAL) + PbS quantum dot system. TIPS-tetracene generates triplets by photon absorption following singlet fission, then the energy is shared with TetCAL bound to PbS quantum dot. Illustration is taken from Ref. [60].

Although the most promissing realizations of the combined material solar cells by now seems to be tetracene/silicon duo. Markus Einzinger *et al.* have recently reported their studies on silicon solar cells sensitization by tetracene [61]. They have designed a three layer device (Fig. 2.7) consisting of 30 nm of tetracene film, interlayer and silicon and empirically found the optimal width of the HfO_xN_y interlayer = $8\mathring{A}$. By electric-field-effect passivation they obtained yield of the fission in tetracene and the energy transfer to silicon of around 133%.

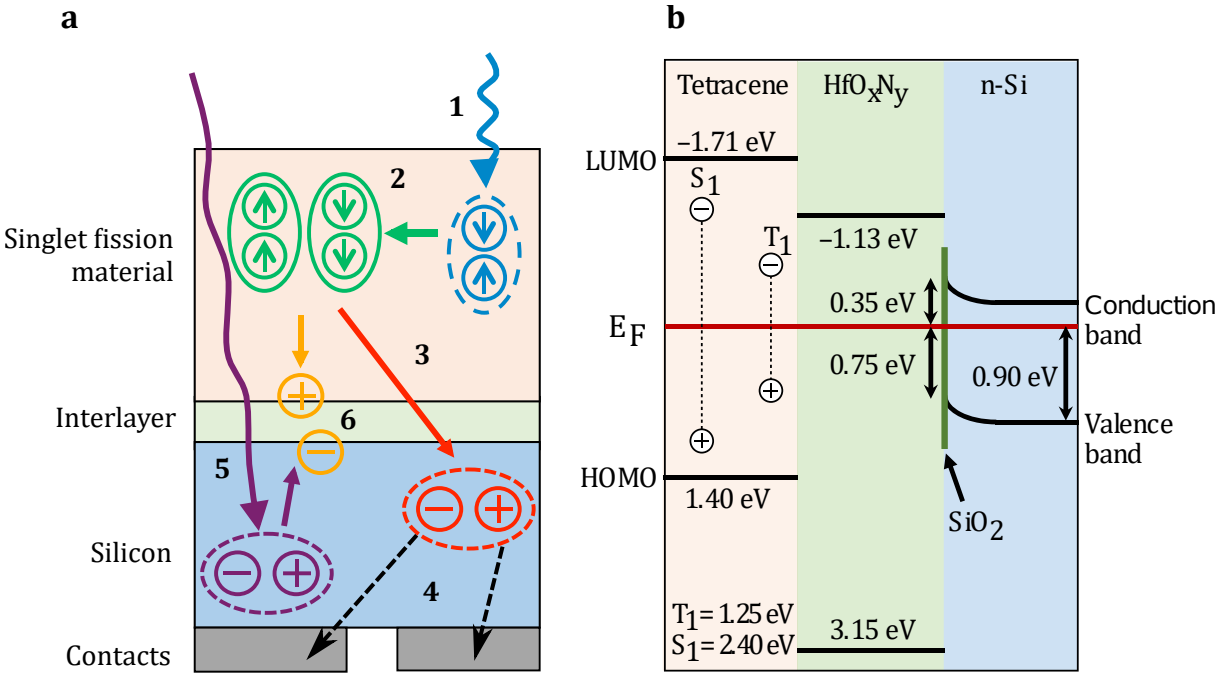

Figure 2.7: Markus Einzinger *et al.*'s singlet fission sensitized solar cell scheme. **a**, (1) Light absorption in tetracene, (2) singlet fission, (3) energy transfer to silicon, (4) charge separation, (5) light absorption in silicon, (6) electric field passivation. **b**, Energy transferring scheme. Illustration is adapted from Ref. [61].

2.1.4 Triplet annihilation

Another interest of SF materials like TIPS-tetracene is the light up-conversion due to triplet-triplet conversion into higher energy singlet exciton, particularly for catalysis [62], photovoltaics [63] and bio-imaging [64]. But in the Thesis we focus on bi-exciton states themselves rather than on triplet fusion.

2.1.5 Quintet excitons

Bi-exciton states are key excited-state species in a range of nano-structured materials from quantum confined inorganic systems [65, 66, 67] to synthetic molecular structures [68, 69, 70]. In organic semiconductors the exciton-pair mediates both the process of SF and triplet-triplet annihilation [71]. Optical characterization of bi-excitons remains challenging as their optical signatures are not easy to predict theoretically and usually overlap with singly-excited states. However magnetic resonance measurements revealed that the SF resulting triplet-pairs form a stable, bound spin-2 state (the quintet state) in few molecular systems [72, 73, 74]. The observation of the quintet state manifests strong exchange interaction of the triplets in a pair. This exchange coupling separates the pure singlet ($S = 0$) from the triplet ($S = 1$), and quintet ($S = 2$) pairings by J and $3J$ respectively, which critically impacts the available spin-dependent loss pathways (i.e.,

triplet-triplet annihilation from the pure quintet state is spin-forbidden [75, 76]). Further, its spin signatures provide an unambiguous marker of the bound triplet-pair state.

Antecedent optically detected magnetic resonance studies exhibit no spin-2 species trace [38], although recent electron paramagnetic resonance measurements [74] explained it to be related to samples' degree of order, which we discuss later (Chapter 5).

2.2 Magnetic resonance

Magnetic resonance (MR) techniques are a branch of powerful spectroscopic methods to study materials via electronic or nuclear spins allowing for determination of molecular structure and morphology.

2.2.1 Electron paramagnetic resonance

Electron paramagnetic resonance (EPR) also known as electron spin resonance (ESR) - is a powerful technique to study unpaired electrons' spins in various materials. It was first observed by E.K. Zavoysky in 1944 [77].

Zeemann effect

Unpaired spins under applied external magnetic field experience Zeemann effect - spin sublevels linear splitting proportional to g-factor, Bohr's magneton μ_B and magnetic field B:

$$h\nu = g\mu_B B_0 \tag{2.3}$$

g-factor characterises the specie's local environment through its' spin and orbital angular momentum. Further we consider g-factor of our species to be isotropic and equal to free electron's $g_{fe} = 2.0023...$ due to weak spin-orbit coupling in organic materials.

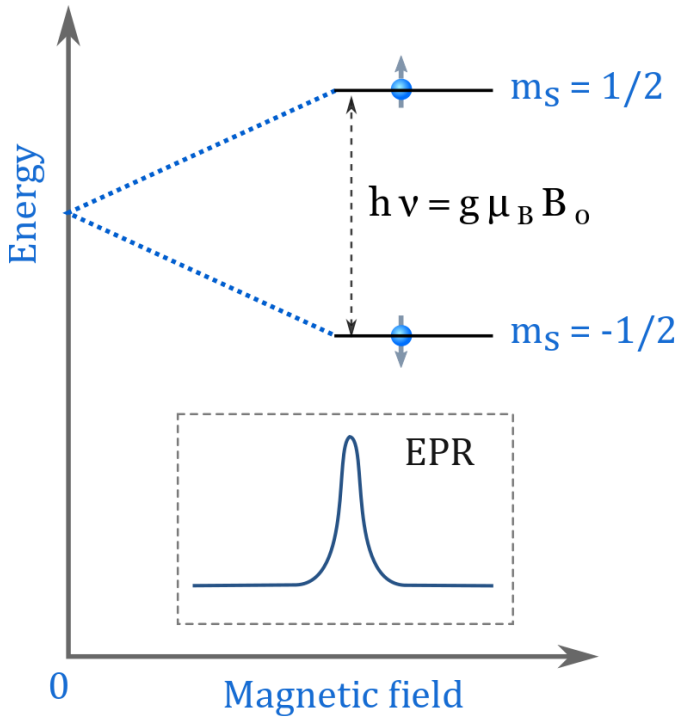

Figure 2.8: Schematic illustration of Zeemann effect on spin $S = 1/2$. Degenerate at $B_0 = 0$ spin sublevels $m_s = \pm 1/2$ split with external magnetic field. The magnetic resonance then appears at energy $h\nu = g\mu_B B_0$ yielding one peak at B_0 magnetic field.

Allowed by spin selection rule $\Delta m_s = \pm 1$ resonant transitions between spin sublevels for EPR at can be induced by applying MW at frequency $\nu = \frac{g\mu_B B_0}{h}$.

Zero-field splitting

Since triplet excitons of spin-1 are formed by pairs of spin-1/2, there rises a dipolar interaction between "electron" and "hole", not occurring for a single electron spin-1/2. This anisotropic interaction splits triplet state levels degenerated at zero magnetic field. Since dipolar interaction has vector origin, it is sensitive to orientation of the molecules compounding spin-specie. This useful feature plays the main role in our measurements presented in the following Chapter.
Unlike Zeemann effect, which is due to the spins' interaction with an external magnetic field, dipolar interaction is observable in zero-field - the spin sublevels shift is due to inter-spin-species coupling. The zero-field Hamiltonian in a molecular basis takes the form:

$$\hat{H}_{ZFS}/h = \mathbf{S}^T \cdot \mathbf{D} \cdot \mathbf{S} = D_x \hat{S}_x^2 + D_y \hat{S}_y^2 + D_z \hat{S}_z^2 \tag{2.4}$$

where $\mathbf{D}$ is the dipolar tensor (D-tensor) and $\mathbf{S}$ is the relevant vector of spin operators ($S = 1, 2$ for triplet, quintet states) defined along the principal axes ($\hat{x}$, $\hat{y}$, $\hat{z}$) of the

D-tensor. These directions are defined by the spatial symmetry of the spin distribution on the molecule and strongly depends on its' geometry. The $\hat{z}$-axis is defined by the axis of maximum dipolar coupling, where the strength of the dipolar coupling parameters $D = \frac{3}{2}D_z$ and $E = \frac{1}{2}(D_y - D_x)$ reflect the degree of confinement and asymmetry of the spin-system.

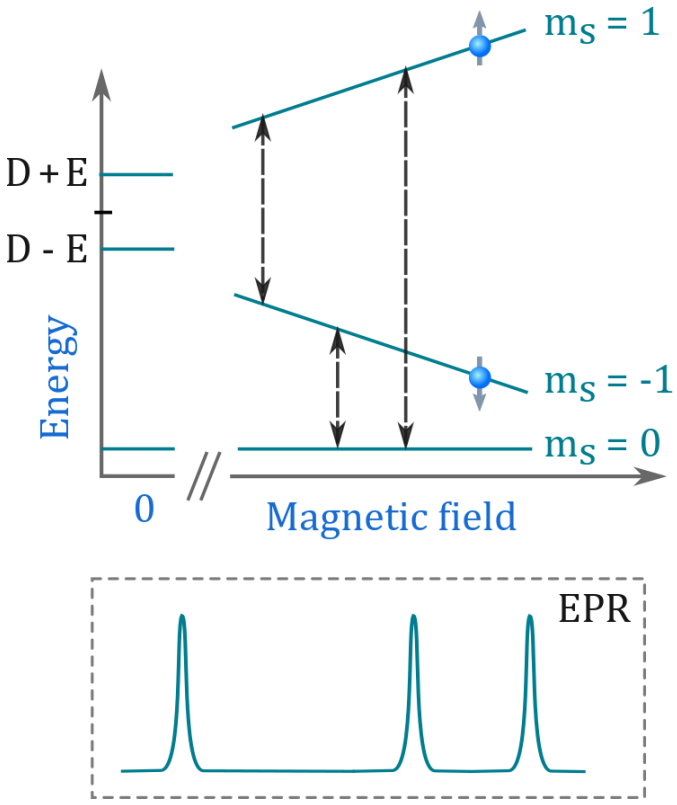

Figure 2.9: Schematic illustration of triplet $S = 1$ energy levels splitting due to Zeemann effect and the dipolar interaction, which lifts the spin sublevels degeneracy. Sublevels $m_S = \pm 1, 0$ appear shifted already in the zero magnetic field, thus three magnetic resonance transitions, whose positions in the absence of magnetic field are given by this initial splitting and in non-zero field - by contribution of both Zeemann and dipolar terms.

We use this dipolar interaction to probe geometrical location of the excited states on molecular sites.

Hyperfine interaction

Spin-1/2 in EPR can also experience hyperfine interaction - interaction of the electron spin S with nuclear spins I of surrounding atoms. It results in an additional spin sublevels splitting occuring in the external magnetic field. Figure 2.10 represents a schematic example of a case of electronic spin $S = 1/2$ interacting with nuclear spin $I = 3/2$ in increasing external magnetic field, leading to 4 nuclear spin sublevels for each of the 2 electronic spin sublevel - i.e. 8 levels with 4 resonant transitions in EPR spectrum.

These transitions are separated in the field by value A which represents this hyperfine interaction.

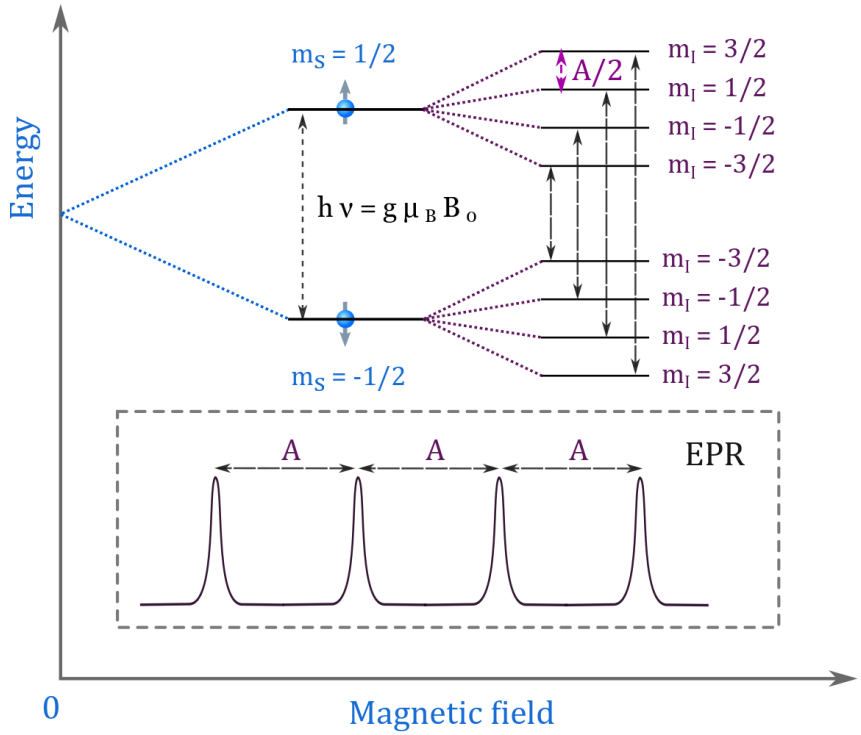

Figure 2.10: Schematic illustration of electronic spin $S = 1/2$ energy levels splitting due to Zeemann effect and the hyperfine interaction with a nuclear spin $I = 3/2$. Each electron sublevels $m_S = \pm 1/2$ split into 4 nuclear spin sublevels $m_I = 3/2, 1/2, -1/2, -3/2$ (separated by $A/2$ value) resulting in four magnetic resonance transitions defined by selections rules $\Delta m_S = 1$ and $\Delta m_I = 0$. These resonances are shown on the inset, they are centered around electron resonance position, the distance between the neighbouring resonances equals to hyperfine interaction constant A.

Continuous wave EPR

Continuous wave EPR (CW EPR) is measured by applying an external constant magnetic field and MW irradiation on a sample and detecting resonant transitions between energy levels splitted and shifted by Zeemann effect, zero-field splitting (also called fine EPR fine structure) and hyperfine interaction. MW frequency and magnetic field ranges depend on the spin species' g-factor which defines their ratio.

Pulsed EPR

Constant external magnetic field $\mathbf{B}_0$ induces a torque affecting an electron's magnetic moment μ:

$$\hat{t} = \mu \times \mathbf{B}_0 = \gamma \mathbf{J} \times \mathbf{B}_0, \tag{2.5}$$

where $\mathbf{J}$ is the angular momentum and $\gamma = \mu/J$ is the gyromagnetic ratio.

This causes a precession of μ along $\mathbf{B}_0$ with Larmor frequency $\omega_L = -\gamma B_0$.

Then adding another alternating external magnetic field $\mathbf{B}_1$ perpendicular to $\mathbf{B}_0$ and $\mathbf{B}_1 \ll \mathbf{B}_0$ μ precesses around both of them with the same ω_L frequencies simultaneously.

Considering an ensemble of electrons we deal with the total magnetisation $\mathbf{M}$ which is a sum of separate electrons' magnetic momenta. While precessing around $\mathbf{B}_1$ at some point $\mathbf{M}$ becomes perpendicular to $\mathbf{B}_0$. Turning the $\mathbf{B}_1$ off at this moment of time ($\pi/2$ pulse) leaving $\mathbf{M}$ precessing around $\mathbf{B}_0$ exerting so-called free inductance decay (FID, Fig. 2.11a) whose Fourier-transformation in time gives a frequency spectrum if the entire EPR spectrum is excited.

Some time after M becomes equal 0 due to magnetic momenta disorientation - they are getting evenly distributed in a plane perpendicular to the constant field.

Applying another pulse of duration π (which means to turn the $\mathbf{B}_1$ field on for time long enough for the momenta to turn to π radian around $\mathbf{B}_1$) induces a process inverse to FID. Then after some time τ after this second pulse the magnetisation M starts increasing raising a spin echo signal (Fig. 2.11b). Various pulse sequences are used for different EPR measurements, however we will not focus on them in the Thesis, this Subsection is solely informative.

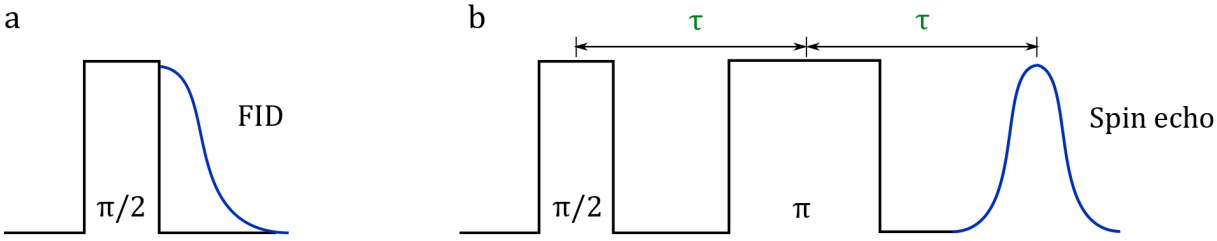

Figure 2.11: Pulsed EPR. **a**, half-π MW ($\mathbf{B}_1$) pulse followed by FID. **b**, spin echo forming pulse sequence $\pi/2 - \tau - \pi - \tau -$echo.

2.2.2 Optically detected magnetic resonance

In various systems MR can be detected optically by optically detected magnetic resonance (ODMR). Nowadays it is well known through experiments on control and detection of a single nitrogen-vacancy (NV) centres' electronic state [78, 79, 80, 81, 82] - unprecedented sensitivity. So ODMR is an important tool for quantum computers development [83], information storage [84] and extreme spatial resolution detectors [85, 86, 87].

This method has certain advantages for studying spins in organic semiconductors. First of all, it gives access to excited states of molecules and charge carriers instead of dealing only with crystal structure defects. Secondly, ODMR as an optical method

has very high sensitivity - up to measurements of triplet states on a single molecule [88, 89]. Indeed, converting MW quanta to optical photons yields lower thermal noise, thus sensitivity is defined by laser stability and detector itself. Thirdly, spin selectivity through induced optical transitions. It means that one measures signal only from those spin species that were excited or their products. And besides, ODMR doesn't require special cavities contrary to EPR which is usually measured as changes of a Q-factor of a cavity, that makes it technically simpler and much more convenient for organic samples of different shapes and configurations.

NV-centres in diamonds have total spin $S = 1$, thus performing triplet system (Fig. 2.12). As it was discussed above, in the absence of external magnetic field $m_s = \pm 1$ spin sublevels are degenerated unless there is a zero-field splitting parameter $E \neq 0$. Increasing magnetic field lifts the degeneracy and then energy levels should evolve differently with field in different orientations due to dipolar tensor $\mathbf{D}$ being sensitive to the centre's geometry.

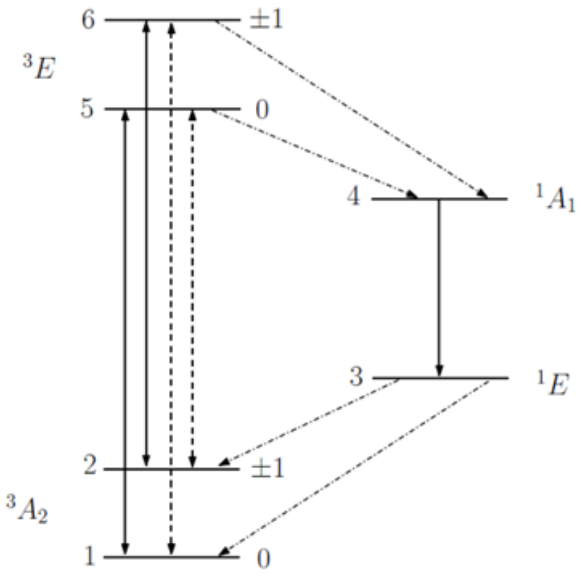

Figure 2.12: Energy levels diagram of the NV-centre in diamond [90]

Keunhong Jeong *et al.* performed studies of NV-centre's magnetic resonance transitions dependence on the field orientation [91]. They measured 2D ODMR for NV^- centres in bulk diamonds (crystals) and nanocrystals (powder). An example of their results for bulk sample are shown on figure 2.13. The maps confirm predicted difference in transitions behaviour at different orientations when the field is applied, though at zero field they are indistinguishable and all detected at 2.8 GHz. Thus ODMR is useful to determine samples morphologies and inner symmetry of defects in various materials.

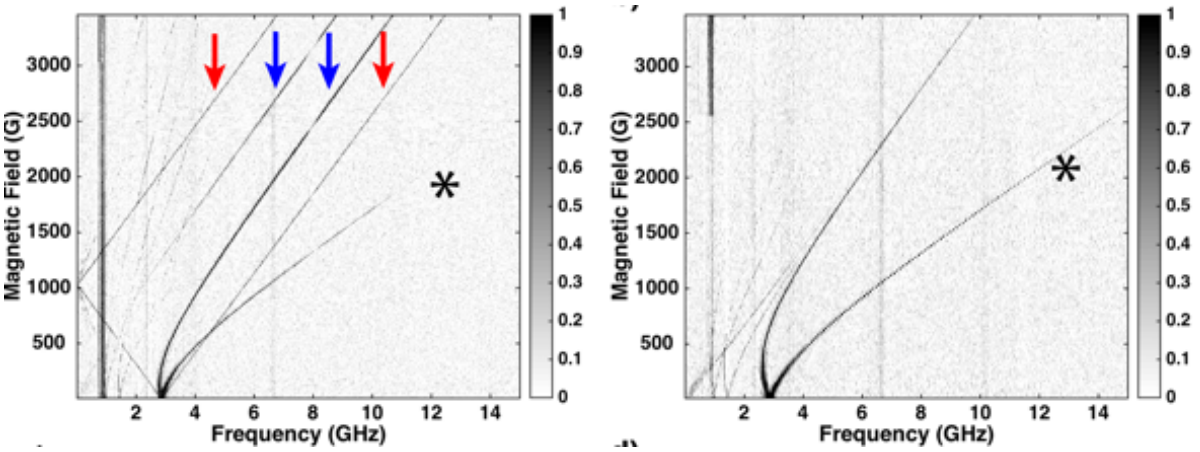

Figure 2.13: 2D ODMR maps of NV^- centres in diamond crystals with magnetic field oriented along the [1 1 1] (left) and [1 0 0] (right) crystallographic axes. Red and blue arrows indicate transitions corresponding to different orientations: red for 0° and blue for 109.5°. Figures from Ref. [91].

An important phenomenon for ODMR is photoluminescence, which is a photo-emission following photon absorption. As it was mentioned before (Subsection 2.1.1) in organic semiconductors a photon absorption on a chromophore creates an excited state with spin $S = 0$, which then may transform into two $S = 1$ triplet states via SF in our case or an intersystem crossing. A chromophore cannot relax to the ground state from these triplet states by emitting a photon due to spin conservation rule. However, zero-field splitting, Zeemann effect and hyperfine interaction discussed above (Subsection 2.2.1) remain relevant for these states. After triplets undergo inverse process of fusion (or intersystem crossing for materials with higher spin-orbit coupling) into a singlet state, the relaxation via photon emission becomes possible.

Thus since triplet and quintet states have non-zero spins, rather slow sweeping applied MW frequency and magnetic field as in EPR measurements allows to detect overall changes in photoluminescence of singlet states in certain magnetic field and MW frequency values determined by triplet and quintet states magnetic resonance transitions.

Chapter 3

Optically detected magnetic resonance measurements

3.0.1 Sample preparation

In the thesis samples of two types were investigated:

- crystals
- thin films

Crystalline samples were provided by Prof. John Anthony group. ODMR measurements were performed on polycrystals or single crystals of relatively right shape: they were chosen to have at least two opposite facets to be smooth and parallel to each other and to have a height comparable with a MW conducting stripline $\sim 1 - 2mm$. Thin film (TF) samples were drop casted from powdered TIPS-tetracene solution in chloroform on a thin glass substrate. Thus after the preparation TF samples had down side smooth attached to the substrate and the top surface of various relief. Sample preparations and installations were done by the author.

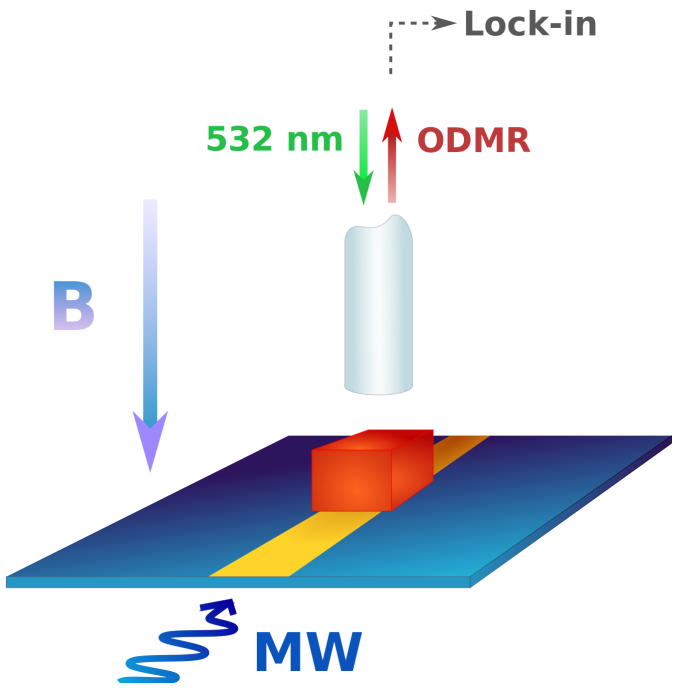

Figure 3.1: Schematic of the experimental set-up. Crystalline samples of TIPS-tetracene were optically illuminated (532nm, cw-excitation) under amplitude-modulated microwave excitation ($\mathbf{B_1}$) using a broadband copper stripline (0-2 GHz) in liquid helium (4 K). Photoluminescence was collected (via optical fiber and APD) to detect the microwave-induced change in photoluminescence (ODMR) as a function of both microwave frequency and static magnetic field ($\mathbf{B}$) with $\mathbf{B} \perp \mathbf{B}_1$.

Measurements were performed at frequency f swept in a range of $0 - 2$ GHz. MW was amplitude modulated at $f_{AM} = 137$ Hz in order to get an effect of MW power on/off to filter out the signal under no MW applied. MW was applied to the broadband copper stripline of a width $w_{sl} \sim 1.5$ mm and length $l_{sl} \sim 10$ mm via coaxial cables.

3.0.2 Signal separation

Previously spectroscopic distinction of species with different kinetics has been studied [92, 38, 93, 94, 95, 96].

A pair of triplet excitons formed on the same molecule is called "geminate triplets", since they were generated by SF, thus by the same photon. Such pairs have faster kinetics and contribute to in-phase signal (Fig. 3.2a). Whereas bimolecular (non-geminate) triplets recombination implies that recombining triplets come from different pairs which were separated. Thus the charges need to diffuse in the sample to "find" each other. It makes the specie's kinetics very slow [97, 98, 99] and thus occur out of phase (Fig. 3.2b).

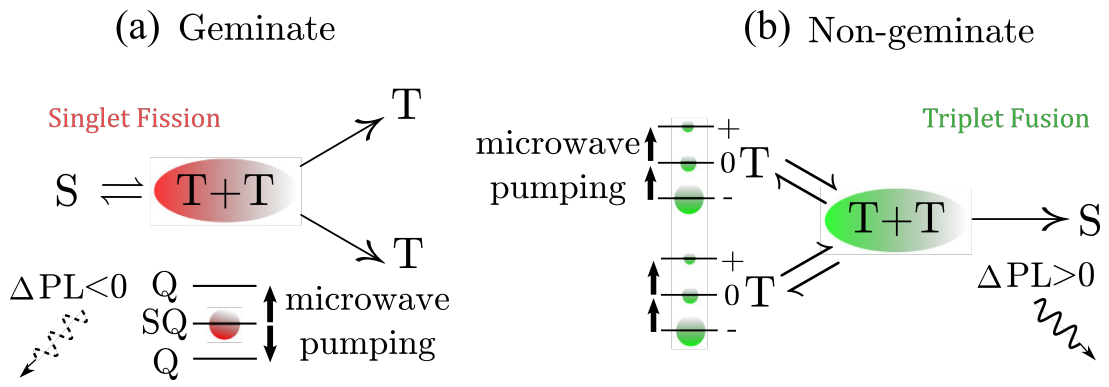

Figure 3.2: Geminate and non-geminate triplet pairs annihilation. **a** Geminate pair. Triplet pair is initially in one of the singlet character states. Applied MW is pumping population of the dark (non-emissive) quintet state. **b** Non-geminate pair. MW is increasing emissive triplet pairs population. Illustrations adapted from [38].

Whereby triplet and quintet spectra can be separated by lock-in phase relative to microwave modulation: the triplet species present in both the in-phase and out-of-phase channels, whereas quintet signatures are restricted to the in-phase measurements. We use this feature to isolate the quintet transitions by subtracting out-of-phase signal (Y-channel) from in-phase signal (X-channel) (following the work of Sam Bayliss, see ref [38]).

Thus AM frequency $f_{AM} = 137$ Hz was chosen to be slow enough to resolve non-geminate triplet states fusion signal. We used previously reported lifetimes of triplets and quintets in thin films which were found to be $\tau_t = 690$ μs and $\tau_q = 25$ μs [38]. However, it only gave us estimative values, since the species lifetimes depend on various circumstances, like amount of light, triplet density, morphology *etc.* So the optimal amplitude modulation frequency needs to be find empirically for certain measurements. For that we fixed MW frequency f_{MW} at resonant value and altered the f_{AM} to obtain better signal.

Initial singlet excitons inside of our samples were induced under cw 532 nm laser illumination, which was applied to the top-side of a sample via optical fiber. Optical scheme of the experiment is shown on figure 3.3, it was designed by Thierry Chaneliére and the author. The laser was split in two with a ratio 90:10 and then the brighter one was sent to the sample. The weaker beam was sent though a photodetector to proportional–integral–derivative controller (PID) supervising laser supply current to avoid laser power instability. Whenever the second beam power detuned from the fixed value, the supply current was altered in the opposite direction. Initially we have tried to use a balanced detector in order to reduce laser noise, however PID is more flexible.

ODMR signal (originating from the emission of singlet states created by the fusion of triplet pairs) was gathered by the same optical fiber and sent to an avalanche photodetector preliminarily being focused and filtered to avoid collecting the laser light. The

signal converted to the voltage was then recorded using lock-in detection at f_{AM}. For the detailed experimental scheme see Appendix III.

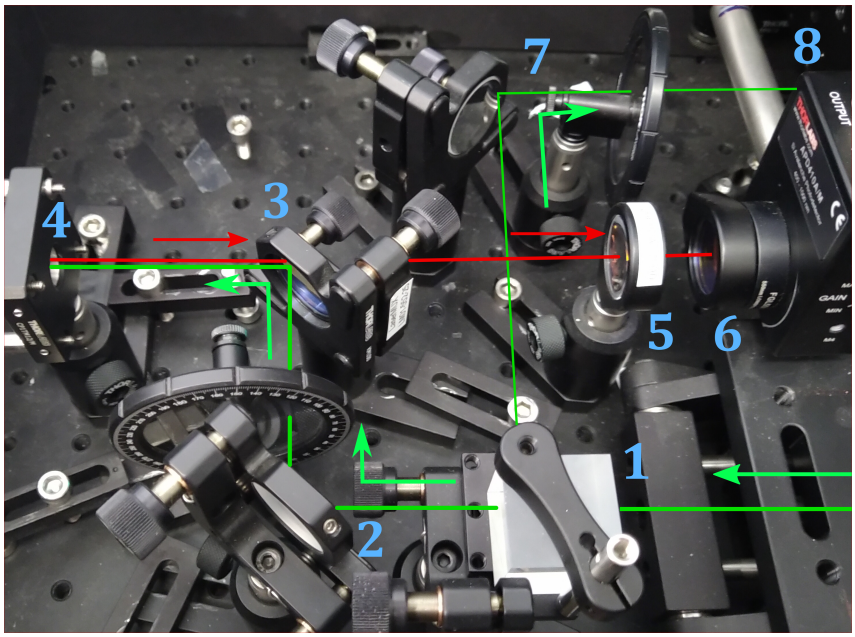

Figure 3.3: Photo of an optical table with a schematic representation of beams. 532 nm laser beam (green) is splitted at splitting cubical prism *1* at ratio 90:10, then more intense part of the beam is sent to optical fiber through *4* passing mirrors *2* and *3*. The weaker part of the laser beam after the cube *1* goes to a supporting photodetector *8* to control the laser power. ODMR signal (red) is obtained via the same fiber through *4*, then sent to an avalanche photodetector *6* through semi-transparent mirror *3* and focusing lens *5*. The photodetector *6* is equipped with a long-pass filter to avoid colleting the laser light.

Crystalline or thin film (TF) samples fixed by glasses were placed on the top of the stripline, situated on a sampleholder shown on figure 3.4.

Figure 3.4: **right** The crystalline (top) and the thin film (bottom) samples placed on the stripline on the top of the sampleholder. **left** The sampleholder installed on the movable part of the setup with coaxial cables connected to the stripline. After this part was placed inside of a protecting tube and then cooled in liquid Helium.

This sampleholder was nested inside of solenoids (here exact information on our two magnets - small one and 5 T - is needed) at a perpendicular to the stripline plane magnetic field.

The whole system was cooled in the liquid He4 and the temperature was varied in a range $1.5 - 4$ K, but most of the measurements were performed at $T = 4K$.

Most of the experiments were done by the author under the supervision of Alexei Chepelianskii (unless otherwise stated), some measurements were performed in collaborations, which will be marked in the Chapters 5,6.

Chapter 4

Bound excitons Hamiltonian

Before introducing the experimental results, let's analyse the quintet formation theoretically and derive the Hamiltonian we will use later to evaluate ODMR spectra. Quintet state is formed by two strongly coupled triplet excitations on adjacent molecules, so it is useful to switch to coupled basis. Thus, in this Chapter we present a theoretical relationship between triplet pair geometry and the resulting $S = 2$ triplet-pair fine structure (D_Q, E_Q and the principal axes $\hat{x}_q$, $\hat{y}_q$, $\hat{z}_q$). Previous measurements of the quintet states in various materials have found that $D_Q \sim D_T/3$, yet this relation holds only in the case of co-linear triplet D-tensors and in the absence of dipolar coupling between the excitons, and so acts as an approximate guide to identifying quintet spectra [72, 73].

4.1 Uncoupled basis

As described in the literature, for triplet excitons in organic semiconductors D_T and E_T are set by the spatially averaged spin-spin interaction of electron and hole, reflecting triplet states localized on a single molecule in TIPS-tetracene [100]. The $\hat{z}$-axis of maximal spin-spin coupling is out of the plane of the molecule and the $\hat{x}$- and $\hat{y}$-axes are in the plane of the molecule along the long and short axes as shown in Figure 4.1a.

The $S = 2$ triplet-pair fine-structure depends on the underlying orientation of a two such triplets. We assume that each triplet has the same zero-field parameters (D_T, E_T) and differ only in orientation and position. We define the principal axes of the triplet state on molecule A as $\{\hat{x}_a, \hat{y}_a, \hat{z}_a\}$ and on molecule B as $\{\hat{x}_b, \hat{y}_b, \hat{z}_b\}$ with the unit vector between molecule A and B given by $\hat{u}_{ab} = \vec{r}_{ab}/|\vec{r}_{ab}|$. The zero-field Hamiltonian of the pair in the uncoupled basis is then given by

$$\hat{H}^{(1\otimes1)}_{zfs}/h = \sum_{i=a,b} \mathbf{S}_i^T \cdot \mathbf{D}_t^i \cdot \mathbf{S}_i - 3\Gamma_d(\hat{u}_{ab}\cdot\mathbf{S}_a)(\hat{u}_{ab}\cdot\mathbf{S}_b) + J\mathbf{S}_a\cdot\mathbf{S}_b \quad , \tag{4.1}$$

where $\Gamma_d = \frac{\mu_0\mu_B^2 g^2}{4\pi|\vec{r}_{ab}|^3}$ gives the strength of the dipolar interaction and $|\vec{r}_{ab}|$ is the inter-triplet distance. In the limit of strong exchange coupling ($J \gg D_T$) the Hamiltonian is approximately diagonal in the coupled spin-basis defined by the states of pure total spin. Projecting the above Hamiltonian into the $S = 2$ subspace and converting to the coupled basis gives the quintet zero-field Hamiltonian as

$$\hat{H}^{(2)}_{zfs}/h = \mathbf{S}^T \cdot \mathbf{D}_q \cdot \mathbf{S} \quad , \tag{4.2}$$

where $\mathbf{S} = (\hat{S}_x, \hat{S}_y, \hat{S}_z)$ are the Pauli spin operators for total spin-2.

4.2 General tensor transformation from uncoupled to coupled representation

We describe a general transformation of tensor components from a representation for an uncoupled pair of spins $\hat{S}^{(a)}$ and $\hat{S}^{(b)}$ to the coupled total-spin representation $\hat{\mathbf{J}} = \hat{\mathbf{S}}_a + \hat{\mathbf{S}}_b$ upon projection into the highest-spin $J = S_a + S_b$ manifold. In the uncoupled basis the Hamiltonian is written

$$\hat{H}^{(S_a\otimes S_b)} = \sum_{ij} D^{(a)}_{ij}\hat{S}^{(a)}_i\hat{S}^{(a)}_j + \sum_{ij} D^{(b)}_{ij}\hat{S}^{(b)}_i\hat{S}^{(b)}_j + \sum_{ij} D^{(m)}_{ij}\hat{S}^{(a)}_i\hat{S}^{(b)}_j \quad , \tag{4.3}$$

where $\mathbf{D}^{(a)}$ describes the fine-structure of spin-a, $\mathbf{D}^{(b)}$ describes the fine-structure of spin-b, and $\mathbf{D}^{(m)}$ describes their inter-spin interactions.

4.2.1 Landé factor derivation

In the case of strong coupling ($J \gg g\mu_B SB$) one can transform Zeemann terms of the Hamiltonian for two spins S_a and S_b in the similar way, as for dipolar coupling in Eq. 4.2:

$$\mathbf{S}_a^T\cdot\mathbf{D}_t\cdot\mathbf{S}_a + \mathbf{S}_b^T\cdot\mathbf{D}_t\cdot\mathbf{S}_b + \mathbf{S}_a^T\cdot\mathbf{D}_{tab}\cdot\mathbf{S}_b \rightarrow \mathbf{S}^T\cdot\mathbf{D}_q\cdot\mathbf{S}, \tag{4.4}$$

$$g_a\mu_B\mathbf{S_a}\cdot\mathbf{B} + g_b\mu_B\mathbf{S_b}\mathbf{B} \rightarrow g_J\mu_B\hat{\mathbf{J}}\mathbf{B} \tag{4.5}$$

thus switching to tensor representation. Projecting into $J = S_a + S_b$ manifold resembles a lot to Landé g-factor derivation. In this case instead of having two spins $\hat{S}_{(a)}$ and $\hat{S}_{(b)}$ one has spin $\mathbf{S}$ and orbital $\mathbf{L}$ momenta of an atom, but the main idea remains the same. The total angular momentum is composed of these two momenta:

$$\mathbf{J}_{Lande} = \mathbf{S} + \mathbf{L} \quad , \tag{4.6}$$

$$\rightarrow \mathbf{J} = \mathbf{S}_a + \mathbf{S}_b \tag{4.7}$$

Then the total magnetic dipole momentum can be found through spin and orbital magnetic momenta:

$$\mu_{\mathbf{a}} = -\mathbf{S}_a g_a \mu_B/\hbar \quad , \tag{4.8}$$

$$\mu_{\mathbf{b}} = -\mathbf{S}_b g_b \mu_B/\hbar \quad , \tag{4.9}$$

$$\mu_{\mathbf{J}} = -\mathbf{J} g_j \mu_B/\hbar = \mu_{\mathbf{a}} + \mu_{\mathbf{b}} \quad , \tag{4.10}$$

where g_a and g_b are gyromagnetic ratios of spin momenta values to the angular momentum.

So it is clear that $g_J\mathbf{J} = g_a\mathbf{S}_a + g_b\mathbf{S}_b$ after reducting $\mu_B/\hbar$. To obtain g_J we can take a dot product of both sides of this formula to $\mathbf{J}$:

$$g_J\mathbf{J}\cdot\mathbf{J} = g_a\mathbf{S}_a\cdot\mathbf{J} + g_b\mathbf{S}_b\cdot\mathbf{J} \quad , \tag{4.11}$$

$$g_J J^2 = g_a(S_a^2 + \mathbf{S}_b\cdot\mathbf{S}_a) + g_b(S_b^2 + \mathbf{S}_b\cdot\mathbf{S}_a) = \tag{4.12}$$

$$= g_a(S_a^2 + \frac{1}{2}(J^2 - S_a^2 - S_b^2)) + g_b(S_b^2 + \frac{1}{2}(J^2 - S_a^2 - S_b^2)) \quad , \tag{4.13}$$

here we used the fact that $\mathbf{S}_a\cdot\mathbf{S}_b$ can be expressed via J as:

$$\mathbf{S}_b\cdot\mathbf{S}_a = S_b J - S_b^2 = J^2 - JS_a - S_b^2 = J^2 - S_aS_b - S_a^2 - S_b^2 \quad , \tag{4.14}$$

$$\rightarrow S_aS_b = \frac{1}{2}\left(J^2 - S_a^2 - S_b^2\right) \tag{4.15}$$

Knowing S_a^2, S_b^2, J^2 operators' eigenvalues:

$$||S_a^2|| = \hbar^2 S_a(S_a+1) \quad , \tag{4.16}$$
$$||S_b^2|| = \hbar^2 S_b(S_b+1) \quad , \tag{4.17}$$
$$||J^2|| = \hbar^2 J(J+1) \quad , \tag{4.18}$$
$$\tag{4.19}$$

we can find Landé g-factor as a coefficient for the projection of $\mathbf{S}_a$ and $\mathbf{S}_b$ on total momentum $\mathbf{J}$:

$$g_J J(J+1) = \frac{1}{2} g_a (J(J+1) + S_a(S_a+1) - S_b(S_b+1)) + \tag{4.20}$$
$$+ \frac{1}{2} g_b (J(J+1) - S_a(S_a+1) + S_b(S_b+1)) \quad , \tag{4.21}$$

and finally get:

$$g_J = \frac{g_a(J(J+1) + S_a(S_a+1) - S_b(S_b+1)) + g_b(J(J+1) - S_a(S_a+1) + S_b(S_b+1))}{2J(J+1)} \tag{4.22}$$

Therefore Landé g-factor derivation kind of gives as a rule to perform the transition to the coupled basis.

4.2.2 Coupled representation

In case of tensors calculations are trickier, but they follow the logic of Eq. 4.14. The spin operator products transform as:

$$\hat{H}^{(J)} = \sum_{ij} (\alpha_J^{(a)} D_{ij}^{(a)} + \alpha_J^{(b)} D_{ij}^{(b)} + \alpha_J^{(m)} D_{ij}^{(m)}) \hat{J}_i \hat{J}_j + \lambda_J \mathrm{Tr}[\mathbf{D}^{(a)} + \mathbf{D}^{(b)} - \mathbf{D}^{(m)}] \hat{I}_3 \quad , \tag{4.23}$$

where $\hat{I}_3$ is the 3 dimensional identity matrix. α and λ coefficients are obtained like g-factor in Eq. 4.22:

$$\alpha_J^{(a)} = \frac{S_a(2S_a-1)}{(S_a+S_b)(2S_a+2S_b-1)} \tag{4.24}$$

$$\alpha_J^{(b)} = \frac{S_b(2S_b-1)}{(S_a+S_b)(2S_a+2S_b-1)} \tag{4.25}$$

$$\alpha_J^{(m)} = \frac{2S_aS_b}{(S_a+S_b)(2S_a+2S_b-1)} \tag{4.26}$$

$$\lambda_J = \frac{S_aS_b}{2S_a+2S_b-1} \tag{4.27}$$

which can then be applied directly to the case of two $S_a = S_b = S = 1$ states coupled and projected into the spin-2 quintet manifold. This application yields $\alpha^{(a)} = \alpha^{(b)} = 1/6$ and $\alpha^{(m)} = \lambda = 1/3$.

4.3 Quintet zero-field tensor

Then the quintet zero-field tensor $\mathbf{D}_q$ in terms of the underlying triplet fine structure, inter-triplet distance, and dipolar interaction is given by

$$\mathbf{D}_q = \frac{D_T}{6}(\sum_{i=a,b} \hat{z}_i\hat{z}_i^T - \frac{2}{3}\hat{I}_3) + \frac{E_T}{6}\sum_{i=a,b}(\hat{x}_i\hat{x}_i^T - \hat{y}_i\hat{y}_i^T) - \Gamma_d(\hat{u}_{ab}\hat{u}_{ab}^T - \frac{1}{3}\hat{I}_3) \tag{4.28}$$

where once again $\Gamma_d = \frac{\mu_0\mu_B^2g^2}{4\pi|\vec{r}_{ab}|^3}$ and $\hat{I}_3$ is 3-dimensional identity matrix. The eigenvalues of $\mathbf{D}_q$ are ordered $|D_y| < |D_x| < |D_z|$, which gives $D_Q = \frac{3}{2}D_z$ and $E_Q = \frac{1}{2}(D_y - D_x)$ and the principal axes $\hat{x}_q, \hat{y}_q, \hat{z}_q$ (the eigenvectors of $\mathbf{D}_q$).

To understand the relationship between quintet fine structure parameters and the localization of the underlying triplet pair we take the physically relevant limit of collinear, axially symmetric triplet D-tensors with $\hat{u}_{ab} = (\cos(\beta)\sin(\alpha), sin(\beta)\sin(\alpha), \cos(\alpha))$ where Equation 4.28 above simplifies to give the parameters:

$$D_Q = \frac{D_T}{3} + \frac{\Gamma_d}{2}(1 - 3\cos^2(\alpha)), \tag{4.29}$$

$$E_Q = \frac{\Gamma_d}{2}\sin^2(\alpha), \tag{4.30}$$

in the limit of $D_T \gg \Gamma_d$. The two parameters, D_Q and E_Q thereby allow us to determine the polar angle α and triplet-triplet distance underlying the quintet state.

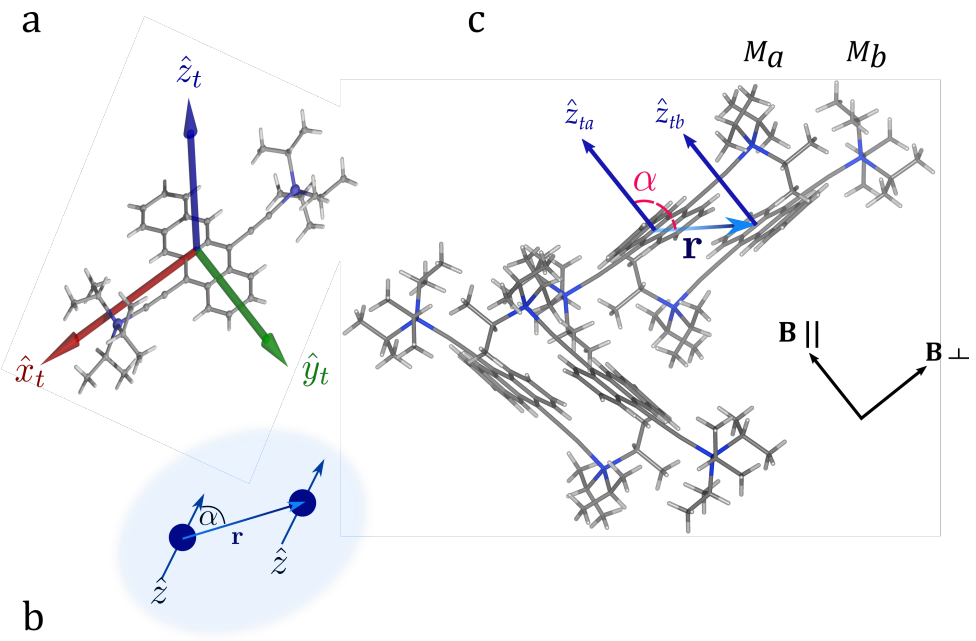

Figure 4.1: **a** Triplet exciton principle axes shown on a single TIPS-tetracene molecule. $\hat{z}_t$ axis is perpendicular to the molecular plane, while $\hat{x}_t$ and $\hat{y}_t$ axes are in-plane oriented with respect to the molecule's geometry. **b** Schematic representation of triplet $\hat{z}$ axes of two parallel molecules. α is an angle between these parallel axes and the inter-triplet distance vector $\bar{r}$. **c** TIPS-tetracene crystal cell containing four molecules. Considered molecules a and b have $\hat{z}_{ta,b}$ axes both parallel to an external magnetic field B. Figure is built using X-ray data provided by John Anthony (available in the Cambridge Structural Database [101]) and Mercury software [102]

To determine the remaining azimuthal angle we find the quintet fine structure axes are then transformed relative to the basis of the triplet as follows

$$\hat{x}_q = \sin\beta\hat{x}_t - \cos\beta\hat{y}_t, \tag{4.31}$$

$$\hat{y}_q = \cos\beta\hat{x}_t + \sin\beta\hat{y}_t, \tag{4.32}$$

$$\hat{z}_q = \hat{z}_t, \tag{4.33}$$

which is a rotation of the $\hat{x}_t, \hat{y}_t$ axes by β about $\hat{z}_t$.

As shown in Figure 4.1c, the crystal structure of TIPS-tetracene contains four orientationally inequivalent molecules yielding six possible pair sites in addition to non-crystalline defect sites. Both bound-pairs and free triplet excitons have been identified in this material with transient electron spin resonance, but where the bound pair is localized remains a key question. The theoretical framework above demonstrates that the parameters of the quintet fine structure (its principle values D_Q, E_Q and the orientation of the principal axes $\hat{x}_q$, $\hat{y}_q$, $\hat{z}_q$) are specific to the geometry of the underlying triplet pair and so each distinct potential pair site could be identified by its unique fine structure parameters

in a single crystal (note that these parameters are calculated explicitly from the crystal structure for each of the six possible pair states and reported in the following Chapter 5). In the following Chapters we will apply this framework to link the measured values and orientation of the D-tensors of the triplet and quintet states to their localization in the crystal structure of TIPS-tetracene.

The author would love to thank Alexei Chepelianskii and Leah Weiss for this theoretical part of the work.

Chapter 5

Optically detected magnetic resonance measurements on the intratriplet coupling

In this Chapter we present our experimental results and their interpretation based on theoretical model introduced in the previous Chapter 4. We performed various ODMR measurements to investigate different features of TIPS-tetracene samples described in different sections respectively. To follow the logic of our studies in this Chapter we will from time to time switch between thin film and crystalline samples, but now divide the Chapter into sample related parts.

5.1 Zero field features

We were first to measure TIPS-tetracene ODMR in the absence of applied magnetic field. The main restrain of high field measurements is the unknown angle between the magnetic field **B** and the fine structure tensor and the associated inhomogeneous broadening which limits the accuracy for the determination of the zero-field parameters D and E. Therefore zero-field ODMR is the method allowing to access zero-field splitting parameters. Indeed, as it has been discussed previously (2.2.1), in the presence of magnetic field the main contribution to resonant transition energy is due to Zeemann splitting term (2.2.1), whereas at zero field energy levels configuration is determined by the zero field splitting (2.2.1) - D-tensor and E-parameter. Nevertheless only zero-field ODMR gives an access to full values of these parameters, which will be discussed in Subsubsection 5.3.1.

Different spin species possess different D-tensors (see the Chapter 4), thus our triplet and quintet species should be spectroscopically distinguishable. Our measurements on crystalline sample containing both triplet and quintet states signatures are shown on

figure 5.1 reaffirm that.

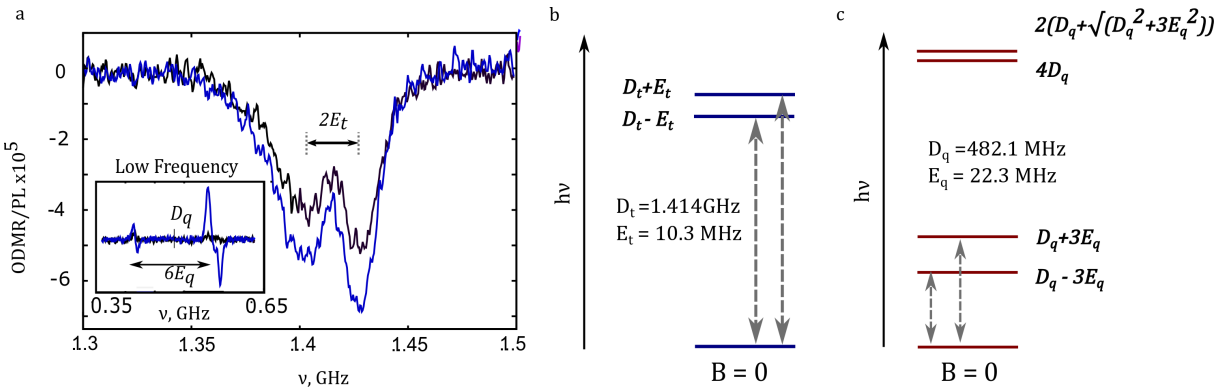

Figure 5.1: **a** Zero-field ODMR spectrum (in-phase channel - blue, out-of-phase - black) where the triplet transitions are split by the zero-field E-parameter and with centre frequency set by the D-parameter. **Inset**: Low frequency quintet transitions marked with zero-field splitting parameters (D_q, E_q) of the quintet pair-state. **b,c** Energy level diagram of triplet and quintet zero-field spin sublevels with the D and E parameters obtained from the experimental spectra shown on panel (a).

The main plot on the panel (a) presents zero field ODMR transitions assigned to the triplet states (frequency range $[1.3; 1.5]$ GHz). The split is due to non-zero E-parameter, which has not been reported thus far [73]. The inset is consistent of zero field ODMR transitions assigned to the quintet states (frequency range $[0.35; 0.65]$ GHz), where the resonance splitting is remarkably larger. For the both plots resonant dips centres are determined by D value and the splittings are proportional to corresponding E-parameter values. Thus figure 5.1a gives a direct access to D and E parameters for both triplet and quintet species.

The (b) panel of figure 5.1 shows energy levels diagrams for the triplet state in the absence of magnetic field. The $|m_{sT} = \pm 1\rangle$ levels appear shifted in energy by $D_t \pm E_t$ regarding $|m_{sT} = 0\rangle$, respectively. The sign of D_T was determined in Ref. [73] to be positive, which in turn determines E_T to be negative. The resolution of the splitting afforded by this technique allows E_Q and E_T to be measured for the first time, highlighting the sensitivity of the zero-field approach. The measurement of the E-parameters here is made possible by the reduced linewidths observed at zero-field relative to previous measurements under non-zero magnetic field. The $|m_{sQ} = \pm 1\rangle$ levels of the quintet state (Fig. 5.1c) are shifted by $D_q \pm 3E_q$ regarding $|m_{sQ} = 0\rangle$, respectively. The $|m_{sQ} = \pm 2\rangle$ levels are shifted by values $4D_q$ and $2(D_q + \sqrt{{D_q}^2 + 3{E_q}^2})$ and their transitions are not induced in the current conditions. The obtained zero field splitting parameters are marked on the schemes (Fig. 5.1b,c): $D_t = 1.414$ GHz and $E_t = -10.3$ MHz for the triplet states, $D_q = 482.1$ MHz and $E_q = 22.3$ MHz (obtained for the first time) for the quintet states.

In our system dipolar coupling between charges forming excitons is a key to molecular

structure. Indeed, magnetic dipoles even in the absence of external magnetic field do couple and vector nature of this coupling occurs strongly attached to molecular symmetry and relative positions of chromophores involved to exciton formation.

5.2 Non-zero field case

In the presence of magnetic field $B \gg 0$ triplet and quintet transitions in crystalline TIPS-tetracene can still be distinguished. Fig. 5.2a presents an example of single crystal sample ODMR spectra, measured at the constant frequency of 9 GHz and the magnetic field swept around a central position $B_0 = 3209$ G. There are both triplet and quintet resonant transitions splitted in the field due to Zeemann effect. These splittings are schematically illustrated on the panel (b) of the same figure: $|m_s = 0\rangle$ levels remain unchanged, meanwhile non-zero spin states $|m_s = \pm 1\rangle$ shift with the field leading to two transitions for each specie. These measurements confirm previously reported results [73, 74].

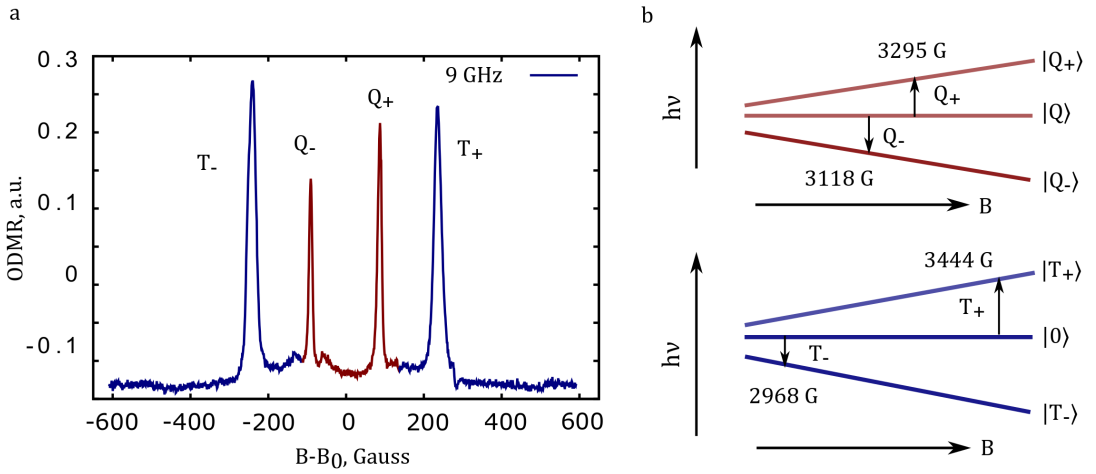

Figure 5.2: Zero field **a** ODMR spectrum at 9 GHz ($B_0 = 3209$ G), showing inner quintet transitions ($Q^{\pm}$) and the outer triplet transitions ($T^{\pm}$). **b** Energy levels of the triplet and quintet $m = 0, \pm 1$ sublevels as a function of field with transitions at 9 GHz marked with arrows to correspond to experimentally observed transitions on panel (a). Single crystal sample III provided by Leah Weiss and which spectra are measured in a collaboration with Alexei Chepelianskii and Leah Weiss.

5.3 Angles fitting

Having extracted the principal components of the triplet and quintet fine structure at zero-field, we now map the resonant frequencies as a function of magnetic field to determine the corresponding orientations of the principal axes. We performed measurement of ODMR

spectra in wide range of magnetic field to follow the dynamics of the resonant transitions.

Even though in the non-zero magnetic field leads to Zeemann term dominates the resonant transitions, by increasing the magnetic field we can learn about the fine structure tensor's orientation with respect to the magnetic field.

5.3.1 Samples' morphology analysis through triplet states field dependence

Let us start with considering simpler case of triplet states. A triplet exciton formed by singlet fission is located on a single molecule of TIPS-tetracene. Molecule's structure is known as well as triplet states' principal axes orientations. They are strongly attached to the geometry of a molecule. Due to TIPS-tetracene's symmetry $\hat{z}_t$ is oriented perpendicular to molecular plane, $\hat{x}_t$ and $\hat{y}_t$ are in-plane and follow main geometrical axes of the molecule.

As it has been mentioned before (see Subsubsection 2.2.1), the largest D-tensor's principal value is $\mathbf{D_z}$. Then for any kind of spin-species D-value observed in magnetic resonance measurements is determined as a projection of $\mathbf{D_z}$ on the external magnetic field $\mathbf{B}$. Above we have declared D_t value of $1.414GHz$, which gives us full value since it was obtained at $B = 0G$, whereas at non-zero magnetic field observed D-value is the largest and equals $1.414GHz$ at $\mathbf{D_z}||\mathbf{B}$ orientation and depends on the field in other cases.

This axial and field-dependence simplicity allows us to investigate molecules' orientations in samples of different morphologies. Since expected behaviour of parallel and perpendicular triplets' transitions with magnetic field, one can probe the morphology through the density of states (DoS) in-between these uttermost orientations.

We show results on three different types of samples - thin films, crystals and a single crystal - and see how the triplet spectra are very sensitive to these different morphologies. We observe a signal on the Y-channel (out-of-phase) when AM frequency f_{AM} is chosen to be slow enough compared to the inverse lifetime of the triplets (as mentioned in the Subsection 3.0.2, lifetimes of triplets and quintets are $\tau_t = 690$ μs and $\tau_q = 25$ μs [38].

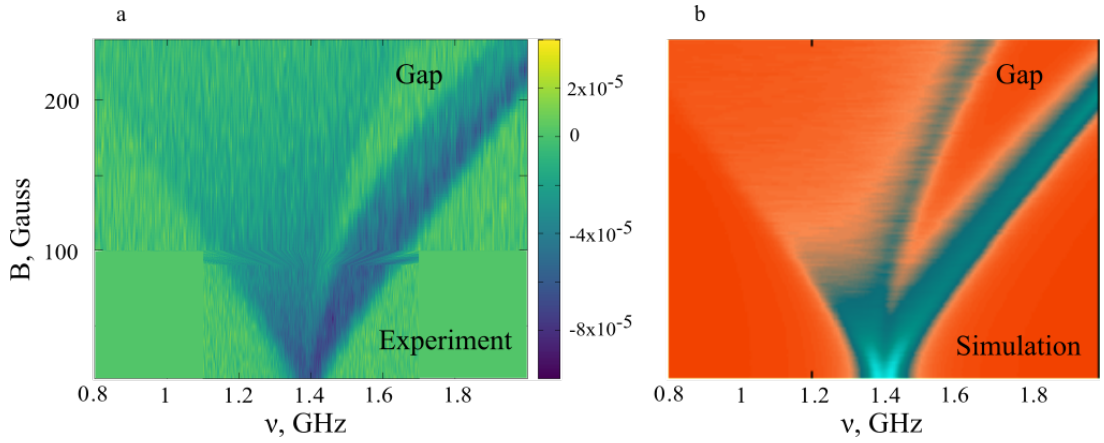

Figure 5.3: **a** Thin film TIPS-tetracene sample Y-channel (out-of-phase) ODMR map. **b** ODMR map calculated for a disordered sample using D_t and E_t values from Subsection 5.1.

To start with we measured ODMR spectral map of thin film TIPS-tetracene sample (sample I) in field up to 240.0 Gauss in a frequency range between 0.8 : 2.0 GHz (Fig. 5.3a). It reveals two lines centered around 1.4 GHz at $B \sim 0$ Gauss. This position in frequency is in agreement with the $D_t = 1.414$ GHz obtained in the Subsection 5.1, manifesting triplet origin of the transitions. One can notice that these transitions remarkably broaden with the field have a prominent gap, broaden as well in the field and tending to higher frequency range - zero DoS area, which appears to be orientationally forbidden. Theoretical calculation of randomly oriented spin-1 species transitions, using $D_t = 1.414$ GHz and $E_t = -10.3$ MHz values from Subsection 5.1 is shown on figure 5.3b. The calculated map is in a good agreement with the experiment on the panel (a), revealing two broad lines with the orientational gap. This theoretically approved gap allows us to determine spin-1 perpendicular and parallel (see Fig. 4.1c) orientations' field dependence, which we will discuss later in this subsubsection.

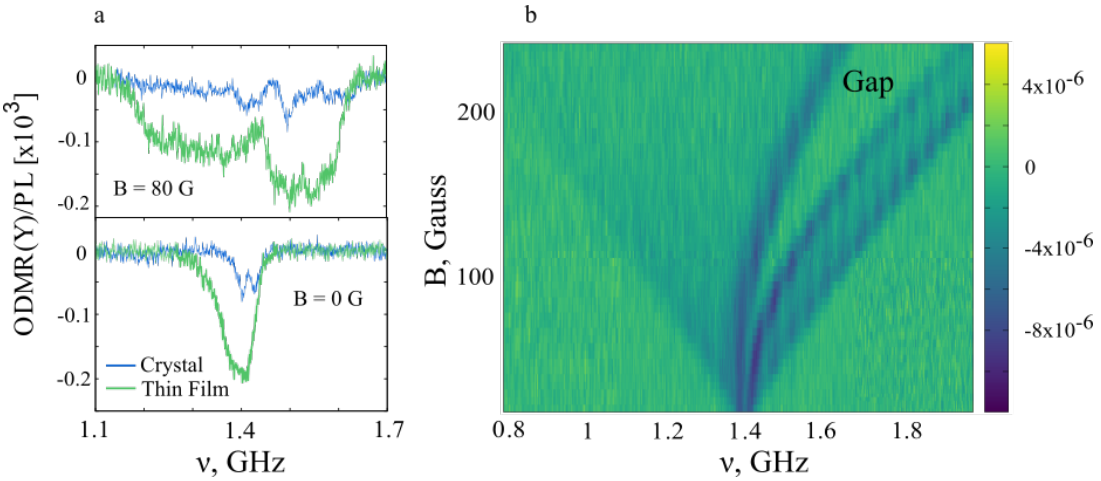

Figure 5.4: **a** Crystalline (Sample II) and thin film (Sample I) TIPS-tetracene Y-channel ODMR linewidths comparison at $B = 80$ and 0 Gauss. Thin film spectrum does not resolve zero field splitting by $2E_t$, clearly seen in the crystalline spectrum (corresponds to Fig. 5.1a). **b** Crystalline TIPS-tetracene (sample II) Y-channel ODMR map.

Crystalline sample (sample II) ODMR map measured in the same conditions reveal similar behaviour of the triplet transitions (Fig. 5.4), nevertheless the lines are narrower - instead of an inhomogeneous broadening this sample shows prominent peak and resolves initial zero-field splitting. Panel (a) on the figure 5.4 shows a linewidth comparison for these two samples. However at non-zero field ($B = 80$ Gauss) crystalline spectrum still has a non-zero ODMR signal intensity down to ~ 1.1 GHz, but it remains much smaller than the prominent resonance at ~ 1.47 GHz splitted due to zero field splitting and Zeemann effect. At zero field crystalline sample spectrum resolves zero field splitting (see Fig. 5.1a for more details), whereas broadened thin film spectrum does not. Full map (up to $B = 240$ Gauss) evidences more discreet distribution of states than the one on figure 5.3a. This is due to samples' morphology. The thin film sample may contain some particularly oriented domains in its' volume, yet in such case one cannot neglect top and bottom surfaces, which seem to be highly disordered due to a formation at media interfaces (glass - TIPS-tetracene and TIPS-tetracene - gas). Crystalline sample II is rather ordered as highly ordered bulk prevails surfaces. Although not being a singe crystal it may still have some differently oriented domains compared to the bulk, as well as surface damages due to the sampleholder may cause a powder formation. The above mentioned gap remains present in the crystalline sample - it is not dependent on a sample morphology. So this inner gap and outer limits for triplet transitions present more or less visibly in both discussed samples Knowing the behaviour of resonances in the two uttermost magnetic field orientation with respect to $\hat{z}_t$ axis (Fig. 4.1c) cases - perpendicular and parallel , one can consider a non-zero DoS between them as sign of disorder. Figure 5.5 shows the difference between disordered (thin film, panel (a)), ordered (crystalline, panel (b))

and highly ordered (single crystal sample III provided by Leah Weiss and which spectra are measured in a collaboration with Alexei Chepelianskii and Leah Weiss, panel (c)) samples' triplet transitions. Panel (c) indicates that $E(10MHz) \ll D(1.4GHz)$ allowing near-linear growth of the splitting for $B||$ to the molecular z-axis.

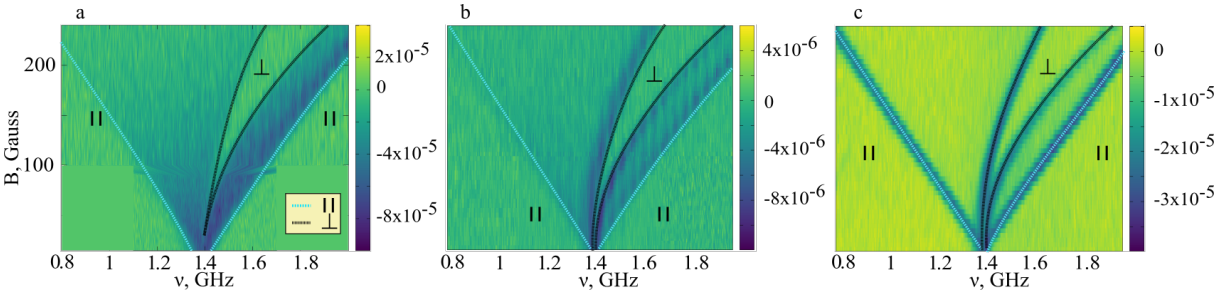

Figure 5.5: Morphology revealing examples of ODMR maps measured in sweeping magnetic field. Transitions on all the panels are attributed to the triplet states. **a** Thin film TIPS-tetracene sample Y-channel (out-of-phase) ODMR map. Non-zero DoS between the uttermost perpendicular and parallel to the external magnetic field **B** manifests presence of variously oriented species - the disordered sample. **b** Crystalline TIPS-tetracene sample Y-channel map. Clearly pronounced uttermost orientations and smaller DoS between them designate highly ordered structure. **c** Single crystal TIPS-tetracene sample Y-channel map with sharply pronounced transitions revealing even higher ordered morphology.

It is clearly seen that there is more signal (and thus more states) between the uttermost cases on the thin film sample map (Fig. 5.5a), than on the crystalline samples maps (Fig. 5.5b,c), confirming our suggestion. Apart from that, morphology studies let us determine magnetic field orientation with the respect to crystalline samples II and III facets, this information will be used in the Section 5.4.

5.3.2 Quintet states spectral justification

If 2D ODMR spectra can probe triplet orientation, why wouldn't it help to investigate quintet principle axis? Measured quintet transitions map is shown on figure 5.6a. The confirmation of the assignment of the ~ 0.4 GHz transitions to a quintet state and extraction of the orientation of the quintet fine-structure axes in the lab frame is obtained by fitting this map with the spin transitions predicted by the fine structure parameters D_q and E_q determined at zero-field (see Section 5.1) with the orientation as input. We describe the orientation of principal axes in the lab frame using the polar angle θ and azimuthal angle ϕ of the magnetic field within the axes (see the inset on Fig 5.6b) which act as fitting parameters for the simulated spin transitions as a function of field strength. The rough fitting revealed θ angle to be $\sim 90°$, thus only ϕ angle needed to be found through more precise fitting of the experimental spectra (for the appropriate code see the

Section 13.2 of the Appendix). Fig. 5.6b illustrates magnetic field orientation effect on the spectral lines behaviour: some experimental points from the map on panel (a) are plotted in purple overlaying calculated angle dependence for some the quintet transitions.

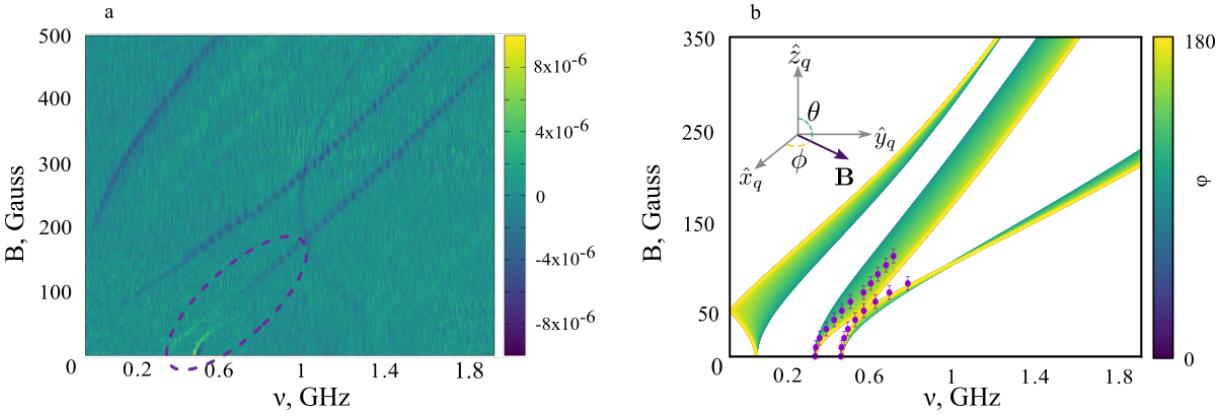

Figure 5.6: **a** ODMR map associated with the quintet state. Signal has been isolated by subtracting the out-of-phase (Y-channel) signal from the in-phase signal (X-channel) to remove triplet contributions. **b** Low frequency experimental lines from panel (a) (purple dots with errorbars) plotted above the quintet angle dependence calculated by Leah Weiss. **Inset**: Magnetic field **B** orientation in the D_q-tensor axes determined by ϕ and θ angles.

Thus the conclusive Hamiltonian for the quintet in the Sample II is the following:

$$\hat{\mathcal{H}}_{\mathcal{Q}}/h = \frac{g\mu_B}{h} B\hat{S}_z + D_q\hat{S}_y^2 + E_q((\cos\phi\hat{S}_z + \sin\phi\hat{S}_x)^2 - (\cos\phi\hat{S}_x - \sin\phi\hat{S}_z)^2) \qquad (5.1)$$

considering the principal component of D_q-tensor considered perpendicular to **B** oriented along the $\hat{c}$ crystallographic axis - $\theta = 90°$.

The Hamiltonian 5.1 and the obtained $\phi = 30°, \theta = 90°$ angles with the tolerance of $\pm 5°$ reveal the quintet state energy level diagram evolution with B (Fig. 5.7a, calculated by the author in Wolfram Mathematica [103]). Comparing it to the spectral map on the panel (b) we can assign observed transitions to certain levels. There are 10 possible transitions between the five quintet spin sublevels, which are overlaid on the ODMR map on the panel (b) (note that transition visibility depends on population and selection rules and transitions *1*, *2*, *6* and *7* are not observed in the experimental data). Calculations perfectly fit the experimental data. We checked more precisely the relevancy of attributing lower frequency transitions (3 and 4 on Fig. 5.7b) to quintet states by comparing triplet excitons DoS calculations (based on the code presented the Section 13.2 of the Appendix) to the experimental ODMR map. The shaded areas on the figure 5.7c illustrate non-zero probability states predicted by the DoS calculations. It fails to delineate the behaviour of these transitions and expects the level anticrossing to appear at both higher frequency and magnetic field.

The resulting calculated transitions for triplet excitons are plotted in black on the Fig. 5.7d and labeled with numbers, corresponding to transitions between field-splitted energy levels sketched on the bottom diagram on the panel (a). Their evolution with field are consistent with: $\theta_t = 0°$ and $\theta_t = 90°$ with the latter perpendicular component more prominent (calculated transitions for $\theta_t = 90°$ are plotted in black) and the $\theta_t = 0°$ consistent with the presence of a weak powder background. This correlates with the morphology studies presented above. Note that ϕ_t could not be extracted reliably as $E_T \ll D_T$ and this parameter was not required for subsequent analysis.

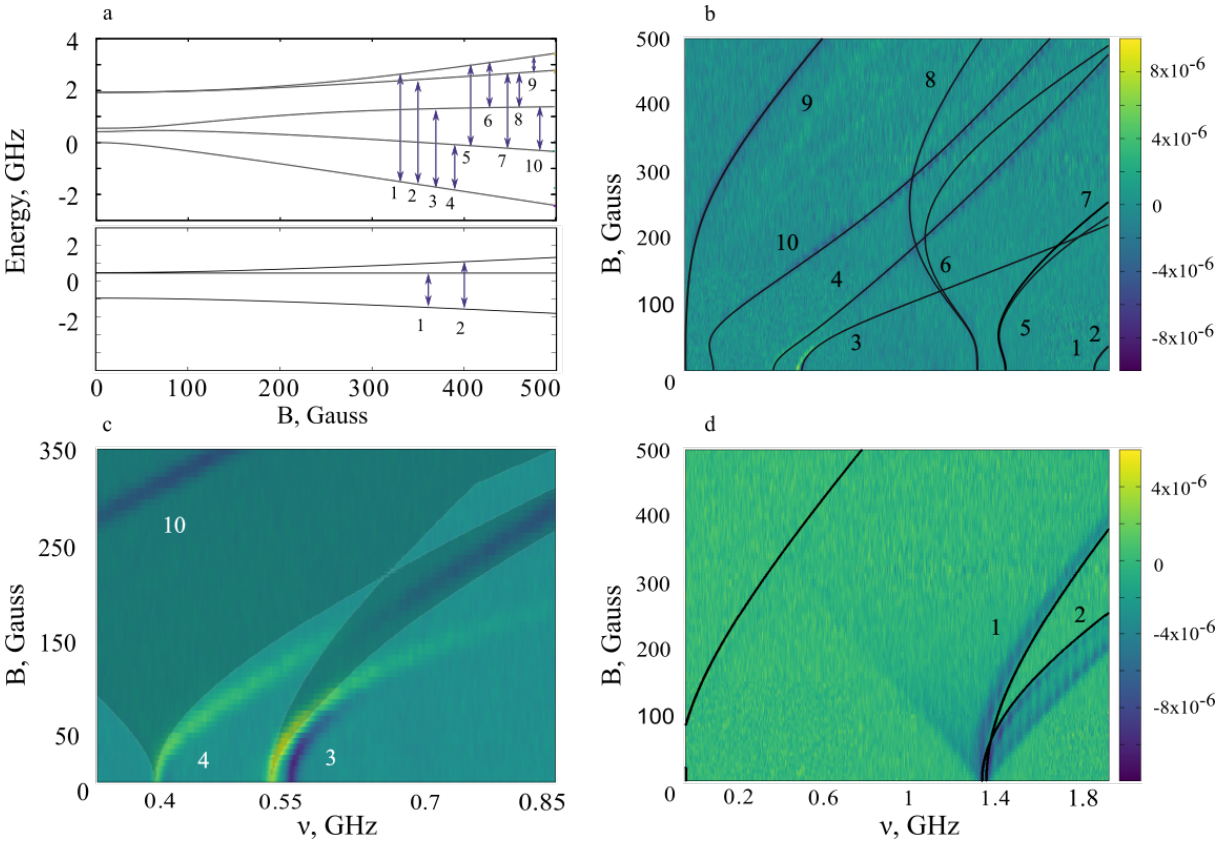

Figure 5.7: **a** Energy level diagrams for the quintet an triplet states as functions of magnetic field B. Arrows indicate transitions, corresponding to numerated lines on panels (b) and (d). **b** Quintet ODMR map from Fig. 5.6a with overlay of simulated transitions. **c** Zoomed map of low frequency transitions 3, 4 and 10 from panel (a) measured with higher MW power. Shaded zones represent calculated areas of non-zero density of states for triplet excitons. Experimental lines are outside of these areas proving that the transitions don't belong to the triplet species. **d** Y-channel ODMR map of the transitions attributed to the triplet state with overlay of calculated transitions for the triplet state in black.

5.4 Molecular structure

Molecular structure of quintet states may be obtained with D and E parameters for triplets and quintets, X-ray data provided by John Anthony (available in the Cambridge

Structural Database [101]) and the magnetic field orientation with the respect to crystalline samples facets determined in the Section 5.3.1. In this Section we show the comparison of this type of calculations and the results extracted from out measurements. TIPS-tetracene crystal cell contains four molecules packed with two approximately parallel dimers each rotated with respect to the other by $\sim 90°$ about the $\hat{c}$ crystalline axis (Fig 5.8a). So the quintet may be formed by triplets six different ways: $TT_{1,2}$, $TT_{1,3}$, $TT_{1,4}$, $TT_{2,3}$, $TT_{2,4}$, $TT_{3,4}$. For each triplet pair (dimer) there will be a particular r_{ab} vector defining a quintet's principal $\hat{z}_q$ axis (Fig 5.8b). As it was discussed before (see Subsubsection 2.2.1 and Section 4), this axis determines quintet D-tensor's largest component and therefore its' projection on **B**.

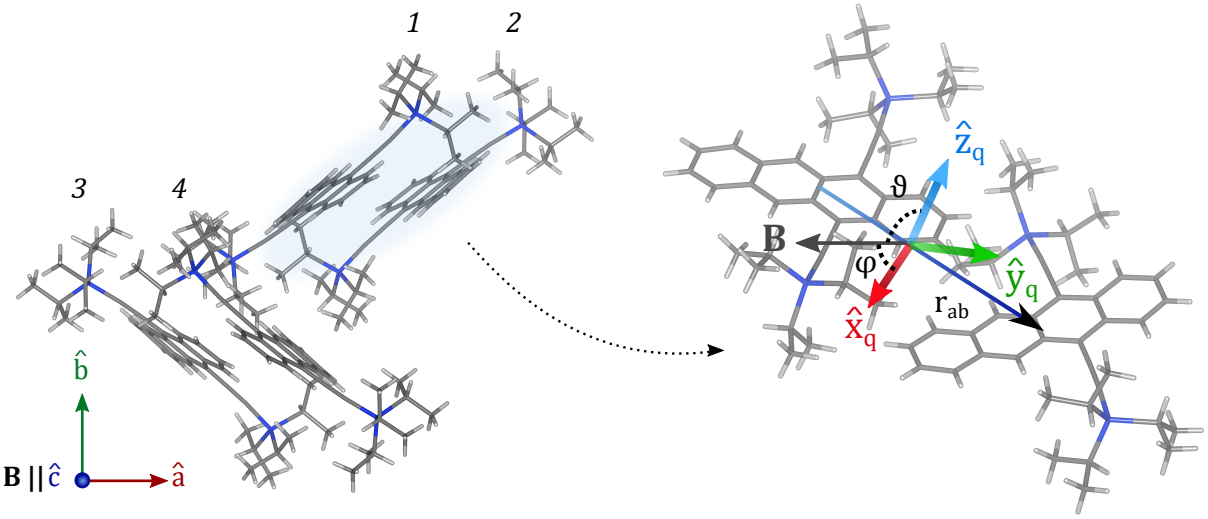

Figure 5.8: Sample II orientation. **a** TIPS-tetracene crystal cell (the same picture as Fig. 4.1c), containing four molecules (numerated). $\hat{a}$, $\hat{b}$ and $\hat{c}$ are the crystal axes. According to our angles fitting magnetic field **B** is parallel to $\hat{c}$. **b** The principal axes $\hat{x}_q$, $\hat{y}_q$ and $\hat{z}_q$ of the quintet state's formed by a pair of triplets on molecules *1* and *2* ($T_{1,2}$). We observed the θ angle between **B** and $\hat{z}_q$ to be $\sim 90°$ and the ϕ angle between **B** and $\hat{x}_q$ to be $\sim 30°$. Figure is built using X-ray data provided by John Anthony (available in the Cambridge Structural Database [101]) and Mercury software [102].

Knowing the intermolecular distances extracted from the crystal structure X-ray diffraction [101] of the four molecules we calculated r_{ab} for each dimer (using Wolfram Mathematica software [103]), from which we accessed their D_q, E_q and ϕ and θ angles. These calculations were performed independently by the author, Alexei Chepelianskii and Leah Weiss and lead to the same results. Calculated and experimentally observed values are given in the Table 5.1. These calculations reveal that the quintet transitions seen in the experiment (Figures 5.6a and 5.7b) belong to triplet pairs $TT_{1,2}$ and $TT_{3,4}$ for the sample II. Interestingly, these dimer configurations correspond to the most closely π-stacked dimers in the crystal suggesting that this geometry is favorable for binding of the triplet

pair state.

Table 5.1: Calculated parameters for six possible dimers in TIPS-tetracene crystal structure with $D_T = 1414.0$ MHz and $E_T = -10.5$ MHz from the measured zero-field values with angles given for $\mathbf{B} \parallel \hat{c}$ between $\mathbf{B}$ and $\hat{z}_q$ (θ_q) and $\hat{x}_q$ (ϕ_q). The final row shows the corresponding experimental observations, consistent with the predicted values of $TT_{1,2}$ and $TT_{3,4}$. This description of the orientation of the triplet pair relative to the crystal facets sets the foundation for orientation-selective, all-optical experiments where faster time-resolution would allow investigation of the transient localization of the pair-state.

heightdimer	$\lvert D_q \rvert$, MHz	$\lvert E_q \rvert$, MHz	θ_q	ϕ_q	r_{ab}, Å
$TT_{1,2}$	474.0	22.5	91.6°	30.6°	10.0
$TT_{1,3}$	227.5	72.4	13.5°	77.8°	10.5
$TT_{1,4}$	250.4	42.7	15.5°	84.7°	9.7
$TT_{2,3}$	234.8	62.0	13.8°	90.8°	15.7
$TT_{2,4}$	245.5	69.7	11.0°	78.9°	17.7
$TT_{3,4}$	474.0	22.5	88.4°	30.6°	10.0
Exp.	482 ± 1	22 ± 1	$90.0 \pm 5°$	$30 \pm 5°$	10 ± 1

5.5 Single crystal

To testify our model we performed the same calculations (see the Section 13.2 of the Appendix) for the single crystal sample (sample III). In these measurements performed in the collaboration with Leah Weiss the magnetic field $\mathbf{B}$ orientation was found to be in $\hat{a}\hat{b}$ crystalline plane (Fig. 5.9d), which gives θ angle between the field and principal quintet axis $\hat{z}_q$ either $\sim 90°$ for a dimer $TT_{3,4}$ or $\sim 0°$ for a dimer $TT_{1,2}$. It means that in this case the resulting map should be consistent of two components: the first one will correspond to the Sample II transitions (Fig. 5.7b) with $\theta = 90°$ and the second one with $\theta = 0°$. In the second orientation ϕ angle doesn't affect the calculated transitions. Figure 5.9c represents energy level diagram of the dimer $TT_{3,4}$ up to 500 Gauss. On figure 5.9a we plotted only those transitions for this dimer which have rather high probabilities, as the experimental map contains a few transitions. We assume it to be due to lack of MW power penetrating the bulk of the sample.

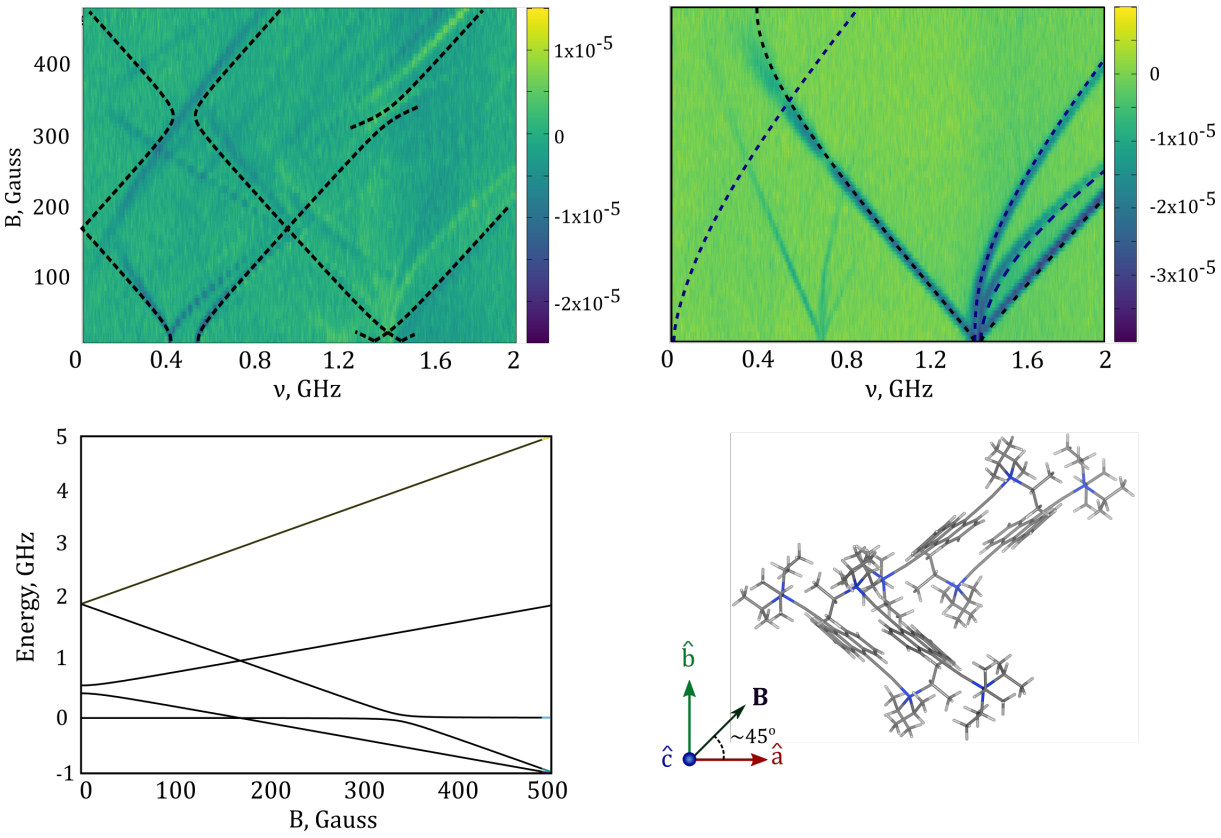

Figure 5.9: **a** Single crystal (sample III) quintet states ODMR map with calculated high probability transitions for the dimer $TT_{1,2}$ with $\theta = 0°$. **b** Triplet states ODMR map with calculated transitions for both parallel and perpendicular orientations. Lines around 0.7 GHz are just a replica of 1.4 GHz transitions due to MW amplifier. **c** $\theta = 0°$ quintet energy levels diagram up to 500 Gauss very different from one on Figure 5.7a. **d** Magnetic field **B** orientation sketch for the Sample III.

To sum up, in this Chapter we presented ODMR studies of triplet and quintet states. We got D and E parameters for both excitations from zero-field measurements and showed their energy levels diagrams. Then we showed that 2D ODMR spectra can probe samples' morphology. It is due to comprehensive understanding of triplet state's geometry on the TIPS-tetracene molecule - the main component of the triplet dipolar coupling tensor D_{tz} on four molecular sites of the crystal yield two possible uttermost orientations in relation to the external magnetic field - parallel and perpendicular. Therefore the density of states in the intermediate of two these uttermost orientations represents the state of disorder in the sample.

We performed the same 2D studies on the quintet states. With the theoretical model derived in the previous Chapter 4 and zero-field splitting parameters measured in the absence of magnetic field we carried out the experimental data fitting in order to find polar and azimuthal angles defining the orientation of the main component of the quintet dipolar coupling tensor D_{qz} with respect to the applied magnetic field. Calculated energy

levels diagram and corresponding predicted transitions were in the perfect agreement with the experimental spectra. Combining these results with a crystallographic information on molecules packing in the TIPS-tetracene, we indicated specific molecular sites hosting quintet excitation.

Chapter 6

High field Magneto-Photoluminescence investigation of the intertriplet coupling

6.1 Magneto-photoluminescence origins

As discussed in the Chapter 2 singlet excitations are photoactive in terms that they can be induced in TIPS-tetracene by photon absorption and undergo relaxation through a photon emission. Triplet pair fusion into singlet followed by photo-emission at certain combinations of magnetic field and applied MW frequency let us investigate triplet and quintet states through changes in PL (ODMR). Magneto-photoluminescence (magneto-PL) measurements are quite similar to ODMR: in this case PL (spectrally-resolved or integrated) is measured as a function of magnetic field at fixed MW frequency. These studies aimed to obtain exchange coupling values for triplet pairs.

6.2 Experiment details

Magneto-photoluminescence (magneto-PL) measurements [104] were performed in collaborations with Sam Bayliss, Leah Weiss, LNCMI (Toulouse, France) and HFML (Nijmegen, Netherlands). The Disseration author participated in the experimental part. Crystalline samples were excited by 532, 514 or 485 nm laser illumination, yielding similar results across the range. Laser light was again cut off by long-pass filter. In integrated PL measurements collected signal was detected by the avalanche photodetector as above. Whereas combination of a monochromator with a nitrogen-cooled CCD was used for

spectrally resolved measurement. Integrated and spectrally resolved experiments to 68 T were performed under pulsed magnetic field at LNCMI. Spectrally resolved measurements up to 33 T were performed under steady-state fields at the HFML. Samples were either immersed in liquid helium or cooled via exchange gas with a surrounding helium bath, giving base temperatures of $\sim 1.1, 1.4, 2$ K.

6.3 Intertriplet coupling

This section consists of brief review of the published results of a collaboration, for more details see Ref. [104]. Above we focused on triplet-exciton pair intratriplet coupling. Now we switch to the intertriplet (exchange) spin coupling, represented by the third term of the Hamiltonian below [105, 106]:

$$\hat{\mathcal{H}} = \sum_{i=a,b} g\mu_B \mathbf{B_0}\hat{\mathbf{S}}_i + D(\hat{S}_{i,z}^2 - \hat{\mathbf{S}}_i^2/3) + J\hat{\mathbf{S}}_a\hat{\mathbf{S}}_b \tag{6.1}$$

Considering strong coupling ($J \gg D$) case (Note that further we will neglect the modulus sign and use simply J instead of $|J|$), the eigenstates at zero magnetic field are the pure spin states consisting of singlet, triplet and quintet effective states, where singlet one is initially populated due to singlet fission spin conservation. In the absence of magnetic field these states are separated by exchange energy. Then application of an external magnetic field tunes non-zero spin sublevels of the triplet and quintet excitations into resonance with the singlet sublevel due to Zeemann effect (Fig. 6.1a).

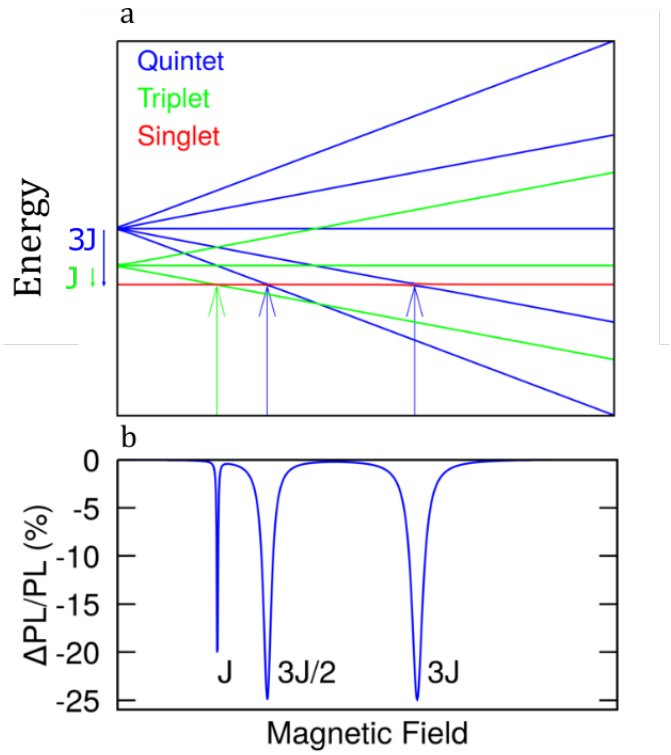

Figure 6.1: Exchange-coupled triplet pair level anticrossing. Adapted from [104]. **a** sublevels of the spin species with $S = 0$, $S = 1$ $S = 2$ formed by triplet pairs splitting in magnetic field due to Zeemann effect. J is the exchange interaction strength. **b** Resonant reduction of TIPS-tetracene PL at field values proportional to J due to magnetic field tuning quintet and triplet sublevels on panel (a) into near-degeneracy with the singlet state.

At these particular positions in field singlet state hybridisation with the triplet and quintet states should lead to PL reduction (Fig. 6.1b)[107, 108, 109, 104]. In magnetic field units singlet-triplet crossing resonance occurs at J, singlet-quintet - at $1.5J$ and $3J$. This dependence remains valid the same for any exchange coupling strength $J \gg D$, thus high field magneto-PL studies allow to direct measurements of exchange coupling strength.

We performed magneto-PL measurements of crystalline TIPS-tetracene sample up to 60 T at 1.4 K to observe these PL-reduction caused resonant dips in the integrated PL. Figure 6.2b shows the changes in integrated PL, where $\Delta PL/PL = [PL(B) - PL(0)]/PL(0)$. Below 1 T, the conventional singlet fission magnetic-field effect is observed, indicative of weakly coupled triplet pairs, while at $\geq$ 15 T spectrum contains two sets of resonances below 15 T - $J_1/g\mu_B = 3.78$, 5.60 and 11.20 T labeled in blue (TT_1) and $J_2/g\mu_B = 2.96$, 4.35 and 8.65 T labeled in red (TT_2) zoomed in the inset - and one higher field set. All these resonances follow the predicted ratio 1 : 1.5 : 3, thus manifesting several triplet

pairs with different J in the same sample: $J_1 = 0.44$ meV and $J_2 = 0.34$ meV.

Thus we could distinguish triplet pairs and extract their exchange coupling strength, though spectral characterization was still not achieved. For that one needs to clearly associate pairs with particular optical properties. We expect the PL-reduction to be specific for each triplet pair with certain J-value, since it implies different configurations affecting optical properties. As while intersystem crossing a pair doesn't contribute to integral PL, this should results in a kind of spectral hole burning, which is schematically represented on figure 6.2a.

What we could do to probe that was to switch to spectrally resolved measurements. To obtain spectral contribution of a certain triplet pair one needs to get a PL spectra at the resonant field position and out of resonance, but still close enough to it in field to exclude other effects: an average of two spectra at either side of the dip approximates non-resonant spectrum. Then subtracting the resonant spectrum from average non-resonant spectrum would give spectral hole associated to a particular triplet pair:

$$PL(B_{non-res}) = \left(PL(B_{left}) + PL(B_{right})\right)/2 \quad , \tag{6.2}$$

$$\Delta PL_{res} = |PL(B_{res}) - PL(B_{non-res})| \tag{6.3}$$

For one triplet pair all the dips expectedly give the same resulting spectrum - its' proper PL-contribution. We did that for three triplet pairs observed in the integrated spectrum on figure 6.2b.

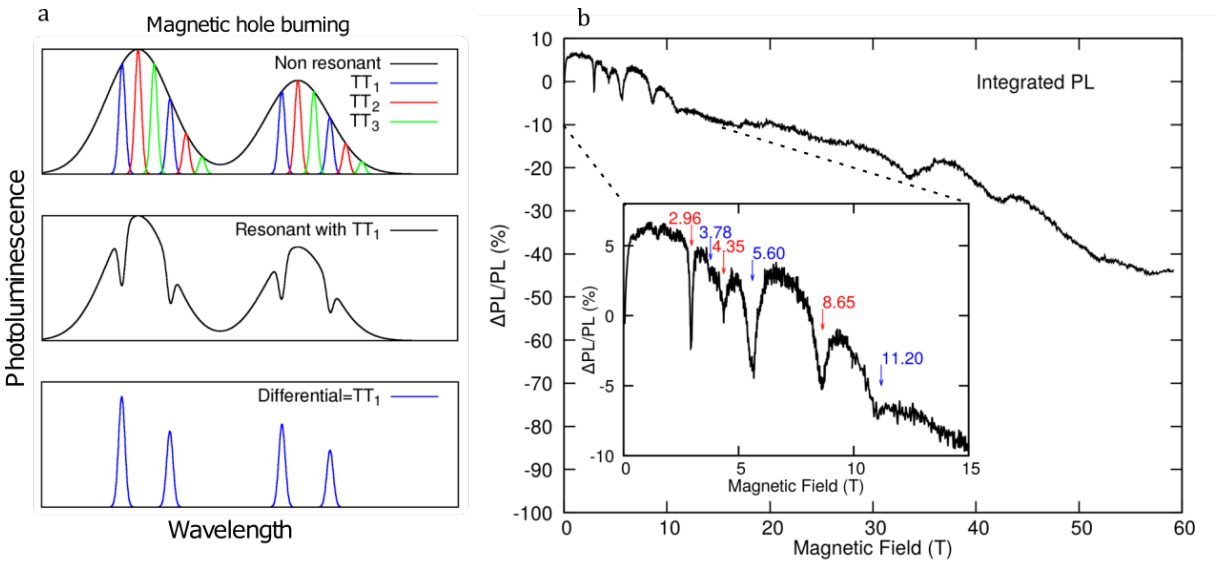

Figure 6.2: **a** Spectral holes linked to triplet pairs $TT_{1,2,3}$ created by field induced level anticrossing (Fig. 6.1). **b** Integrated magneto-PL spectrum measured at $T = 1.4$ K, revealing sets of resonant PL reduction associated with different exchange-coupled triplet pairs. $\Delta PL/PL = PL(B)/PL(0) - 1$. Adapted from [104].

This spectral hole burning allowed us to spectrally resolving interacting triplets thought their individual PL-spectra (Fig. 6.3). Higher energy region of TIPS-tetracene total PL spectrum (Fig. 6.3a) possesses three features at certain wavelengths $\lambda_1 = 562.5$ nm, $\lambda_2 = 564.9$ nm and $\lambda_3 = 567.1$ nm. Magneto-PL measurements at these wavelengths revealed sets of resonant dips following the same ratio of $1 : 1.5 : 3$ (fig. 6.3b-d). Their positions occured to be close to the resonances observed in the integrated spectrum (fig. 6.2b), so we assigned them to the same triplet pairs: TT_1 on panel (b) has a coupling of 0.44 meV ($J/g\mu_B = 3.79$ T) and TT_2 on panel (c) has 0.34 meV ($J/g\mu_B = 2.96$ T). Importantly magneto-PL measured at a fixed wavelength yields a particular set of resonances, except a slight mixture between TT_1 and TT_2 on panel (c), where $3J_1/2$ resonance of TT_1 is present - apparently it is due to J_1 and J_2 being relatively close to each other. λ_3 measurements on the inset of panel (d) revealed two higher field dips not following $1 : 1.5$ ratio at 33.4 and 42.0 T. Therefore we assing them to $1J$ dips for two different triplet pair coupled by 3.87 and 4.87 meV (also close enough J-values), respectively, and consider the rests of these sets not fitting in the taken field range. The spectra associated with sets of resonances of certainly exchange-coupled triplet pairs are given on figure 6.3e,f-h. From these resonant spectral changes, both the spin and optical properties of pair sites are therefore reconstructed.

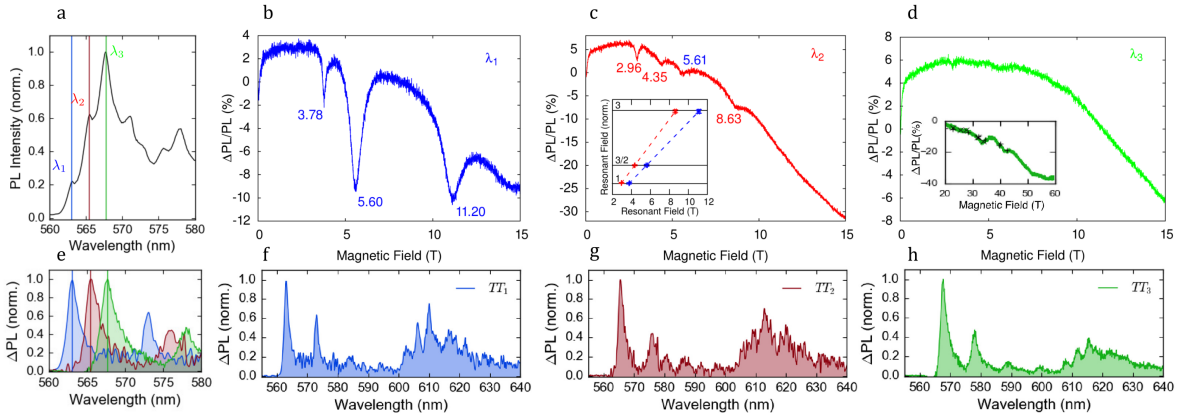

Figure 6.3: Extraction of PL spectra for different triplet pairs. Adapted from [104]. **a** TIPS-tetracene PL spectrum at 1.4 K. $\lambda_1 = 562.5$ nm, $\lambda_2 = 564.9$ nm, $\lambda_3 = 567.1nm$. **b-d** Magneto-PL measured for $\lambda_{1,2,3}$. **c-inset**: resonant dips positions following the ratio 1:1.5:3 J for TT_1 and TT_2. **d-inset**: Spectrally resolved measurements (black points) vs. integrated spectral trace (green line). **e** Overlaid $\lambda_{1,2,3}$ component spectra contributing to the one on the panel (a). **f-h** Extracted PL spectra associated with resonant dips on panels (b-d).

Specific spin pairs with distinct spectral and spin properties can therefore be disentangled in an ensemble measurement and their local environment and microscopic properties probed. This is the key principle of our approach to provide a spin- and site-selective measurement of organic spin pairs.

As a conclusion, in this Chapter we briefly introduced our collaborative results, published in 2018 (See the Ref. [104]). High field magneto-photoluminescence measurements allowed us to witness experimentally resonant PL reduction for triplet pairs with different exchange coupling strengths. Further spectrally resolved analysis allowed us to assign the PL reduction spectral dips to certain triplet pairs and define their spectral contributions.

Chapter 7

Conclusions on Part I

Nowadays scientific community has high expectations for material science to find direct and indirect salvations for increasing intensity of the modern world problems. Their scale ranges from global disasters, such as climate change and uncontrollable pollution, down to bio-compatible devices for innovative medicine of tomorrow. Organic and organic-inorganic composite materials remain the major trend for all the applications of this wide range. On a top of that neuron signal reading bio-transistors and other human body upgrading implants make people believe in trans-humanistic future of a mankind.

By now ecological solution of energy problems is the main application of organic semiconductors, but in any case their implementation requires deep knowledge and understanding of the origins of intrinsic spin processes that enlarge opportunities and increase efficiencies. Particularly understanding a connection between intermolecular structure and wavefunction localization is critical as it presents a pathway toward molecular engineering of pair states and their properties.

Our contribution to this evolution of knowledge is diverse studies of organic semiconductor TIPS-tetracene by optically detected magnetic resonance (ODMR), yielding rich information on the spin processes and intrinsic structure of the material.

Indeed, using one simple and powerful method which is highly affordable to set up even in a small laboratory - ODMR - we have accessed directly to one of the main interactions responsible for excited states formation and dynamics - excitons' dipolar coupling. This interaction is very weak, it is used as a probe for nm scale distances. For that we performed zero-field ODMR measurements, where Zeemann interaction is not present in the Hamiltonian, thus we reached pure zero-field splitting of non-zero spin states like triplet and quintet excitons. We obtained $D_t = 1.414$ GHz and $E_t = -10.3$ MHz for the triplet states, $D_q = 482.1$ MHz and $E_q = 22.3$ MHz measured for the first time for quintets and shown their energy level structures in the absence of perturbing external magnetic field, which are highly sensitive probes of underlying molecular structure.

Besides, knowing these spin species having different kinetics, we successfully separate and distinguish between their spectra. Therefore we could determine exact parameters for each type of excitation.

Studying such a key interaction as the dipolar coupling of triplet states allowed us to unambiguously probe TIPS-tetracene samples' morphology. Density of states of triplets oriented differently in relation to external magnetic field appeared to be a direct measure of a structural disorder.

While comprehension of triplet species seems to be rather complete, we wanted to go further and investigate formation of bi-exciton (quintet) state composed of two triplets. For that we developed both the theoretical and experimental approaches to connect intermolecular structure and bi-exciton localisation.

First we confirmed spin-2 origin of our ODMR spectra. Apart from raising phase-separable signals, triplet and quintet MR transitions behave differently in increasing magnetic field due to different multiplicities - mapping ODMR spectra in wide magnetic field range reveals spin Hamiltonian features for distinct species. We used quintet exciton Hamiltonian with dipolar coupling tensor parameters obtained from zero-field measurements to achieve quintet state's principal axes orientation in relation to the magnetic field - polar angle θ and azimuthal angle ϕ as fitting parameters. Resulting values we found are $\phi = 30°, \theta = 90°$ with the tolerance of $\pm 5°$.

Then the information was sufficient to calculate expected quintet MR transitions in sweeping magnetic field, since all the Hamiltonian parameters were determined. Reconstructing energy level structure change in field, we extracted exact transitions for every field value. Comparing these theoretical predictions with experimental results showed perfect matching.

Further on relying on X-ray studies of TIPS-tetracene crystal structure and our triplet and quintet species' orientations results then we could also calculate expected dipolar coupling tensor parameters for different molecular sites - as quintets are formed on pairs of molecules we looked over all the possible molecular combinations to determine experimentally observed species localisation. We succeeded to spot the exact molecular site contributing to our measurements.

Finally obtained dipolar tensor parameters, field orientation angles and intermolecular distances provided by previous X-ray measurements defined quintet state's geometry and location in TIPS-tetracene crystals distinctly.

The approach described here is not only applicable to singlet fission systems, but will provide a means of capturing the underlying structure of bi-excitons in a range of applications from multiple-exciton generation to spectral conversion approaches involving triplet-triplet annihilation [62, 110]. While in this case we have used the native dipolar

structure as a probe of the electronic structure of excitons, we note that the connection explored here presents a means of tuning spin energy levels in organic systems more broadly. Beyond the use of the dipolar spin interactions as a window into the geometry of the triplet-pair state, this work highlights the sensitivity of the effective spin fine structure of the coupled spin state. Tuning spin energy levels and zero-field interactions is critical in spin-based applications, for example in tuning the amplification frequency in the newly emerging class of organic molecular masers [111, 112]. The sensitivity of the effective spin Hamiltonian to intermolecular geometry therefore opens up opportunities to tune spin parameters via crystal structure engineering spin-based organic devices.

Besides investigating intratriplet coupling, we also probed intertriplet exchange coupling in TIPS-tetracene. In the Thesis we presented published results of collaborative high field magneto photoluminescence (magneto-PL) measurements, performed in steady-state field up to 33 T (spectrally resolved) and in pulsed field up to 68 T (integrated and spectrally resolved). These experiments allowed to witness dips in magneto-PL due to intersystem crossing between spin states of different multiplicities: singlet-triplet and two singlet-quintet crossing resonances. Their positions in external magnetic field depends linearly on exchange coupling J energy specific for each triplet pair, which was then easy to extract. The ratio of $J - 3J/2 - 3J$ is fair for any pair, thus high field magneto-PL was useful to detect and distinguish triplet pairs of exchange coupling strength varying in a wide range.

Through providing the method by spectral resolution we could assign particular PL-spectra to these pairs. While intersystem crossing the pair doesn't contribute to integrated PL, thus raising spectral hole burning at certain magnetic fields. Therefore subtracting PL-spectra at these resonance dips from the integrated PL at neighbouring non-resonant field positions we set an approach to obtain a PL contribution of a certain exchange coupled triplet pair - selectively addressing exchange-coupled triplets.

We believe magneto-optic resolution of triplet pairs could be also performed in other materials for various applications.

Part II

Tunable coupling of quantum electrodynamics atom and oscillator

Chapter 8

Physics of 2-dimensional electron gas on liquid helium

8.1 Interest

2 dimensional electron system (2DES) is a system of electrons moving rather freely in two dimensions, but strictly confined in the third dimension. Depending on their densities they can form gas, liquid or solid, which will be discussed further in the Dissertation.

Electrons can be confined between different materials in silicon or gallium arsenide heterostructures. For example 2-dimensional electron gas is present in metal-oxide semiconductor field effect transistors (MOSFET, in inversion mode) and high-electron-mobility transistors (HEMT field-effect transistors based on the heterojunction between two semiconducting materials). Apart from that 2DEG can also be confined to surfaces - topological insulators remain of a certain interest and 2DEG plays key role in analysis and designing such systems. In the Dissertation we place 2DEG on the surface of liquid He^4, thus realising a strongly confined high purity system. Strong confinement can be also reached in mono-layer materials, like graphene, though helium allows to higher electron mobilities.

8.2 Wigner crystal

2D surface electrons (SE) on liquid helium allow to observe Wigner crystallisation experimentally due to the system being very clean: helium surface is pure and smooth and electron densities can be varied in wide range.

Wigner crystal is a strongly correlated phase of 2D electrons on the surface of liquid helium.

8.2.1 Low density crystallization

The first calculations of Eugene Wigner were performed for low density case [113], therefore let's discuss it first. According to an intuitional macroscopic logic low densities should mean weak interaction, meanwhile quantum mechanics approach clarifies the origins of this strong correlation. If we consider r_0 as a typical distance between electrons forming Wigner crystal, then we can get their kinetic ϵ_F (Fermi energy, related to the pulse) and potential E_p (defined by Coulomb interaction) energies:

$$r_s = \frac{r_0}{r_B}, \tag{8.1}$$

$$\epsilon_F \sim \frac{p^2}{2m} = \frac{(\hbar k_F)^2}{2m} \sim \frac{\hbar^2}{2mr_0^2}, \tag{8.2}$$

$$E_p \sim \frac{e^2}{4\pi\epsilon_0 r_0}, \tag{8.3}$$

$$\Rightarrow E_p > \epsilon_F, \tag{8.4}$$

where $r_B = \frac{4\pi\epsilon_0\hbar^2}{me^2}$ is the Bohr radius, $k_F = p/\hbar$ is the wavenumber, ϵ_0 is the electric constant. According to the first line of Eq.(8.1) in case of low densities (larger r_s) the kinetic energy ϵ_F is even lower than the potential energy E_p.

Thus one can say that electrons are "fixed" in their positions above the helium surface forming a kind of triangular crystalline lattice [114]. Therefore a steady electron puts local deforming pressure on the surface. Hence 2D crystal creates commensurate dimple lattice on the helium surface [115, 116], affecting transport properties of the system. In this case of low density the Fermi energy is significantly smaller than the temperature $\epsilon_F \ll k_B T$, so the electron gas becomes non-degenerate and the particles are described by classical physics. Then the main characteristic of the Wigner crystallisation - a plasma parameter, representing the Coulomb correlation energy to thermal energy ratio - is inversely proportional to the temperature:

$$\Gamma_c = \frac{e^2}{4\pi\epsilon_0 r_0 T} \tag{8.5}$$

8.2.2 High density crystallization

For 2D electronic systems similar phase transition was predicted to occur at rather high densities as well [117]. C.C. Grimes and G. Adams were first to prove the electron liquid to electron solid phase transition experimentally on the helium surface [118]. The main difference with the previous case is that for high electron densities Fermi energy is no longer much smaller than the temperature, but it becomes much larger: $\epsilon_F \gg k_B T$, so it

is degenerated regime. Then the plasma parameter is found as follows [119]:

$$\Gamma_c = \frac{e^2}{4\pi\epsilon_0}\frac{\sqrt{\pi n_s}}{k_B T} \geq 100 \tag{8.6}$$

Thus the plasma parameter increases with the density. Then we can estimate at what density n_s 2DEG will be non-degenerated:

$$\epsilon_F = \frac{\hbar^2}{m r_0^2} = \frac{\hbar^2 \pi n_s}{m} \ll k_B T, \tag{8.7}$$

$$n_s \ll \frac{k_B T m}{\hbar^2 \pi} \sim 10^{10}\mathrm{cm}^{-2}, \tag{8.8}$$

since in our experiments $T = 300$ mK, however such high densities cannot be achieved experimentally due to charge instabilities.

8.3 Stark effect

The Stark effect is the electric analogue to the Zeemann effect discussed in the Section 2.2 - it shifts and splits spectral lines of atoms and molecules due to the presence of an external electric field E_{ext}. The shift value $\Delta\epsilon$ may be linear (in a case of hydrogen atom in moderate fields) or quadratic.

Large atoms in the absence of field are pretty symmetrical and electrically balanced, which results in $< \mathbf{d} >= 0$. Therefore such an atom has no dipolar momentum in the absence of electric field, then when placed in static field th obtains an induced dipolar momentum. In the zero order and first orders of perturbation theory $\Delta\epsilon = 0$ and non-zero shift occurs only in the second order, yielding a quadratic dependence on the electric field strength E_{ext} - quadratic Stark effect.

However, for hydrogen-like atoms where electrons experience Coulomb potential, under applied electric field electron cloud surrounding the nucleus shifts against the field, while the nucleus shift in the direction of the field, though its' shift is rather small. This type of atoms has non-zero dipolar momentum $\mathbf{d}$ at zero field and once the field is applied they get potential energy of:

$$\epsilon_p = -\mathbf{d} \cdot \mathbf{E_{ext}} \tag{8.9}$$

and it is our case, because confined electrons on the helium surface create asymmetrical system, therefore their resonant transitions shift linearly with applied electric field.

8.4 Shubnikov-de Haas oscillations

Another beautiful phenomenon observable in 2DEG is Shubnikov-de Haas oscillations. It was first discovered by L.V. Shubnikov and V. de Haas as magnetoconductivity oscillations in Bismuth films at low temperatures [120]. Here we will shortly describe transverse Shubnikov-de Haas effect which is relevant for the case of 2DEG in degenerate regime ($\epsilon_F \gg k_B T$). 2DEG under perpendicular magnetic field applied experience Lorenz force prompting quantised circular in-plane motion - Landau oscillations [121], thus energy eigenstates are defined by Landau levels. Landau levels are equidistant:

$$\epsilon^L = (N_L + \frac{1}{2})\hbar\omega_C, \tag{8.10}$$

where ω_C is a cyclotron frequency and N_L is Landau level number, therefore they can be treated theoretically as a harmonic oscillator. Then energy levels can be manipulated by magnetic field strength B, since Landau oscillator's cyclotron frequency is defined as $\omega_C = eB/m_e$.

Electron gas DoS is a delta-function:

$$DoS(\epsilon) = \sum_{n=1}^{\infty} \delta\left(\epsilon - \hbar\omega_C\left(N_L - 1/2\right)\right) \tag{8.11}$$

As the distance between Landau levels increases with the magnetic field B Landau energy levels may cross Fermi level $\epsilon_n^L = E_F$ which leads to the 2DEG's conductivity gain. Meanwhile when Fermi level is in the area with no electrons - between two Landau levels $\epsilon_n^L < E_F < \epsilon_{n+1}^L$ - the conductivity is minimal. This process repeats with the magnetic field with a period $\tau_{osc} = 1/B_i - 1/B_{i-1}$. Then it can be used to find electron density:

$$n_e = \frac{2e}{h}\frac{1}{\tau_{osc}} \tag{8.12}$$

Nevertheless, Shubnikov-de Haas effect has also a topological aspect, reminding of Quantum Hall effect. If we consider a sample of finite macroscopic size, Landau levels then are bended at the edges as shown on figure 8.1, thus the conductivity appears to change not only with the magnetic field, but also with the coordinate.

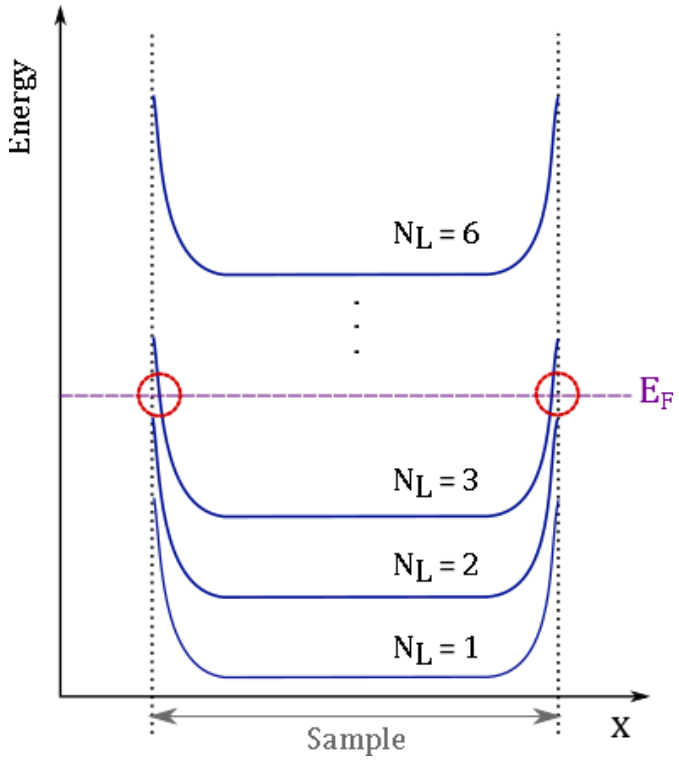

Figure 8.1: Landau levels of the 2 dimensional electron gas in a finite size sample. N_L is the level number, E_F is Fermi energy. Red circles mark crossings between Landau level and Fermi energy.

8.5 Microwave induced resistance oscillations

Microwave-induced oscillations of magnetoresistivity (MIRO) leading to the zero-resistance states (ZRS) attract a lot of attention recently. They were first predicted theoretically by Ryzhii V.I. *et al.* [122, 123, 124, 125] and first observed by Zudov M.A. *et al.* [126], who called this effect "Shubnikov-de Haas-like oscillations" (Fig. 8.2a), although MIRO is observed in the absence of degeneracy ($\epsilon_F \ll k_B T$), when Shubnikov-de Haas oscillations are not present.

They studied millimeterwave photoconductivity of 2DEG in GaAs$-$Al$_x$Ga$_{1-x}$As and observed it to oscillate with giant amplitude, resembling Shubnikov-de Haas conductivity oscillations. However the period measured appear to correspond to ω/ω_C ratio (see Chapter 10). So Zudov M.A. *et al.* explained these oscillations by resonant transitions between non-adjacent Landau levels, shown on Fig. 8.2b,c.

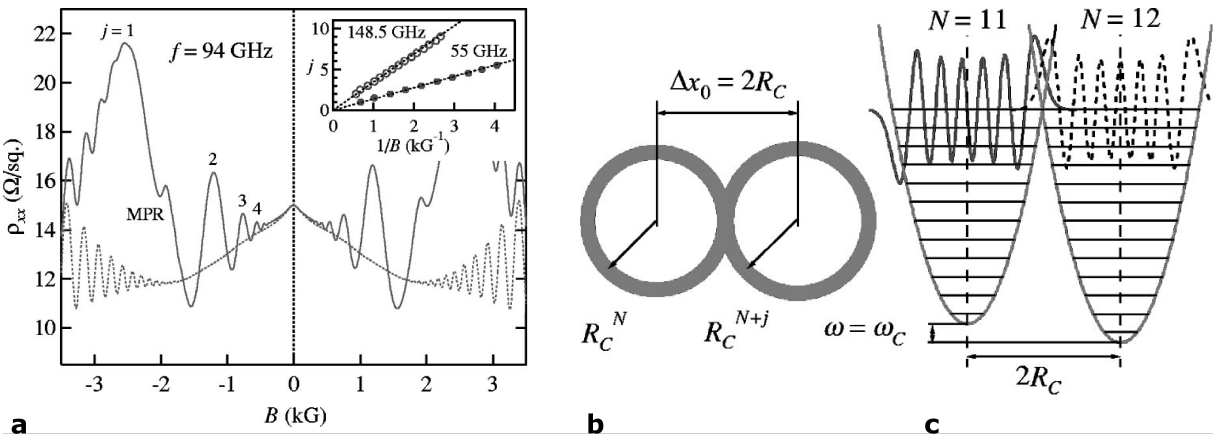

Figure 8.2: **a**, Magnetoresistivity measured by Zudov M.A. *et al.* under 94 GHz illumination (solid line) and dark (dotted line) depending on multiplicity index j. **Inset**: j evolution with $1/B$ at different illumination frequencies revealing an effective mass of an electron $m_e{}^* \approx 0.068 m_e$. **b**, A sketch of N^{th} and $(N + j^{th}$ Landau levels electron orbits with the maximum overlap expected at $\Delta x_0 \approx 2R^N{}_C$ **c**, Schematic representation for transition between orbits with different Landau levels number N, which corresponds to $j = 1$ peak observed by Zudov in photoconductivity. They explained oscillations to arise in magnetic field from Landau levels coincidence being close to the Fermi energy in two oscillators. The illustrations are taken from [126]

Thus obtaining the periodicity in field B:

$$\hbar\omega = j\frac{\hbar eB}{m*_e} = j\hbar\omega_C, \qquad j = 1, 2, .. \tag{8.13}$$

where j represents the difference between participating Landau levels indices. Thus MIRO can be a tool to spectroscopically probe Landau levels.

MIRO mechanisms

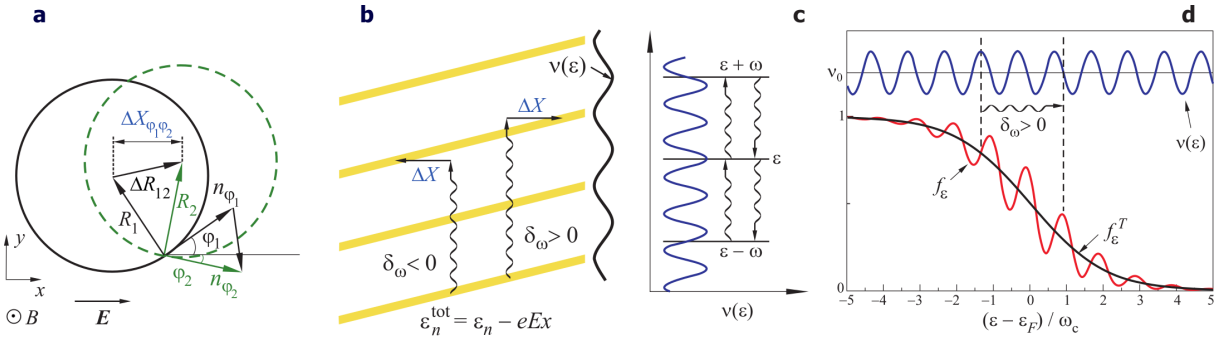

Figure 8.3: ***Mechanism 1:*** **a**, An illustration of a quasielastic scattering off disorder shifting a cyclotron orbit's centre. **b**, Schematic representation of the detuning $\delta_\omega = \omega/\omega_C - 2$ for the CR second harmonic sign determination by a direction of the cyclotron-orbit shift ΔX due to photon absorption. Yellow stripes represent the DoS maxima $\epsilon_n = (n + 1/2)\omega_C$ when Landau levels are tilted by a DC field. ***Mechanism 2:*** **c**, An illustrative sketch for the detuning $\delta_\omega = \omega/\omega_C - 2 = 1/4$ photon absorption and emission processes. **d**, The DoS $\nu(\epsilon)$ and schematic behaviour of distribution function f_ϵ for $k_BT \sim \omega_C$ compared to the thermal distribution f_ϵ^T. The illustrations are taken from [127]

Initially MIRO were explained via spatial displacements of quasiclassical electron orbits due to radiation-assisted scattering off disorder - so-called displacement mechanism [128, 129]. It considers these displacements' favourable directions (regarding to the anisotropic DC field) with period of ω/ω_C due to Landau quantisation leading to periodic modulation of the DoS of a form $\nu(\epsilon) \approx \nu(\epsilon + \omega_C)$ (Fig. 8.2, 8.3a,b). Then Dmitriev *et al.* [130] suggested inelastic mechanism to play main role in MIRO. According to them oscillations appeared due to radiation-induced changes in the electron states' population [130, 131]. For this mechanism detunings from the N^{th} harmonics of the cyclotron resonance (CR) $\delta\omega = \omega/\omega_C - N$ affect directly population of the states above or below the DoS $\nu(\epsilon)$ maxima giving positive or negative nonequilibrium correction to a distribution function depending on the detuning sign (Fig. 8.3 b) [127]. Figure 8.3d shows correlation of the DoS $\nu(\epsilon)$ and distribution function $f(\epsilon)$ oscillations around ν_0 and Fermi distribution $f_T(\epsilon)$), which affects photoconductivity (see the references for details). Further Dmitriev *et al.* confirmed contributions of the both proposed mechanisms. They found the inelastic mechanism to dominate at lower temperatures [132]. The displacement mechanism was found to play role at higher temperatures in cases of: (i) systems with rather high short-range impurity densities [133, 134], (ii) high MW power [135], (iii) strong DC field [134].

Recently MIRO is still of a great interest, it's different features are being studied on 2DES in various materials [136, 137]: oscillation amplitude dependence on titled magnetic field [138], photoconductivity response on MW polarisation [139], on MW power [140] etc.

8.6 QED systems

Being a part of quantum theory, quantum electrodynamics (QED) focuses on the electromagnetic interactions of quantum objects. And no doubt the coupling of such a fundamental objects like an atom and a resonant cavity is of a great interest for studying. Taken separately an atom possesses progressing energy levels structure with each next level locating closer to its' predecessor, whereas a cavity is a certain kind of a harmonic oscillator with all the levels located equidistantly. On the top of that ground an first excited atomic states (two-levels system) can play a role of a qubit, attracting even more interest to this topic. If an atom forms a qubit, then the cavity can could be used for a quantum memory or to connect several qubits.

Then the question is what is the effect of their coupling - how does the cavity affect the atom's energy levels diagram? Various systems were performed in order to answer this.

Several domains exist depending on the approach to states preparation and reconstruction. Cavity quantum electrodynamics (CQED), for example, uses atoms and high Q-factor cavities. To the contrary Circuit QED uses Josephson junctions as an atom and LC-circuit as an oscillator.

8.6.1 Jaynes-Cummings model

In 1963 Edwin Jaynes and Fred Cummings published a theoretical work proposing a model for making connection between the quantum theory of radiation and the semiclassical theory [141]. The model considers a single two-states atom (two-levels system) interaction with a single near-resonant cavity mode of quantized field. Here we will shortly discuss this theoretical method.

Field

Starting with Maxwell equations, Jaynes and Cummings performed quantization of the electromagnetic field of the cavity, and then got the electric and magnetic fields representation through creation and annihilation operators, where z - is the cavity's principal axis and x and y represent fields polarization:

$$\hat{E}_x(z,t) = E_0(\hat{a}(t) + \hat{a}^+(t))sin(kz) \quad , \tag{8.14}$$

$$\hat{B}_y(z,t) = E_0(\hat{a}(t) - \hat{a}^+(t))cos(kz) \tag{8.15}$$

Then they rewrote the field Hamiltonian as:

$$\hat{H}_{field} = \hbar\omega_{cav}(\hat{a}(t)\hat{a}^{+}(t) + \frac{1}{2}) \approx \hbar\omega_{cav}\hat{a}(t)\hat{a}^{+}(t) = \hbar\omega_{cav}\hat{a}^{+}\hat{a} \tag{8.16}$$

Atom

Ground and excited atomic states can be taken as:

$$|g\rangle = \begin{pmatrix} 0 \\ 1 \end{pmatrix}, \quad |e\rangle = \begin{pmatrix} 1 \\ 0 \end{pmatrix} \tag{8.17}$$

Then the Hamiltonian for two-levels system can be derived as:

$$\begin{gathered} \hat{H}_{atom} = E_g|g\rangle\langle g| + E_e|e\rangle\langle e| = \begin{pmatrix} E_e & 0 \\ 0 & E_g \end{pmatrix} = \\ = \tfrac{1}{2}\begin{pmatrix} E_g + E_e & 0 \\ 0 & E_g + E_e \end{pmatrix} + \tfrac{1}{2}\begin{pmatrix} E_e - E_g & 0 \\ 0 & -E_e + E_g \end{pmatrix} = \\ = \tfrac{1}{2}(E_g + E_e)\hat{\mathcal{I}} + \tfrac{1}{2}(E_e - E_g)\sigma_z \\ \hbar\omega_{atom} = E_e - E_g \\ \hat{H}_{atom} = \tfrac{1}{2}\hbar\omega_{atom}\hat{\sigma}_z \end{gathered} \tag{8.18}$$

Interaction

The formula for the dipole momentum of the atom interaction with the electromagnetic field is common:

$$\hat{H}_{int} = -\hat{d}\hat{\mathbf{E}} \tag{8.19}$$

Using Eq. 8.14, this Hamiltonian can be written as:

$$\hat{H}_{int} = -\hat{d} \cdot E_0(a + a^{+})sin(kz)\mathbf{x} = \lambda\hat{d}(a + a^{+}) \quad , \tag{8.20}$$

$$\lambda = -\sqrt{\frac{\hbar\omega_{cav}}{\epsilon_0 V}}sin(kz) \tag{8.21}$$

Then after some conversions interaction term can be transformed as:

$$\hat{H}_{int} = \hbar\Omega(\hat{\sigma}_{+} + \hat{\sigma}_{-})(\hat{a} + \hat{a}^{+}) \quad , \tag{8.22}$$

$$\Omega = -\frac{d}{\hbar}\sqrt{\frac{\hbar\omega_{cav}}{\epsilon_0 V}}\sin kz \tag{8.23}$$

Considering $\hat{a}$, $\hat{a}^{+}$ and $\hat{\sigma}_{\pm}$ operators evolution with time, the Hamiltonian becomes:

$$\hat{H}_{int} = \hbar\Omega(\hat{\sigma}_+\hat{a}e^{i(\omega_{atom}-\omega_{cav})t} + \hat{\sigma}_+\hat{a}^+e^{i(\omega_{atom}+\omega_{cav})t} + \tag{8.24}$$

$$+\hat{\sigma}_-\hat{a}e^{-i(\omega_{atom}+\omega_{cav})t} + \hat{\sigma}_-\hat{a}^+e^{-i(\omega_{atom}-\omega_{cav})t}) \tag{8.25}$$

To simplify it, rotating wave approximation is used. Its' main idea is that oscillations of $\hat{\sigma}_+\hat{a}^+$ and $\hat{\sigma}_-\hat{a}$ term are too fast, thus they give 0 in average. Then the interaction term is:

$$\hat{H}_{int} = \hbar\Omega(\hat{\sigma}_+\hat{a} + \hat{\sigma}_-\hat{a}^+) \tag{8.26}$$

And finally the Jaynes-Cummings Hamiltonian is [141, 142]:

$$\hat{H}_{JC} = \hbar\omega_{cav}\hat{a}^+\hat{a} + \frac{1}{2}\hbar\omega_{atom}\hat{\sigma}_z + \hbar\Omega(\hat{\sigma}_+\hat{a} + \hat{\sigma}_-\hat{a}^+) \tag{8.27}$$

8.6.2 CQED approach

For the most evident experimental realisation - CQED - of such coupling one needs to be able to manipulate a single particle and to maintain stable oscillations.

In CQED, an atom's electric dipole moment d interacts with the vacuum state electric field E_0 of a cavity inducing Rabi vacuum oscillations at the frequency $n_{Rabi} = 2dE_0/h$.

In 1996 two papers appeared at the same issue of Physical Review Letters reporting experimental results on the same topic, though obtained by two opposite approaches [143, 144]: so-called "in-vivo" studies of a single particle (an atom/ion) coupling to an oscillator. Interesting that in the first report [143] the measurements were performed with trapped single charged atoms (ions) (team of David Wineland, NIST, Boulder), whereas in the second [144, 145] the authors trapped a photon (team of Serge Haroche, ENS, Paris). These two works got Nobel Prize in 2012.

David Wineland

Inspired by Ignacio Cirac and Peter Zoller's qubit preparation scheme [146] David Wineland's group placed $^9Be^+$ ion in strong confinement coaxial-resonator-driven rf (Paul) trap [147] and cooled it to near the zero-point energy using resolved-sideband laser cooling with stimulated Raman transitions [148, 149, 150] (Fig. 8.4). Once the ion is cooled to the ground Fock state, they applied a sequence of Rabi π pulses of laser radiation (for details see the References [143, 149]). Thus they fixed "the atom" and made photons pass through the rf trap and the oscillator is due to the ion motion.

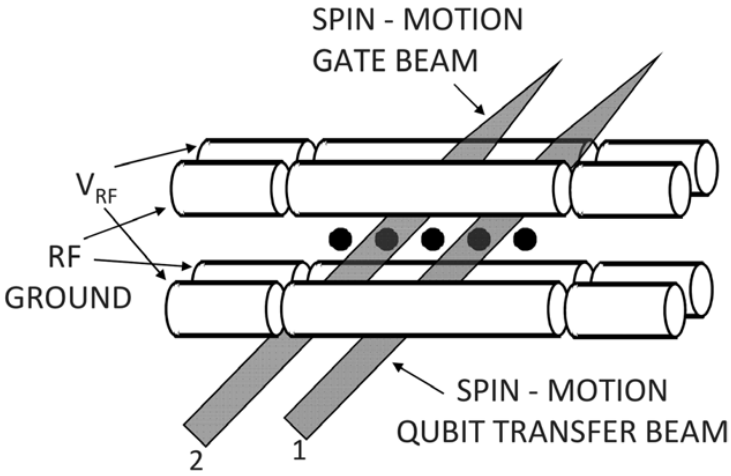

Figure 8.4: Cirac and Zoller scheme [146]. Radio frequency (RF) potential is to rise a ponderomotive pseudopotential, static potential is to confine ions along the trap axis. Illustration from Ref. [150]

It can be explained as follows: Wineland's team considered a trapped ion with a single-electron electric-dipole transition of frequency ω_0 and radiative linewidth γ (confining the ion by 1D harmonic well of vibration frequency $\omega_v \gg \gamma$). Then if exciting the transition by laser radiation of frequency ω_L applied along the ion's motion direction (z-axis), absorption spectrum would reveal main frequency ω_0 and modulation sidebands spaced by ω_v due to Doppler effect. Tuning the laser to the lower ("red") sideband is used for cooling the ion: $\omega_L = \omega_0 - \omega_v$. Then Rabi oscillations arise, since the ion absorbs photons of energy $\hbar(\omega_0 - \omega_v)$ and emits photons with energies of $\sim \hbar\omega_0$, that returns the ion to its' initial internal state, thus reducing the ion's kinetic energy by $\hbar\omega_v$ per scattering event (assuming $\hbar\omega_v$ is much greater than the photon recoil energy). Such cooling goes till the limit of the ion's average vibrational quantum number in the harmonic well is given by $\langle n \rangle_{min} \simeq (\gamma/2\omega_v)^2 \ll 1$ [149].

The interaction of the ion with photons is given by the following Hamiltonian:

$$\hat{H}_i = -e\vec{r} \cdot \hat{\epsilon} E_0 cos(kz - \omega_{\mathbf{L}} t + \phi) = \hbar\mathbf{\Omega}(\sigma_+ + \sigma_-)(e^{i(kz-\omega_L t+\phi)} + e^{-i(kz-\omega_L t+\phi)}) \quad , \tag{8.28}$$

$$\mathbf{\Omega} = -E_0 \langle \uparrow | \vec{r} \cdot \hat{\epsilon} | \downarrow \rangle \quad , \tag{8.29}$$

where $\vec{r}$ represents electron coordinate relative to the ion's core, z is the ions mean position, $\hat{\epsilon}$ is the laser beam's polarization of amplitude E_0, k stands for a wave vector and ϕ is the electric-field phase at the mean position of the ion. Then taking $\eta = kz_0$ Lamb-Dicke parameter and some conversions Wineland *et al.* simplify the red- and blue-sidebands terms to:

$$\hat{H}_{iR} = \hbar\eta(\Omega\sigma_+ a + \Omega^*\sigma_- a^+) \quad , \tag{8.30}$$

$$\hat{H}_{iB} = \hbar\eta(\Omega\sigma_+ a^+ + \Omega^*\sigma_- a) \quad , \tag{8.31}$$

$$\tag{8.32}$$

for $\omega_L = \omega_0 \mp \omega_z$ respectively, where a and a^+ are lowering and raising operators for the ion motion, whereas σ_+ and σ_- are internal-state raising and lowering operators. Thus they performed Fock states to manipulate the ion's motional states [150, 149].

Serge Haroche

Serge Haroche's group based their approach on Rydberg atom maser experiment of Gross *et al.* [151], where atoms excited to Rydberg states by laser illumination were rising pulsing emission in the MW field. One of the main ideas was to perform *in vivo* measurements in sense of keeping the same photon. For that purpose they used a photon box to trap a photon instead of trapping an atom.

Rydberg atom is an atom with at least one electron excited to very high quantum number n level (determined by Rydberg formula), thus ionic core and such excited electron perform a huge effective hydrogen-like atom [152, 153]. By wave-particle duality a stable orbit's circumference fits an integer number of wavelengths corresponding to an electron.

Haroche *et al.* prepared rubidium atoms in circular Rydberg state with laser and RF excitation [154]. In such configuration the outer electron orbits are round with a diameter $\sim 10^3$ of a ground state atom. Ground Rydberg $|g\rangle$ state's principal quantum number was 50 and the excited $|e\rangle$ state's was 51, therefore allowing to longer lifetimes $\sim$ 30 ms due to larger angular momentum (the same order of magnitude as a lifetime of the photon in the cavity). A Rydberg atom in it's ground $n = 50$ or excited $n = 51$ state is shown on figure 8.5a. Then they applied a pulse of resonant MW to prepare the atom in a superposition state between $|g\rangle$ and $|e\rangle$ states, which then performs an electric dipole due to an interference of de Broglie waves of two states as shown on figure 8.5b. This dipole then rotates with 51 GHz frequency and is sensitive to MW radiation and can be imagined as a "clock".

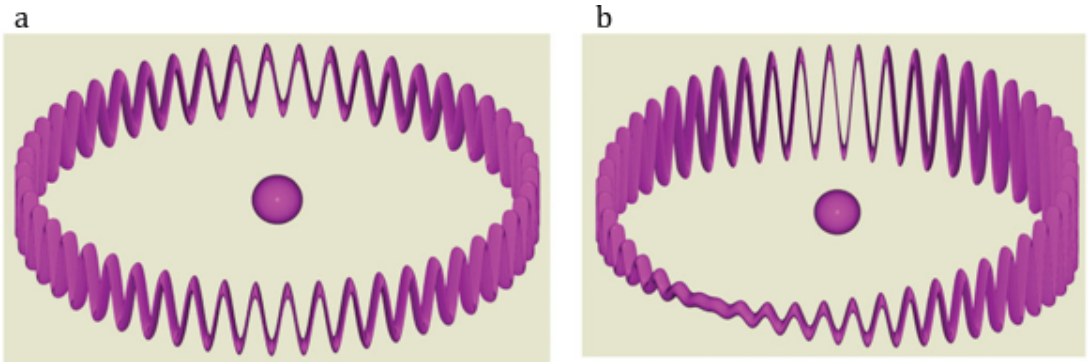

Figure 8.5: Schematic representation of a Rydberg atom. **a**, in its' ground $|g\rangle$ or $|e\rangle$ state atom remains symmetrical with de Broglie wave's amplitude being uniform allover the circumference. **b**, in superposition of ground $|g\rangle$ or $|e\rangle$ states de Broglie waves corresponding to these states interfere positively and negatively on the opposite sides of the electron orbit, inducing an in-plane rotating electric dipole. Illustrations from Ref. [145].

Non-resonant photon cannot be absorbed by such an atom, thus *in vivo* criteria was satisfied, meanwhile by affecting the atomic energy levels the photon changes the dipole rotation frequency [155], which is proportional to the photon number, yielding a phase shift. So Haroche's team built an interferometer to detect it (Fig. 8.6), where atoms were prepared in 0, driven into the superposition in R_1 by a MW flash, exposed to the trapped photon in the cavity C, and the atomic dipole orientation was detected in R_2 by the second MW flash [144, 145].

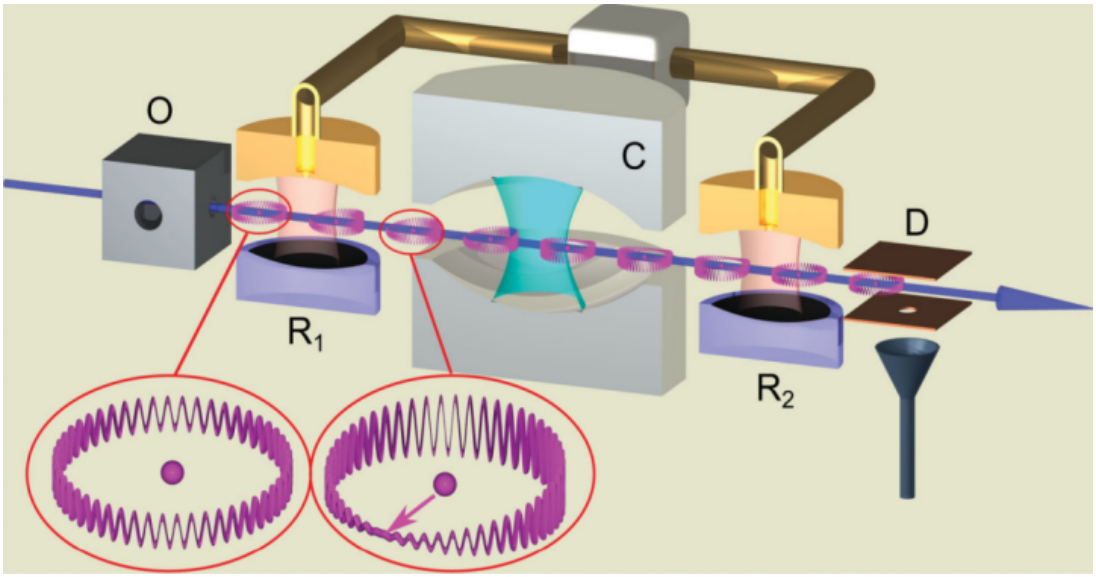

Figure 8.6: Serge Haroche's team setup - the cavity QED Ramsey interferometer.

Two team obtained similar results shown on figure 8.7: panel (a) reveals ion oscillations in a superposition of vibration quanta in rf trap, panel (b) represents similar signature of resonant interaction of atoms with an oscillating field with superposition of photon numbers [143, 144, 145].

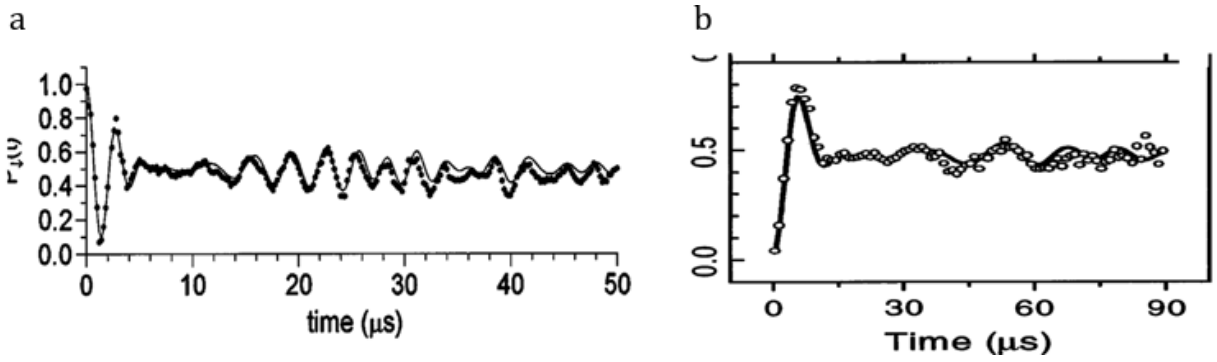

Figure 8.7: Rabi oscillations in the (a) NIST and the (b) ENS experiments [143, 144, 145]. Vertical axis is a transition probability between two states, which is time-dependent.

8.6.3 Circuit approach

As an example of another very different way to perform an interacting system of an atom with electro-magnetic field we review briefly a realization of circuit QED.

Various materials and systems were considered to perform better artificial atoms and cavities by creating larger dipole moment atom size and vacuum field strength. For an illustration we will focus here on the first reported experimental observation of strong coupling of an artificial atom with a photon, performed by Andreas Wallraff *et al.* [156].

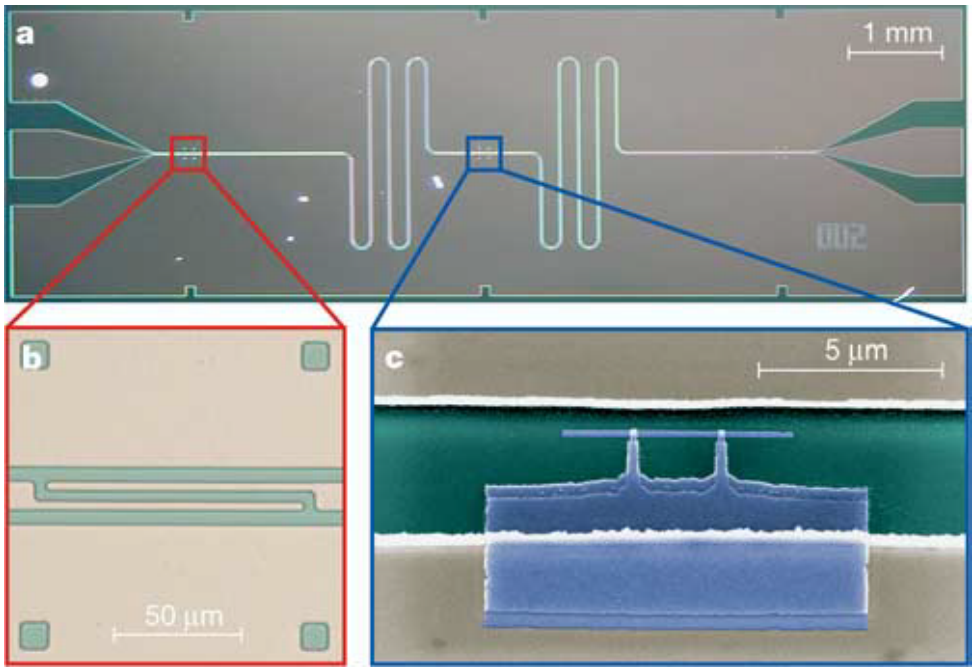

Figure 8.8: Circuit QED, fabricated by optical lithography. **a**, integrated circuit itself. **b**, capacitive coupling to the input and output lines. **c** the Cooper pair box highlighted with blue placed between the center conductor on the top and the ground plane of a resonator on the bottom. Figure taken from Ref. [156].

They fabricated the circuit by depositing thin superconductor film on a silicon chip

with a certain pattern by means of optical lithography (Fig. 8.8a). The harmonic oscillator in the circuit is a coplanar waveguide resonator of frequency $\omega_r = 1/\sqrt{LC}$, which is coupled to transmission lines by capacitors shown on figure 8.8b. It is described by the typical Hamiltonian:

$$\hat{H}_r = \hbar\omega_r(a^+a + 1/2) \tag{8.33}$$

This scheme allowed Wallraff'm team to reach an average photon lifetime in their resonator $\gtrsim$ 100 ns. An artificial atom is represented by a so-called Cooper pair box (CPB): superconductiong island coupled to a large superconducting reservoir via two Josephson junctions (Fig. 8.8c), described by the following Hamiltonian:

$$\hat{H}_a = -(E_{el}\sigma_x + E_J\sigma_z)/2 \quad , \tag{8.34}$$

where E_{el} and E_J are electrostatic and Josephson energies respectively, whose scales are defined during fabrication and then the values can be controlled by applied voltage and magnetic flux.

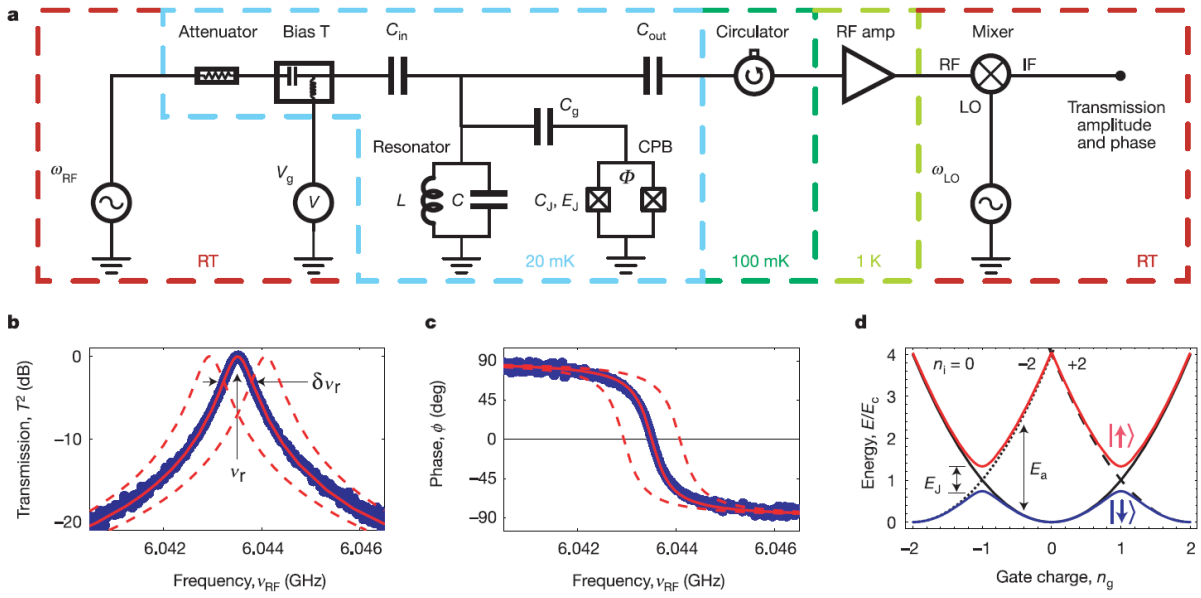

Figure 8.9: Wallraff *et al.* measurements. **a**, scheme of the experimental circuit, the resonator and the Cooper pair box are coupled through the capacitance C_g. **b**, the resonator's transmission power spectrum fitted by a lorentzian. **c**, transmission phase measurements. **d**, the Cooper pair box energy levels with "atomic" ground and excited states' bands marked as $|\uparrow\rangle$ and $|\downarrow\rangle$.

As shown on the experimental circuit scheme (Fig. 8.9a), the Cooper pair box is coupled to the resonator via the capacitance C_g and then the Cooper pair energy changes due to vacuum voltage fluctuations V_{rms} in the resonator by:

$$\hbar g = dE_0 = eV_{rms}C_g/C_\Sigma \tag{8.35}$$

As expected, Wallraff *et al.*describe the whole system by the Jaynes-Cummings Hamiltonian:

$$\hat{H}_{JC} = \hat{H}_r + \hat{H}_a + \hbar g(a^+\sigma_- + a\sigma_+) \tag{8.36}$$

For more details see Ref. [156].

8.6.4 Hybrid system

Electrons confined on the helium surface can be implemented to such systems. For example Ge Yang *et al.* developed a hybrid device combining circuit QED with electrons trapped in the superfluid helium [157].

In their experiment stable electrons ensemble was trapped above an on-chip superconducting MW resonator, changing the capacity of the cavity, thus shifting its' resonant frequency: the superfluid helium induced an effective dielectric constant of the waveguide, which resulted in decreasing the resonator's frequency proportionally to the helium thickness. This shift they showed to be several times larger than the cavity linewidth and obtained the coupling strength per one electron of about 1 MHz.

Their device contained an integrated electron trap and coplanar waveguide resonator, where the ground planes were thicker than the centre, thus forming a microchannel of 800 nm height defining superfluid helium thickness (Fig. 8.10). Electrons were kept in the resonator by DC bias voltage and were confined in two in-plane directions of the microchannel. Measurements on the device were performed in transmission using a low-noise amplifier (LNA) and the trap potential is tuned through a DC source connected to the center pin through a low-pass filter. That DC voltage created a parabolic trapping potential for electrons above the surface that couple to the RF field in the cavity. For single electron experiments Ge Yang *et al.* provided additional smaller electron traps.

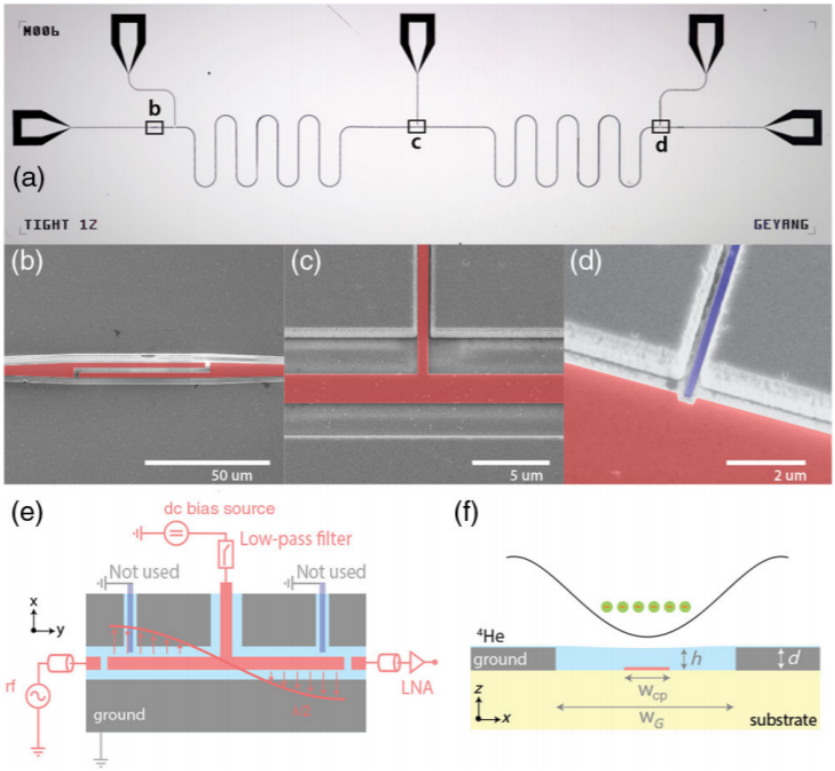

Figure 8.10: The hybrid device of Ge Yang *et al.* combining circuit QED with electrons trapped in the superfluid helium. **a**, a cavity-electron ensemble trap placed on superconducting chip. **b**, gap capacitors. **c**, bias electrode connected to the centre of the cavity at the standing-wave voltage distribution node. **d**, electron trap. **e**, circuit sketch with the voltage distribution. **f**, schematic view of the cavity waveguide gap. Figure taken from the Ref. [157]

In the Dissertation we present a different approach to the problem, using the same system - 2DEG - to perform both an artificial atom and an oscillator, which will be discussed thoroughly in the following chapters.

8.6.5 2DES coupling to a cavity

As discussed in previous sections, 2DES give possibilities to study various advanced physical phenomena and coupling effects are of certain interest as well. Last year Denis Konstantinov group reported their investigation on a related subject: they coupled cyclotron motion of the surface electrons to the microwave field [158]. For that they used electrons confined on the surface of liquid helium and induced cyclotron motion by applying perpendicular magnetic field. Coupling to the MW was done using semi-confocal Fabry-Perot resonator with the TEM_{002} mode's frequency $\omega_r \approx 35.06$ GHz (Fig. 8.11).

This technique allowed them to resolve the electrons' interaction with two polarization components of the field. They found that the interaction with these two components affecting differently the spectrum of the coupled field-particle motion (Fig. 8.12). Nor-

mal mode (CR-active, co-rotating component) splitting was observed when the cyclotron frequency ω_c was close to the cavity's resonant frequency ω_r. Another mode (CR-passive, counter-rotating component) yielded a resonant dip when the excitation frequency ω was close to ω_r. Therefore Konstantinov *et al.* associated these two modes as two circular polarized components of the MW field. In order to explain the results Konstantinov *et al.* derived both classical and quantum based theoretical models. Comparing them showed that the quantum approach's mean-value equations of motion yielded the same result, therefore the classical model was sufficient. Here we do not review these calculations, so for the details see Ref. [158]. Thus they experimentally reached strong coupling of the surface electrons system to the microwave field and presented a complete classical electrodynamics model explaining the phenomenon.

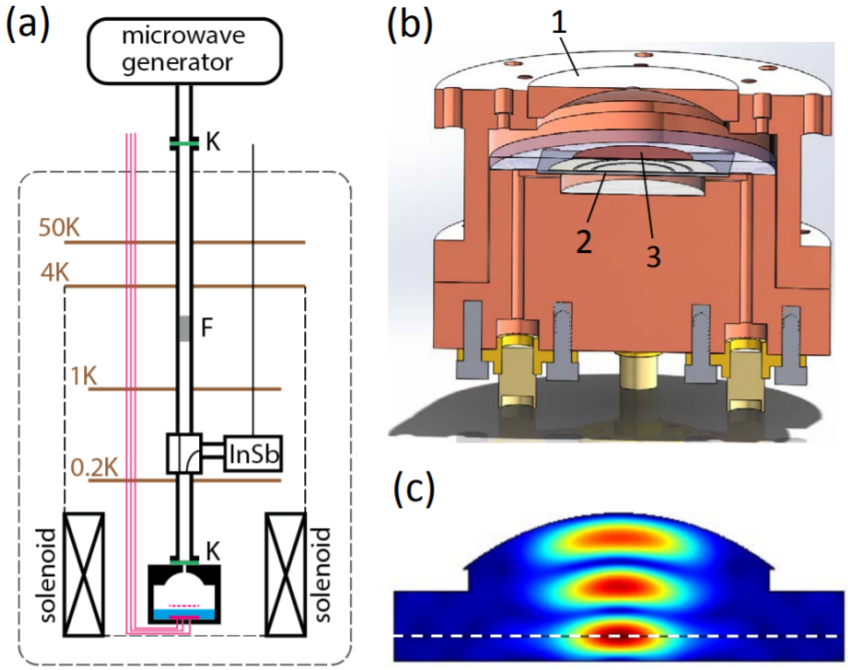

Figure 8.11: Schematic representation of Konstantinov group's experiment. **a**, the setup placed in the dilution refrigerator. **b**, experimental cell: ***1*** top spherical mirror, ***2*** bottom flat mirror and Corbino electrodes, ***3*** 2DES. **c**, resonant TEM_{002} mode distribution in the Fabry-Perot resonator. The dashed line marks liquid helium level and the position of the first antinode of the field. Figure taken from the Ref. [158]

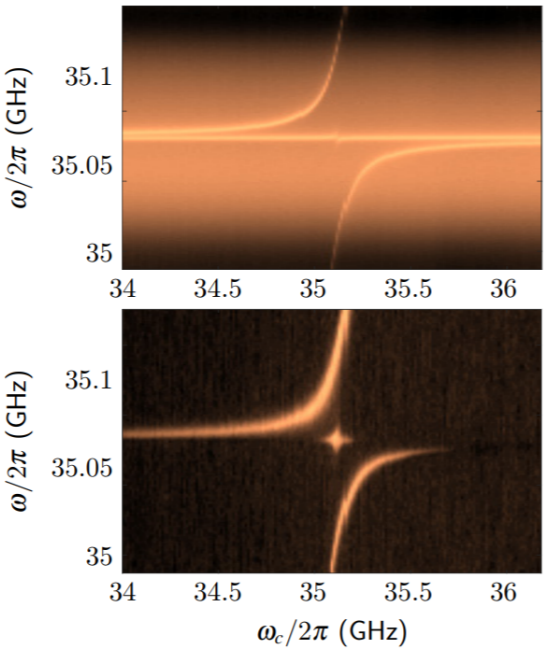

Figure 8.12: Results of Konstantinov group's experiment. **top**, 2D spectrum of the power reflection from the cavity depending on the cyclotron frequency of electrons ω_c and frequency of MW excitation ω measured at $T = 0.2$ K for electron surface density $n_s = 8.010^7 cm^2$ and input MW power $P = 9$ dBm. **bottom** electron DC conductivity response in the same conditions. Figure taken from the Ref. [158]

Chapter 9

Spectroscopy of confined electron gas

Our experimental setup consists of a cavity with Corbino electrodes (experimental cell, Fig. (9.1)), which was placed in a dilution refrigerator. This cavity is half-filled with liquid helium-4 by condensing helium vapor and monitoring the capacitance between top and bottom electrodes.

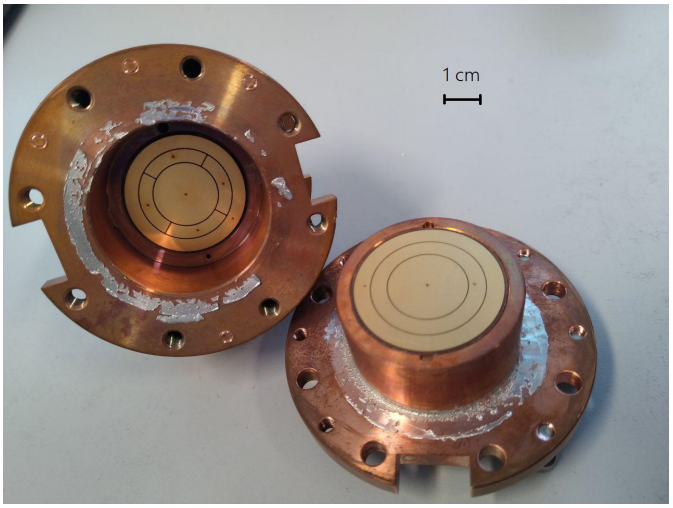

Figure 9.1: A photo of the experimental cell (disassembled) - a cavity with Corbino electrodes, the geometry of which is discussed later in the main text.

Electrons are then deposited by thermal emission from a heated tungsten filament and are trapped on the surface by a pressing electric field $E_\perp$ induced by the potential difference between top and bottom central electrodes of the cavity.

9.1 Densities

Depending on their density SE can form 2 dimensional crystal, liquid or gas (2DEG). Number of electrons n_e in the system can be controlled by initially depositing a high number of electrons and then lowering the confinement voltage allowing excess electrons

to escape the helium surface. This way n_e can be found by measuring their compressibility in the equilibrium [159].

In the saturation regime, electron density is given by formula:

$$n_e = \frac{E_\perp}{2\pi e} \sim 10^7 \mathrm{cm}^-2 \tag{9.1}$$

In our measurements the electron gas density was $n_e \simeq 1.5 \times 10^7$ cm^{-2} (with a total number of 4×10^7 electrons trapped in the cloud) at the temperatures $T_{exp} \sim 300$ mK to obtain 2DEG regime. To check that the Wigner crystal is not the phase we are working at, we can calculate crystallisation temperature for the chosen density and compare it to T_{exp}. Plasma parameter at the Wigner solid melting temperature is known to be $\Gamma_c \sim 130$, thus Wigner crystallisation temperature for our electron densities remains much lower than T_{exp} and is equal to ~ 70 mK.

9.2 Experimental cell configuration

Above mentioned experimental cell's (Fig. (9.1)) layout is presented on figure (9.2). It is formed by two plain electrodes - on the top and on the bottom, both divided into three parts. The cylindrical space of 2.6 mm height and $\sim$ 5 cm diameter was half-filled with liquid He^4, as mentioned above. Electrons were emitted by the filament ***7*** and then confined by the electric field: a positive DC voltage V_d applied to ***4*** and ***5***, controlling pressing electric field value $E_{perp} = V_d/h$. In order to keep electrons inside the cell one needs to apply negative voltage on the perimeter of the cell. Although one of main conditions for our experiments is the homogeneousness of the $E_\perp$. To solve this issue we applied a negative guard potential to the electrodes ***3*** and ***6***, but fixed the potential difference $V_6 - V_3$ to V_d. Centre top electrode ***1*** was grounded and used as a detector, AC voltage 10 mV of a frequency 1137 kHz was applied via segmented electrode ***2*** to obtain the admittance Y of the cell. Microwave (MW) power of atomic transition (a photon absorption lets an electron jump to a higher state above the helium surface, Fig. 9.3) frequency was applied via a waveguide. It was modulated with frequencies of $\sim 10Hz$ in order to get an effect of MW power on/off to filter out the signal under no MW applied. Perpendicular and parallel magnetic fields were applied by two vector magnets surrounding the cell.

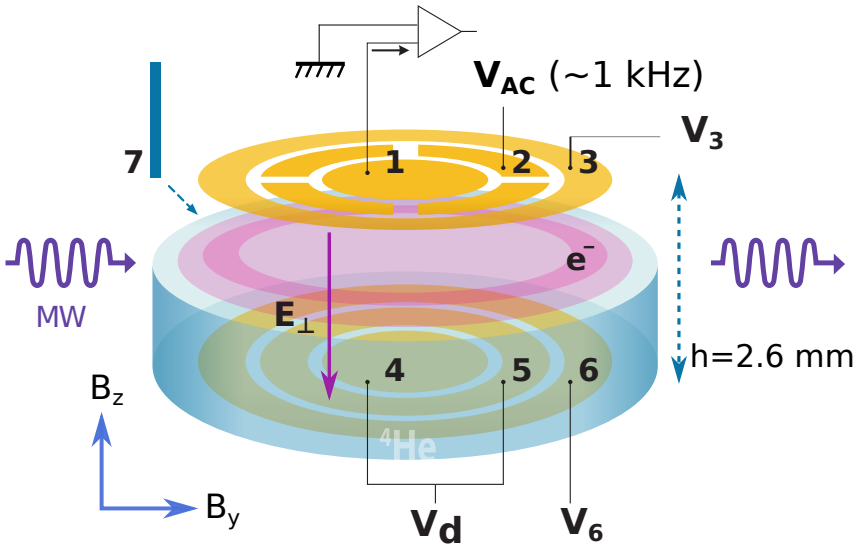

Figure 9.2: Schematic diagram of the experimental cell. The top electrodes ***1*** and ***2*** are DC grounded and are used for the AC measurements. A positive DC voltage V_d is applied to ***4*** and ***5*** confining the electrons into the center of the cell and fixing $E_\perp = V_d/h$. The electrodes ***3*** and ***6*** are used as a guard with negative potential. To ensure an homogeneous $E_\perp$ we fixed $V_6 - V_3$ to V_d (and $V_d - V_6 = 6\text{V}$). The admittance Y of the cell is obtained by applying a 10 mV AC voltage at 1137 Hz to the segmented electrode ***2*** and measuring the induced pickup voltage on ***1*** with a lock-in amplifier. It depends on the in-plane conductivity of the electrons under magnetic field as obtained from Corbino measurements with Ohmic contacts on conventional 2DES. MW power was sent into the cell through a waveguide and ***7*** is the filament (e^- source).

Due to experimental scheme features one cannot know the distribution of magnetic and electric components of the MW applied inside of the cell, thus in such configuration pulsed experiments would be impossible, however this doesn't play any role for our measurement.

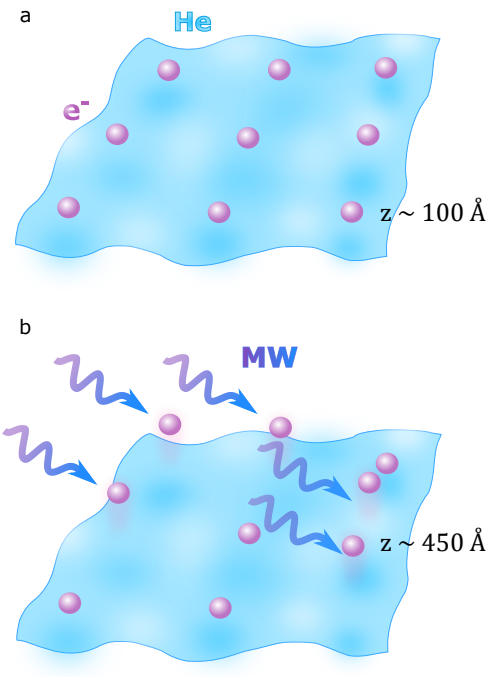

Figure 9.3: Electrons hovering on the surface of liquid helium-4 [160]. **a**, the lowest surface state is ~ 100 $\mathring{A}$ distant from the surface. **b**, absorbing a MW photon a surface electron can go to the excited state which is ~ 450 $\mathring{A}$ from the surface.

9.3 Admittance measurements

2DEG for in plane transport behaves as an effective resistance R placed between two contacts with capacitance C (Fig. 9.4). This resistance can then be determined by measuring the admittance of the cell Y between the two inner Corbino contacts from the top electrodes at frequencies comparable with the RC relaxation time (we used 1137 Hz). To extract the MW dependent (MIRO) admittance δY, MW power is modulated at a frequency of 17 Hz and a double demodulation technique is used. Real and imaginary parts of δY give very similar lineshapes.

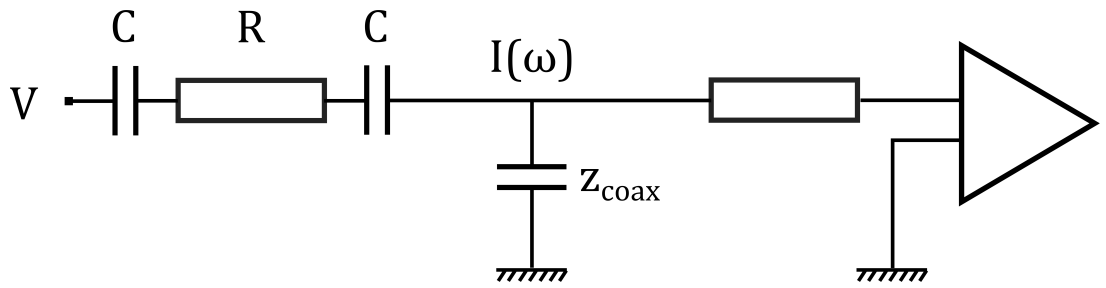

Figure 9.4: 2DEG on the liquid helium placed between Corbino electrodes can be illustrated as a capacitance-resistance sandwich (left). The current through the circuit is then sent to voltage amplifier (right) and then the voltage drop on the amplifier is measured. It depends on the R, C and input voltage V, and also on the impedance of the coaxial cable z_{coax}.

The admittance Y can be obtained through the current $I(\omega)$ measurements (Fig. 9.4, 9.2). We measure it as voltage drop on the voltage amplifier (right on Fig. 9.4). When the frequency $\omega = 0$ RCR-cell acts like a capacitance and when $\omega \gg 1/RC$ the cell acts like a low-pass filter (see equations 9.2). Since there is large resistance at the input of the amplifier and also coaxial cables impedance $z_{coax} = 1/iC_{coax}\omega$, the amount of input current on the amplifier depends on these resistance-impedance ratio, whereas the impedance z_{coax} depends on the frequency ω.

So first we calculate the current as follows:

$$z_C = \frac{1}{iC\omega} \tag{9.2}$$

$$z_R = R \tag{9.3}$$

$$z = z_C + z_R + z_C = R + \frac{2}{iC\omega} = \frac{iC\omega R + 2}{iC\omega} \tag{9.4}$$

$$I(\omega) = \frac{V}{z} = V\frac{iC\omega}{2 + iC\omega R} = VC\omega\frac{2i + RC\omega}{4 + (C\omega R)^2} \tag{9.5}$$

Then the measured voltage V_{mes} can be found as:

$$z_{coax} = \frac{1}{iC_{coax}\omega} \quad , \tag{9.6}$$

$$V_{mes} = z_{coax} \cdot I(\omega) = -\frac{iVC}{C_{coax}} \cdot \frac{2i + RC\omega}{4 + (C\omega R)^2} = \tag{9.7}$$

$$= \frac{VC}{C_{coax}} \cdot \frac{2 - iC\omega}{4 + (C\omega R)^2} \tag{9.8}$$

From this we can get different phase signals V_x and V_y:

$$V_x = \frac{VC}{C_{coax}} \cdot \frac{2}{4 + (C\omega R)^2} \quad , \tag{9.9}$$

$$V_y = -\frac{VC}{C_{coax}} \cdot \frac{C\omega}{4 + (C\omega R)^2} \tag{9.10}$$

Then these in-phase V_x and out-of-phase V_y signals amplitude depends on the ω and looks as it is plotted on figure 9.5, where an arrow shows the direction of ω increasing.

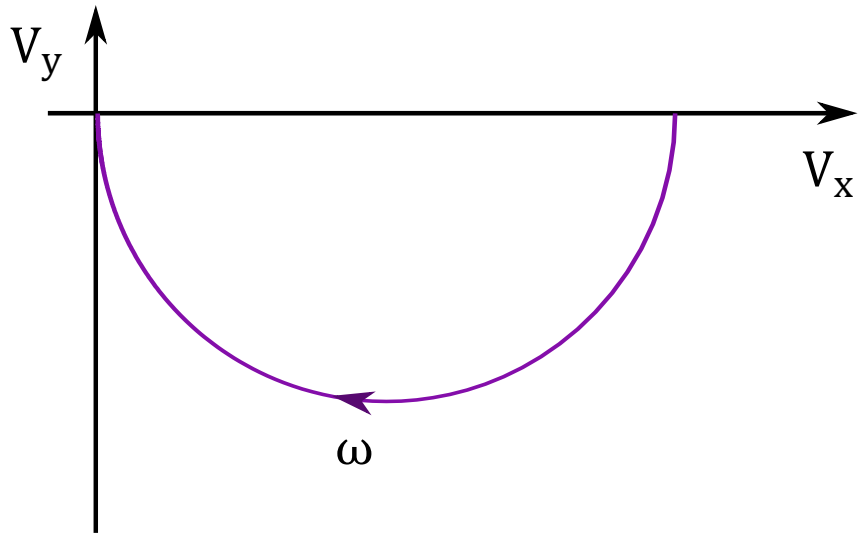

Figure 9.5: Voltage in-phase and out-of-phase signal diagram. An arrow indicates the ω increase.

Thus knowing the position on this diagram (Fig. 9.5) and the capacitance $C = \epsilon_0 \frac{2\pi r^2}{h} \approx 0.25$ pF we estimated the R resistance of the electron gas. In presence of perpendicular magnetic field in the $0.5 - 1$ Tesla range, $RC\omega \sim 1$, occurs at $\omega \approx 2\pi \cdot 300$ Hz, which corresponds to a typical resistance per square of the electron gas of hundreds of MOhm (at zero magnetic field the resistance is much lower of the order of tens of kOhms). Thus our approach is rather simplified in contrast to commonly used finite elements calculations. However finite elements approach works in absence of resonances, for example, when one deals with edge magnetoplasmons, meanwhile our goal was to detect the difference between resonant and non-resonant conditions and our method describes the experiment well. Although one can still perform finite elements calculations if needed. Excitation frequency was chosen to be ~ 1 kHz to be around the lowest point of the arc shown on Fig. 9.5, besides it had to be > 100 Hz to reduce the pink noise of the amplifier, which increases with $1/f$. MW modulation to perform MW on/off effect was chosen ~ 10 Hz since it had to be $\ll f \sim 1$ kHz to demodulate the signal. At the same time it had to be low enough to detect the conductivity response (which is of order ~ 100 ms).

Figure 9.6: A photography of the sampleholder with the assembled cell, which was then placed in a dilution refrigerator.

The whole system (Fig. 9.6) was placed in a dilution fridge and kept at T $\sim$ 300 mK. Magnetic field was applied to the 2DEG in the cell using two vector magnets - perpendicular and in-plane oriented - with magnetic field being swept up to $\sim$ 1.3 Tesla.

Chapter 10

QED Hamiltonian for 2DEG

For better understanding, in this Chapter we describe the derivation of the QED Hamiltonian for electrons on helium, performed by Alexei Chepelianskii with the participation of the author. It will be used to explain and describe our experimental results in the following Chapter 11.

10.1 Vertical motion

2DEG creates an electric field, which then polarizes the liquid helium, thus creating an image charge. This positive image charge attracts the electrons, pressing them towards the helium surface, however electrons cannot penetrate inside the liquid helium, due to a steep electron-volt high energy barrier. The interaction with the image charge gives rise to a one-dimensional Coulomb potential which leads to the quantization of the vertical motion and to the formation of a Rydberg series of bound states for a one-dimensional hydrogen-like atom. This series will play the role of the atomic degree of freedom in our QED model, which we will call "an atom" further in the text. A pressing perpendicular static electric field $E_\perp$ present in the experiments allows to shift the Rydberg levels through linear Stark effect [161]. Then the spectroscopic positions of the Rydberg states is well described by a one-dimensional Schrödinger equation for vertical motion:

$$\mathcal{H}_a = -\frac{\hbar^2}{2m}\frac{\partial^2}{\partial z^2} + V_a(z) = \sum_n \varepsilon_n \left|n\right\rangle \left\langle n\right| \tag{10.1}$$

where we introduced z - the vertical distance of the electrons to the helium surface, the eigenstates for the vertical motion $|n\rangle$ and their eigenenergies ϵ_n. Above the helium surface, for $z > 0$, the confinement potential $V_a(z)$ is the sum of the interaction with the image charge and with the perpendicular electric field:

$$V_a^0(z) = -\Lambda/z - eE_\perp z \quad , \tag{10.2}$$

$$\Lambda = \frac{e^2}{16\pi\epsilon_0}\frac{\epsilon_r - 1}{\epsilon_r + 1} \quad , \tag{10.3}$$

where $\epsilon_r = 1.056$ is liquid He_4 relative permittivity. Inside liquid helium for $z < 0$ we can set $V_a(z) = \infty$ in the energy scale of the bound states ($\sim$ 7 K). We introduced a subscript $V_a^0(z)$ to the potential since, as we will show later, $V_a(z)$ is renormalized when an in-plane magnetic field is present. For usual pressing electric fields $E_\perp \sim 2$ V mm^{-1} the main contribution to the confinement potential for the lowest eigenstates comes from the interaction with the image charge.

10.2 In-plane motion

In addition to their vertical motion, electrons on helium move horizontally as free particles - electrons with their bare electronic mass m. A perpendicular magnetic field applied to 2DES induces Lorenz force on the electrons, making electrons move circularly. This results in the Landau quantization of horizontal motion giving raise to equidistant Landau levels. According to that, the Hamiltonian for horizontal motion (up to a constant) then becomes:

$$\mathcal{H}_l = \hbar\omega_c \hat{a}^+ \hat{a} \quad , \tag{10.4}$$

where $\omega_c = eB_z/m$ is the cyclotron frequency, mentioned above in Section 8.5. This term has the same form as the Hamiltonian of a resonant cavity in QED (see Section 8.6.2), so the Landau level then plays the role of the number of light quanta in the cavity.

10.3 Coupling

With only a perpendicular magnetic field and in the limit of weak electron-electron interaction the Landau levels and Rydberg states are not coupled. A tunable coupling can be introduced by applying an in plane magnetic field [162, 163]. Indeed a magnetic field applied in the y direction will tend to turn a vertical velocity towards the x direction due to cyclotron motion along the y axis induced by the parallel field. This coupling has been investigated in double quantum wells in a regime with many occupied Landau levels [164, 165, 166]. In our measurements we focus instead on the limit where only the lowest Landau levels are occupied. The quantitative form of the interaction induced by the in-plane field can be obtained as follows. First we write the total Hamiltonian:

$$\mathcal{H} = \frac{(\mathbf{p} - e\mathbf{A})^2}{2m} + V_a^0(z) \tag{10.5}$$

Hamiltonian derivation

Using the Landau Gauge $\mathbf{A} = B_y z\mathbf{e}_x + B_z x\mathbf{e}_y$, where the vector potential doesn't have any component along the z-axis motion, this Hamiltonian can be rewritten as:

$$\begin{aligned} \hat{\mathcal{H}} = \frac{(\overline{p}_x - eB_y z)^2}{2m} + \frac{(\overline{p}_y - eB_z x)^2}{2m} + \frac{\overline{p}_z^2}{2m} + V(\bar{r}) = \\ = \frac{\overline{p}_x^2}{2m} - \frac{eB_y z}{m}\overline{p}_x + \frac{(eB_y z)^2}{2m} + \frac{(\hbar k_y - eB_z x)^2}{2m} + \frac{\overline{p}_z^2}{2m} + V(\bar{r}) \end{aligned} \tag{10.6}$$

This Hamiltonian can be expanded in the powers of B_y: to the lowest order we have $\hat{H} = \hat{H}_a + \hat{H}_l$, the first order in B_y introduces an atom-cavity interaction term $\hat{H}_c = -eB_y z\hat{p}_x/m$. Writing $\hat{H}_l$ in terms of the Landau level creation and annihilation operators we obtain the following expression:

$$\mathcal{H}_l = \hbar\omega_c \hat{a}^+\hat{a} = \frac{(\hbar k_y - eB_z x)^2}{2m} + \frac{\overline{p}_x^2}{2m} \tag{10.7}$$

Since a parallel magnetic field doesn't affect in-plane motion of the electrons, the cavity's Hamiltonian 10.7 remains the same in the presence of the B_y. Energy corrections rise when the out of plane motion is concerned: the parallel magnetic field affects the atom's Hamiltonian in a known way making a parabolic correction (diamagnetic effect) to the potential energy in Eq. (10.8):

$$V_A(z) = \frac{(\overline{p}_x^2 - eB_y z)^2}{2m} + \frac{\Lambda}{z} - eE_\perp z \tag{10.8}$$

In order to convert our Hamiltonian to a form convenient to work with, some transformations and replacements are needed. First we start with switching to generalised coordinate and momentum and centralising:

$$\hat{Q} = \left(x - \frac{\hbar k_y}{B_z}\right) \cdot \sqrt{\frac{m\omega_c}{\hbar}} \tag{10.9a}$$

$$\hat{P} = \frac{\overline{p}_x}{\sqrt{\hbar m\omega_c}} \tag{10.9b}$$

Building new operators:

$$\hat{b} = \frac{1}{\sqrt{2}}\left(\hat{Q} + i\hat{P}\right) \tag{10.10a}$$

$$\hat{b}^+ = \frac{1}{\sqrt{2}}\left(\hat{Q} - i\hat{P}\right) \tag{10.10b}$$

$$\left[b,\, b^+\right] = 1 \tag{10.10c}$$

Rewriting $\hat{Q}$ and $\hat{P}$ operators (Eq. (10.9)):

$$\begin{aligned} \hat{Q} &= \frac{1}{\sqrt{2}}\left(\hat{b} + \hat{b}^+\right) \\ \hat{P} &= -\frac{i}{\sqrt{2}}\left(\hat{b} - \hat{b}^+\right) \\ \Rightarrow \frac{\hat{Q}^2 + \hat{P}^2}{2} &= \frac{\hat{b}\hat{b}^+ + \hat{b}^+\hat{b}}{2} = \hat{b}^+\hat{b} + \frac{1}{2} \end{aligned} \tag{10.11}$$

Transforming the Hamiltonian to an intermediate form:

$$\hat{\mathcal{H}} = \left(\hat{b}^+\hat{b} + \frac{1}{2}\right)\hbar\omega_c - \frac{i}{\sqrt{2}}\frac{eB_y z}{m}\sqrt{\hbar m\omega_c}\left(\hat{b} - \hat{b}^+\right) + \frac{\left(eB_y z\right)^2}{2m} + \frac{\overline{p}_z^2}{2m} + V(\bar{r}) \tag{10.12}$$

Adding new coordinates with the same commutational properties as operators (10.10):

$$\begin{aligned} a &= ib \\ a^+ &= -ib^+ \\ \left[a,\, a^+\right] &= 1 \end{aligned} \tag{10.13}$$

getting Hamiltonian (10.12):

$$\hat{\mathcal{H}} = \left(\hat{a}^+\hat{a} + \frac{1}{2}\right)\hbar\omega_c + \frac{1}{\sqrt{2}}\frac{eB_y z}{m}\sqrt{\hbar m\omega_c}\left(\hat{a}^+ + \hat{a}\right) + \frac{\left(eB_y z\right)^2}{2m} + \frac{\overline{p}_z^2}{2m} + V(\bar{r}) \tag{10.14}$$

The eigenvalues of $\frac{(eB_y z)^2}{2m} + \frac{\overline{p}_z^2}{2m} + V(\bar{r})$ we calculated numerically by $C{+}{+}$ computations. Then making some simplifications we get the following form:

$$\hat{\mathcal{H}} = \hbar\omega_c\hat{a}^+\hat{a} + \sum \varepsilon_n \left|n\right\rangle\left\langle n\right| + \frac{1}{\sqrt{2}}\frac{eB_y z}{m}\sqrt{\hbar m\omega_c}\left(\hat{a}^+ + \hat{a}\right) \tag{10.15}$$

Thus we obtain the following expression:

$$\hat{\mathcal{H}} = \hbar\omega_c\hat{a}^+\hat{a} + \sum_n \varepsilon_n \left|n\right\rangle\left\langle n\right| + \frac{\hbar eB_y}{m\sqrt{2}}\left(\hat{a}^+ + \hat{a}\right)\frac{\hat{z}}{\ell_B} \tag{10.16}$$

In this equation we introduced the magnetic length for the perpendicular field $\ell_B = \sqrt{\hbar/(m\omega_c)}$, the notation $\hat{z}$ stands for the matrix elements of the z operator on the vertical eigenstates $|n\rangle$, it plays here the role of the dipole moment operator in quantum electrodynamics. This formula covers Jaynes-Cummings Hamiltonian 8.27, where the last term stands for interaction (like the interaction term of Jaynes-Cummings Hamiltonian 8.26) and depends directly on the parallel magnetic field strength B_y.

One should note that the rotating wave approximation usually performed for Jaynes-Cummings Hamiltonian derivation does not work for our calculations, we keep the rotating part. Besides, in our model we do not dismiss higher atomic and Landau levels, which are normally neglected in Jaynes-Cummings model.

As a conclusion, the QED Hamiltonian Eq. (10.16) appears in models where a photon mode in a cavity/harmonic oscillator (Landau levels in our experiment) is coupled to an atom/qubit provided by Rydberg states. The strength of the interaction, which would be the vacuum Rabi splitting in atomic physics, is directly controllable and proportional to B_y allowing in principle couplings of arbitrary strength.

This Hamiltonian may seem valid to first order in B_y, however the second order diamagnetic term $m\omega_y^2 z^2/2$ only renormalizes the vertical confinement potential $V_a(z) = V_a^0(z) + m\omega_y^2 z^2/2$. Thus Eq. (10.16) remains valid for arbitrary interaction strength keeping in mind that the in-plane magnetic field then not only controls the coupling strength between the atom and Landau levels but also changes the atom energies ϵ_n and the dipole momentum matrix $\hat{z}$, which can still be obtained easily by solving the one dimensional Schrödinger equation Eq. (11.1) in the modified confinement potential.

Chapter 11

Coupling Rydberg atom to Landau levels

11.1 Stark spectroscopy

Stark spectroscopy provides an efficient tool to manipulate atomic energy levels. As discussed in previous Chapters, a pressing perpendicular static electric field $E_\perp$ allows to shift the Rydberg levels through linear Stark effect [161]. Then the spectroscopic positions of the Rydberg states is well described by a one-dimensional Schrödinger equation for vertical motion:

$$\mathcal{H}_a = -\frac{\hbar^2}{2m}\frac{\partial^2}{\partial z^2} + V_a(z) = \sum_n \varepsilon_n \left|n\right\rangle \left\langle n\right| \tag{11.1}$$

Applied MW induces atomic transitions between Rydberg levels of the system $\Delta n = \pm 1$. Their energy may be tuned by shifting the levels through changing the $E_\perp$. In our Stark spectroscopy measurements we did the opposite: varying the MW frequency for weak parallel magnetic fields the transition from the ground $|g\rangle$ to the first excited Rydberg state $|e\rangle$ manifests as a resonance of the microwave induced change in admittance as function of $E_\perp$. Series of measurements proved linear shift, according to our expectations.

In the absence of perturbing parallel magnetic field $B_y = 0$ T, we observed following shift:

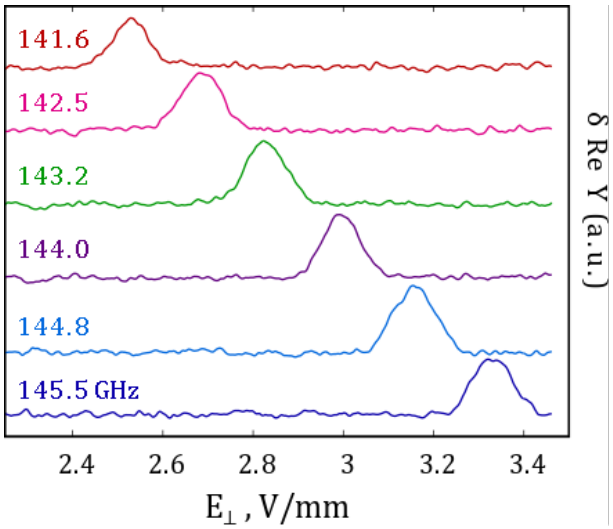

Figure 11.1: Spectra measured at different applied MW frequencies in swept confinement voltage $E_\perp$. Resonance's position in electric field shifts linearly with the frequency. $B_z = 0.73$ T, $B_y = 0$ T.

Linearity of the effect allows us to make a useful voltage-frequency calibration in order to switch to energy units:

$$h\nu = \Delta + \alpha V_\perp \tag{11.2}$$

We will further use this calibration to analyse parallel magnetic field effect. The resonance position at energy $h\nu_0 = \epsilon_e - \epsilon_g$ shifts linearly with $E_\perp$, the slope can be obtained from the Schrödinger equation Eq. (11.1) with small deviations due to uncertainties on geometrical parameters.

11.2 Detuning

This result corresponds very well to expected behaviour of an isolated atom with no coupling (see Chapter 10). However, we would like to test, if applying a parallel magnetic field does indeed induce coupling between independent terms of an initial Hamiltonian, concerning the atom being tuned by Stark effect, and also a cavity. Repeating the same Stark spectroscopy measurements in a case of non-zero parallel magnetic field, we observed $|g\rangle \rightarrow |e\rangle$ transition's resonances at different $E_\perp$ voltages for the same set of MW frequencies. Figure 11.2 represents the difference between cases of $B_y = 0$ and $B_y \neq 0$. On panel (a) linear shifts due to Stark effect for $B_y = 0$ (red) and 0.25 T (blue) are plotted, non-zero field case is detuned from non-perturbed atomic transition's line. Panel (b) shows an example of resonances at the same frequency 141.6 GHz for these two cases.

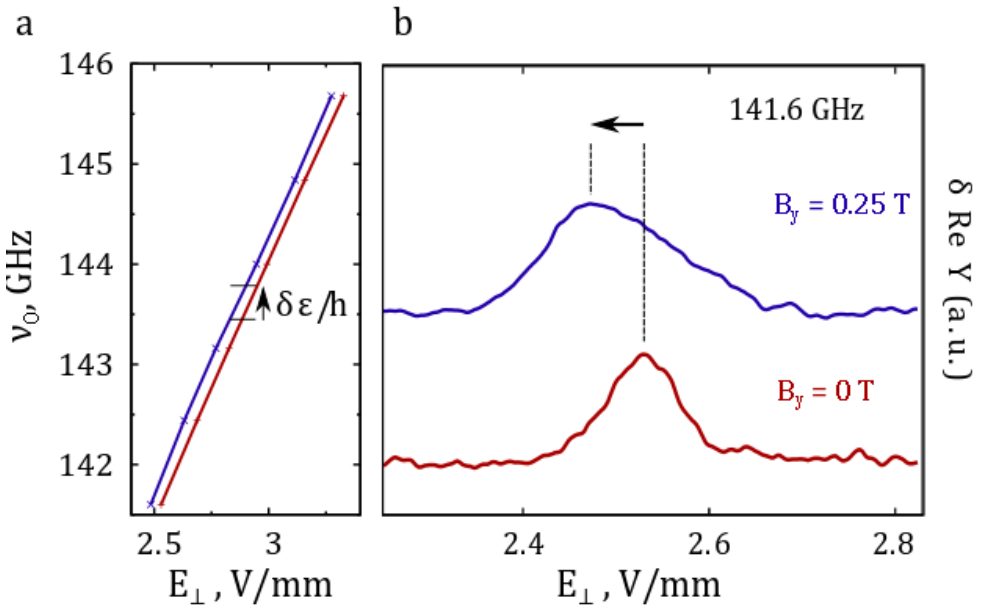

Figure 11.2: **a**, Resonance positions shift slopes for $B_y = 0.25$ T (blue) and $B_y = 0$ T (red). $\delta\epsilon/h$ is the detuning value in energy units for $B_y = 0.25$ T. **b**, Example spectra at 141.6 GHz for $B_y = 0$ and 0.25 T, $B_z = 0.73$ T.

The slope is almost independent of B_y (see Fig. 11.2b), indeed for $B_y \leq 1$ Tesla the coupling term of the QED Hamiltonian $\frac{\hbar\omega_y}{\sqrt{2}}\frac{\langle e|\hat{z}|g\rangle}{\ell_B} \lesssim 10$ GHz is small compared to $h\nu_0 \simeq 140$ GHz and does not change the vertical dipole moment significantly. While the slope as function of $E_\perp$ remains unchanged, an overall energy shift $\delta\epsilon$ is visible. It appears due to the coupling between Rydberg states and Landau levels at finite B_y. We define δ as the detuning induced by the Shark shift due to the deviation of $E_\perp$ from its resonant value at the excitation frequency f for $B_y = 0$; δ is thus the difference between $E_\perp$ and its value at resonance $\simeq 2$ Vmm^{-1} times (minus) the slope measured in Fig.11.2b. In the following, we present a careful experimental investigation of the coupling induced energy shift and show that it can be understood quantitatively from the QED Hamiltonian.

11.3 Experimental investigation of the parallel magnetic field effect

To study the evolution of the $|g\rangle \rightarrow |e\rangle$ transition with B_y, we take advantage of the linear dependence of the energy shifts on $E_\perp$, which enables us to fix the excitation frequency to $f = 139$ GHz and change only $E_\perp$.

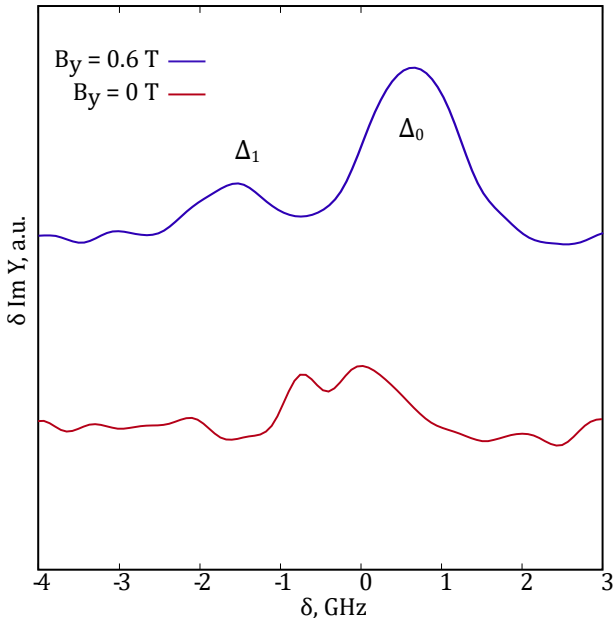

Figure 11.3: Spectra comparison for $B_y = 0.6$ T (blue) and $B_y = 0$ T (red) at $B_z = 1.05$. Both spectra are normalized to $B_y = 0$ T maximum intensity.

Figure 11.3 shows example spectra obtained at $B_y = 0$ and $B_y = 0.6$ T and $B_z = 1.05$ T at $f_{MW} = 138.96$ GHz. Now there is not only the resonance shift, but also a peculiar splitting of the initial peak. We consider this splitting to be due to parallel magnetic field resolution of two close atomic transitions $\Delta n = \pm 1$ with different Landau level numbers m involved (Fig. 11.3), which we call Δ_0 and Δ_1 transitions.

In order to investigate this we measured spectra sweeping the $E_\perp$ voltage with varying parallel magnetic field B_y at different values of fixed perpendicular magnetic field $B_z \neq 0$. All the collected data is then transformed into map where the change in admittance is plotted as function of B_y and of the detuning δ (Fig. 11.4). Four panels show maps for four perpendicular magnetic field values: $B_z = 1.3$, 1.05, 0.85 and 0.73 T. These maps reveal similar "butterfly" patterns (note: do not confuse with Hofstadter's butterfly), consisting of two transitions, resolving symmetrically with parallel field B_y. The two resolved transitions are pretty different in their behaviour. Upward going "wings" of the butterfly - we consider it to be Δ_0 transition from figure 11.3 - reveals increasing with parallel magnetic field strength B_y distance between involved energy levels. Whereas downward going "wings" - Δ_1 transition from figure 11.3 - shows decreasing distance. Such behaviour means that at a moderate range B_y affects differently Landau levels associated with different number of quanta in the "cavity".

Besides, Δ_0 transition is more intense at every fixed perpendicular magnetic field value B_z and its' coupling strength dependence is almost the same for all B_z in our data set. At weak B_y its' energy increases quadratically and at higher fields it becomes more linear. Δ_1 transition splits off from the main transition as B_y becomes stronger. Another interesting

feature is that Δ_1 transition line's slope as function of the coupling strength increases significantly with B_z.

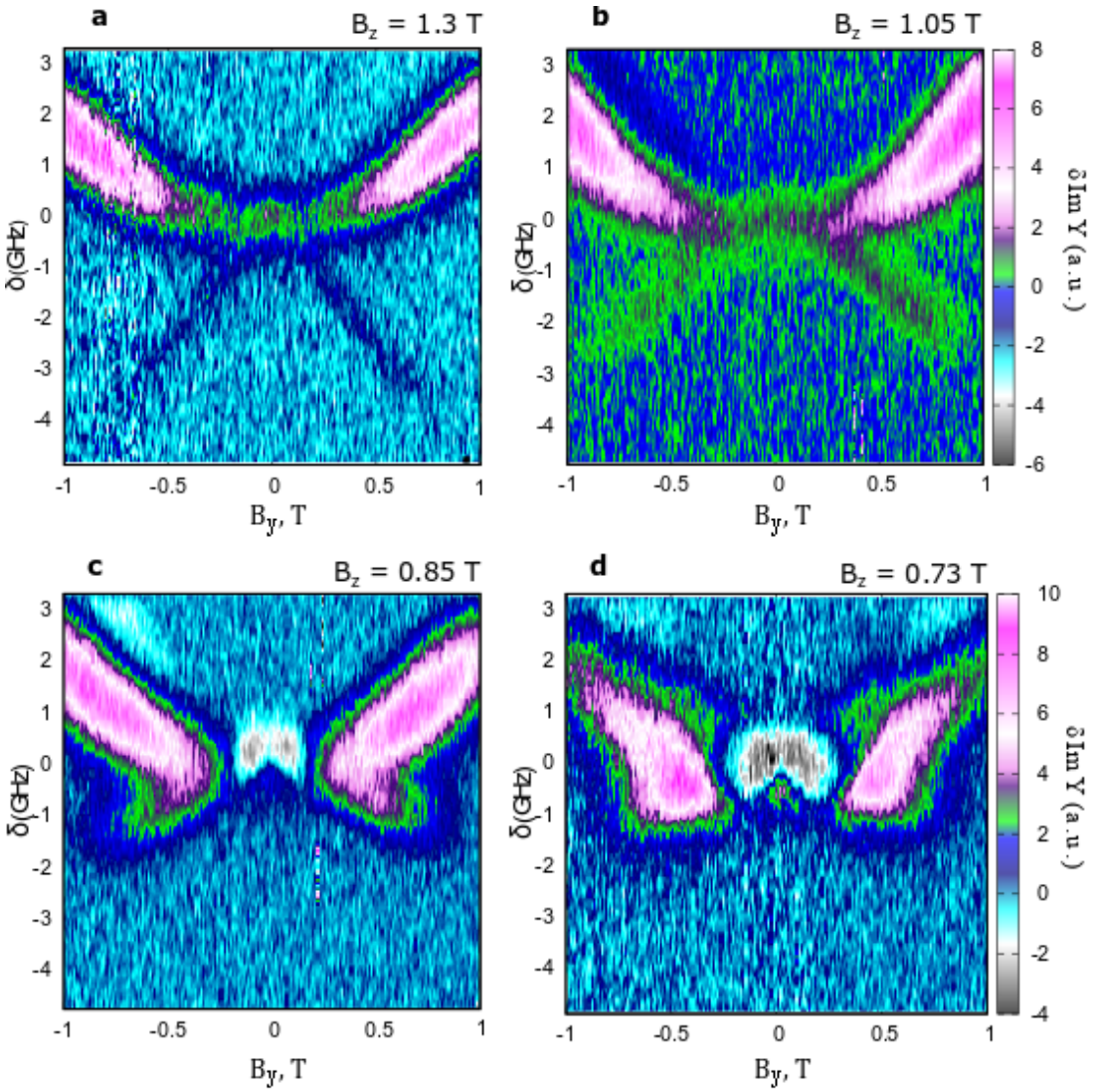

Figure 11.4: Stark spectroscopy experimental maps, measured at (**a**) $B_z = 1.3$ T, (**b**) $B_z = 1.05$ T, (**c**) $B_z = 0.85$ T and (**d**) $B_z = 0.73$ T. Horizontal x-axis correspond to swept parallel magnetic field B_y, vertical y-axis represents $E_\perp$ voltage converted into energy units via Eq. 11.2, colour scale z-axis is the admittance change.

11.4 QED analysis of magnetic fields effect on the energy levels of 2DEG

Witnessed splitting of the Rydberg transition can be understood from the energy level diagram in Fig. 11.5, which shows how the energy levels from the QED Hamiltonian evolve with the coupling strength. For each atomic state $|n\rangle$, the manifold of dressed states consists of a ladder of Landau levels $|n, m\rangle$. Distance between equidistant Landau

levels is defined by the perpendicular magnetic field strength B_z, since it is this field creates Lorenz force inducing Landau oscillations of the electrons, as discussed in Chapter 10. Applied MW excites transitions that conserve the Landau level number m (between states with the same number of photons in the cavity $|n, m\rangle \rightarrow |n \pm 1, m\rangle$, $|\Delta m = 0)$. Without parallel magnetic field the energy of the $|g, m\rangle \rightarrow |e, m\rangle$ transition does not dependent on m.

The coupling term $\frac{\hbar e B_y}{m\sqrt{2}} (\hat{a}^+ + \hat{a}) \frac{\hat{z}}{\ell_B}$ of our QED Hamiltonian 5.1 derived in Chapter 10 is responsible for lifting this degeneracy in the presence of the $B_y \neq 0$, making transitions associated to different Landau levels spectroscopically distinguishable. For example, in the special case of the $m = 0$ transition $|g, 0\rangle \rightarrow |e, 0\rangle$ with energy Δ_0 the renormalization of the transition energy is due to an interaction with the lowest Landau level. It can be seen as an effective Lamb shift in analogy with atomic physics, circuit QED [167, 156], coupling to phonons in quantum dots and with ripplons for electrons on helium [168]. A similar renormalization occurs for all the transitions $|g, m\rangle \rightarrow |e, m\rangle$, and simulations are thus needed to identify the observed spectroscopic lines as one of the transitions Δ_m.

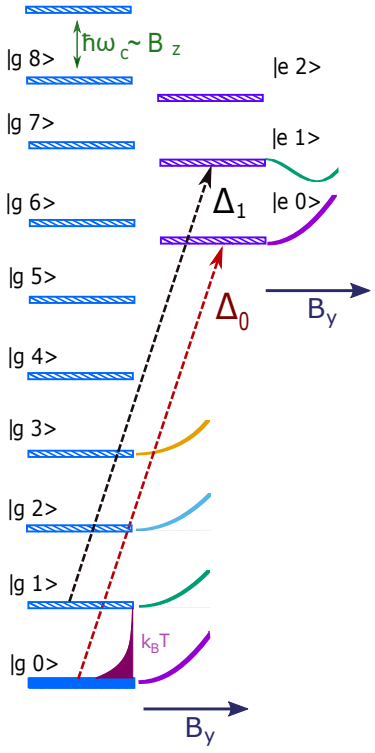

Figure 11.5: 2DEG energy levels diagram. States are denoted as $|n, m\rangle$, where the first quantum number gives the atomic state and m is Landau level number (number of photons in the cavity). Distance between Landau levels is defined by B_z. Δ_0 and Δ_1 resonant peaks from figure 11.3 correspond to m quanta number conserving $(\Delta m = 0)$ $|g0\rangle \rightarrow |e0\rangle$ and $|g1\rangle \rightarrow |e1\rangle$ transitions. The calculated evolution of individual levels (rescaled for visibility) with B_y up to 1 T is shown by coloured lines.

The QED Hamiltonian 5.1 gives a quantitative prediction on the renormalization of the transition energies Δ_m. Here we emphasize that all the parameters appearing in the model involve $E_\perp$, the applied magnetic field, the liquid Helium dielectric constant ϵ and fundamental constants, there are thus no fitting parameters. The values of Δ_m can be obtained from the numerical diagonalization of Hamiltonian 5.1, to obtain accurate values we had to include Rydberg states and Landau levels at an energy scale higher than $\hbar\nu_0$ from $|g,0\rangle$, in the simulations shown here we used a basis set of 100 Landau levels and 20 Rydberg states. Results of our simulations for transitions $\Delta_{0,1}$ are overlaid on top of the experimental data (Fig. 11.6). We see that they reproduce accurately both upper and lower "butterfly wings", including the striking increase of $\Delta_1(B_y)$ with B_z which contrasts with the Δ_0 transition that is almost B_z independent.

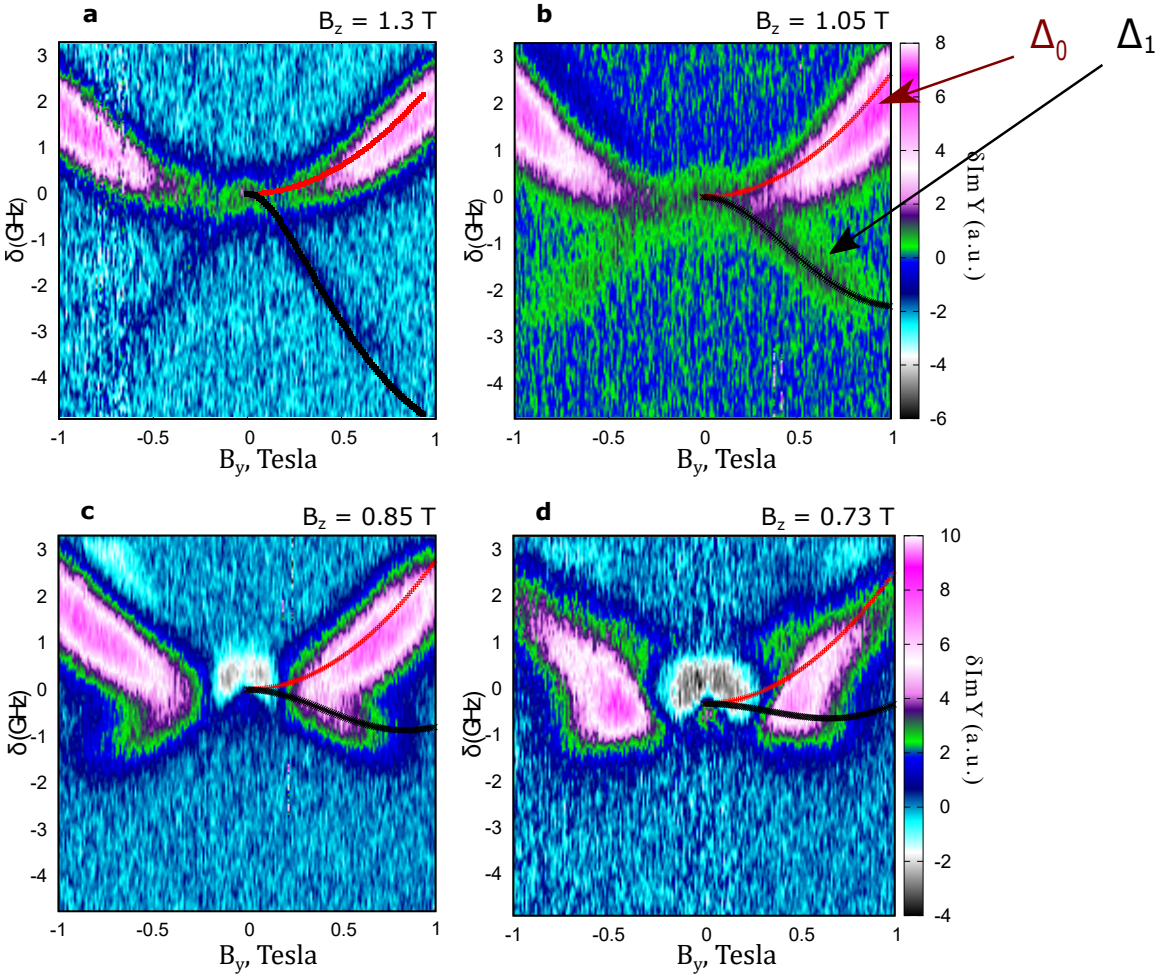

Figure 11.6: QED Hamiltonian calculations results overlaid on the experimental maps from figure11.4. Red and black curves give the QED Hamiltonian predictions for the Δ_0 and Δ_1 transitions drawn in figure 11.5 between states $|n,m\rangle$.

11.5 Population mechanisms

We claim that for understanding the intensity difference of the transitions $\Delta_{0,1}$ and the Δ_1 transition's vanishing with $B_y \lesssim 1$ Tesla, one needs to consider the involved levels population mechanism. Indeed, the transitions Δ_m between states $|g,m\rangle \rightarrow |e,m\rangle$ can only be observed, if the initial state $|g,m\rangle$ is populated. At the experiment temperature $T = 0.3$ K only the ground state $|g,0\rangle$ is populated in equilibrium. The thermal population of $|g,1\rangle$ state at $T = 0.3$ K and $B_z = 1$ T is only 1%. As a consequence, transitions Δ_m with $m \geq 1$ require an external excitation to become visible.

We performed power dependence measurements at fixed magnetic fields strengths $B_z = 1$ T and $B_y = 0.5$ T. MW excitation power was varied in a range $2.5 - 10$ mW. Although these numbers are relative, since as it was mentioned in the Chapter 9, MW distribution inside of the cell was inhomogeneous and we don't know exact values of the power in the cell. In Fig. 11.7(a) we show that indeed Δ_1 transition physically appears only when the MW power is high enough, as opposed to the Δ_0 transition which is present even at low MW power. Two possible mechanisms to populate the $|g,1\rangle$ level may be taken into consideration. The first one assumes in-plane component of the MW electric field populating a $|g,1\rangle$ level non-resonantly from the initial $|g,0\rangle$ level. The second one is illustrated with dashed lines on the Fig. 11.7(b). When the energy of the transitions $\Delta_{0,1}$ are sufficiently close (at low B_y) a Δ_1 energy MW photon can also excite a transition into the $|e,0\rangle$ state, scattering can then transfer some population into a nearby $|g,m\rangle$ level, leading (after relaxation) to a finite population in the $|g,1\rangle$ state which makes the transition Δ_1 visible. This can also explain why the Δ_1 transition disappears faster than the Δ_0 transition with B_y and $E_\perp$ applied (see figures 11.4 and 11.6). This observation can be understood within the population mechanism for $|g,1\rangle$ shown in Fig. 11.7b. Indeed at larger B_y the energies of the $\Delta_{0,1}$ transitions become different and the MW excitation at the Δ_1 frequency can no longer excite the Δ_0 transition which populates the $|g,1\rangle$ level. The state $|g,1\rangle$ then remains empty leading to the disappearance of the Δ_1 wings.

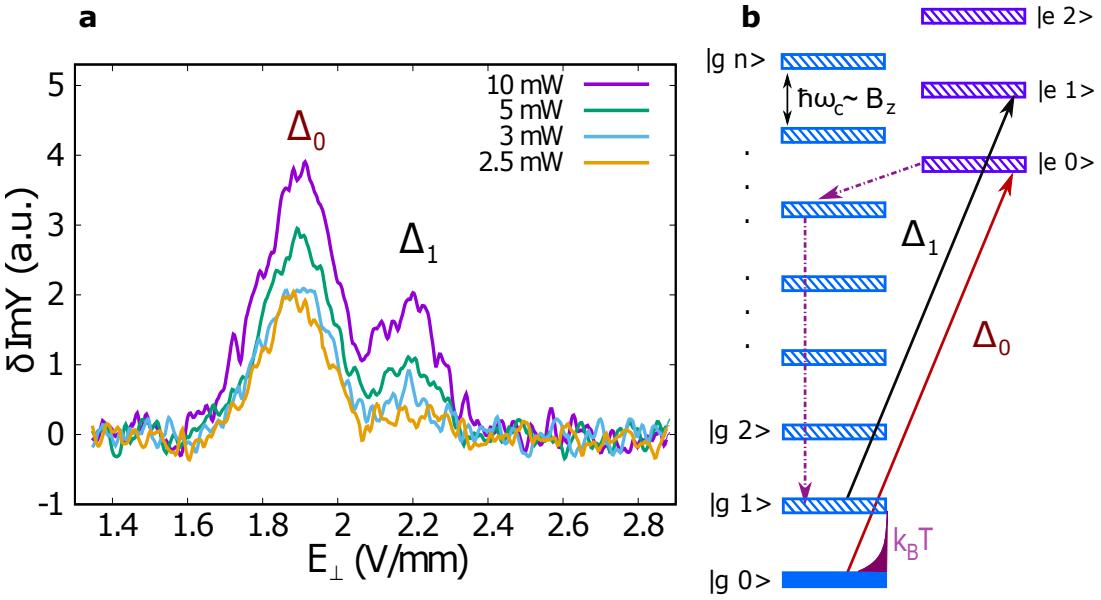

Figure 11.7: **a** Dependence of the $\Delta_{0,1}$ resonances on MW excitation power at $B_z = 1$ T, $B_y = 0.5$ T. The Δ_1 transition disappears at low power. **b** illustrates how the Δ_0 transition can populate the $|g,1\rangle$ level, if the energies $\Delta_{0,1}$ are close, MW photons at the Δ_1 energy can also induce the Δ_0 transition providing the non-equilibrium population needed to see the resonance at Δ_1.

In conclusion, we observed linear Stark shift of the Rydberg atom's levels with the applied MW frequency. Then we showed that applied parallel magnetic field affects the shifted resonant positions, even though the slope of the shift remained independent of the field. We investigated experimentally the effect of the parallel magnetic field in more details, since according to our Hamiltonian 5.1 derived in the previous Chapter 10 it is B_y strength responsible for the interaction between the Rydberg atom and Landau levels in our system. We found that initial transition Δ_0 from the ground $|g\rangle$ to the first excited state $|e\rangle$is degenerated. This degeneracy is lifted in the non-zero B_y yielding two peaks (Δ_0 and Δ_1) corresponding to the transitions assigned to different quanta number in the cavity - different Landau level numbers m: $|g,0\rangle \rightarrow |e,0\rangle$ and $|g,1\rangle \rightarrow |e,1\rangle$.

We measured spectroscopic maps of these transitions in different perpendicular magnetic fields. Further we compared the obtained data and transitions calculated with our QED Hamiltonian 5.1 and proved excellent matching of the experiment with the predictions.

Then we analysed the MW power dependence of the $\Delta_{0,1}$ transitions and proposed two possible mechanisms of populating the levels involved. All the measurements presented here were performed by Alexei Chepelianskii and the author.

Chapter 12

Conclusions on Part II

2-dimensional electron gas is a widely present physical object. It can be described by quantum laws and still be treated as a macroscopic system, which is much easier to manipulate experimentally. It has been studied in various materials and ambiances and we are definitely not the first ones to confine it on the surface of liquid helium, but we were the very first ones to couple two different by their physics and geometrical directions degrees of freedom of such a system.

In this Disseration we have shown that electrons confined and restricted in their vertical motion by pressing electric field $E_\perp$ have energy levels in the vertical direction following Rydberg series distribution rule due to induced image charge in the liquid helium. Besides applied perpendicular magnetic field B_z induces quantized in-plane motion of the electrons as charged particles - Landau oscillations - due to Lorenz force. This two degrees of freedom remain independent unless the parallel magnetic field B_y is applied. Then due to the same Lorenz force electrons tend to vertical motion, therefore resulting in dressing Rydberg states of the system. The interaction between no more independent degrees of freedom appeared to be easily controlled by the strength of this parallel magnetic field.

We derived step by step a theoretical description of this coupling of Rydberg states with Landau levels and ended up with Jaynes-Cummings type Hamiltonian for confined electron gas in the presence of perturbing magnetic fields. Its legitimacy was proven by numerical predictions perfectly matching the experimental results. On the top of that, the model we propose has not a single fitting parameter, involving only real physical variables and constants.

Thus we presented a brand-new approach to form a prototype quantum electrodynamics system - an atom interacting with the quantized electromagnetic field, described by well known Jaynes-Cummings model. 2-dimensional electron gas is easy to confine on the surface of liquid helium-4, therefore performing extremely pure system, where the only possible perturbations could arise from the surface ripplons, whose effect is negligible for

our experiments. Control of the population transfer between dressed states could enable tunable mm-wave lasers.

Part III

Appendix

Chapter 13

Appendix on Part I

13.1 Complete experimental scheme for ODMR measurements

The full experimental scheme of ODMR is shown on Fig. 13.1 with all the explanations given in the caption.

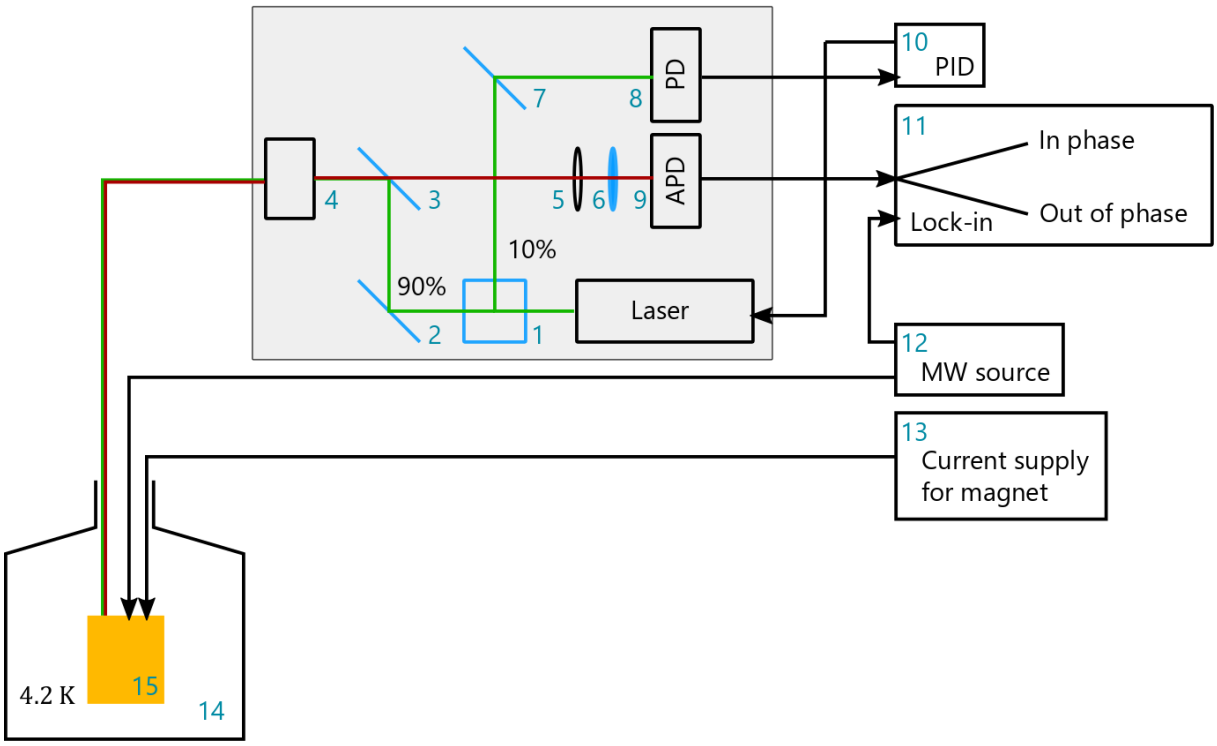

Figure 13.1: Extended version of Fig. 3.3. 532 nm laser beam (green) is splitted at splitting cubical prism *1* at ratio 90:10, then more intense part of the beam is sent to optical fiber through *4* passing mirrors *2* and *3* to sampleholder placed in the Dewer *14* at liquid He temperature. Current supply *13* was used to feed the solenoid *15*. The weaker part of the laser beam after the cube *1* goes to a supporting photodetector *8*. Signal from the supporting photodetector *8* was sent to PID *10* regularizing the voltage sent to the laser. ODMR signal (red) is obtained via the same fiber through *4*, then sent to an avalanche photodetector *6* through semi-transparent mirror *3* and focusing lens *5*. The photodetector *9* is equipped with a long-pass filter *6* to avoid colleting the laser light. Then the phase separation was performed using lock-in *11* tuned to the reference frequency from the MW source *12*. MW was sent to the sampleholder via co-axial cables.

13.2 Quintet ODMR maps fitting

13.2.1 Obtaining ϕ angle for quintets, sample II

Calculations of triplet and quintet transitions was performed using the Hamiltonian given in the main text with the following code, created by Alexei Chepelianskii with participation of Sam Bayliss and Kamila Yunusova:
https://github.com/yneter/ODMR

13.2.2 Obtaining ϕ angle for quintets, sample III

The code for single crystal transitions calculations was created by Kamila Yunusova, using using certain functions from the code mentioned above:
https://github.com/KamChaos/TransitionsTIPsttcSC/blob/master/Fig4transitionsMathematica.py

Chapter 14

Appendix on Part II

14.1 2DEG energy levels calculation

In order to calculate evolution of 2DEG energy levels with parallel magnetic field, we used the following $C++$ code, developed by Alexei Chepelianski and slightly modified by Kamila Yunusova. As it is mentioned in the main text, in the experiment we faced only two Rydberg level (ground $|g\rangle$ and first excited $|e\rangle$ states) and only two Landau levels ($m = 0, 1$). Nevertheless, our calculations revealed necessity of taking higher levels into consideration to obtain adequate results.

Listing 14.1: C++ code using listings

```
1  #include <iostream>
2  #include <cmath>
3  #include <fstream>
4  #include <vector>
5  #include <complex>
6  #include <stdlib.h>
7  #include <stdio.h>
8  #include <time.h>
9  #include <assert.h>
10 #include <algorithm>
11 #include <Eigen/Dense>
12 #include <Eigen/Sparse>
13
14
15 using namespace std;
16 using namespace Eigen;
```

```
17
18 typedef SparseMatrix<double> SparseMatrixXd;
19 typedef complex<double> complexg;
20 typedef vector<double> vectorg;
21 const complexg iii(0,1);
22 inline double sq(double x) { return x*x; }
23 inline double min(double x, double y) { return (y < x) ? y : x; }
24 inline double scalar(complexg a, complexg b)
25         { return real(a)*real(b)+imag(a)*imag(b); }
26 double myrand(void) { return (double) rand() / (double) RAND_MAX; }
27
28 double SQR( double a ) { return (a == 0.0) ? 0.0 : a*a; }
29 double SIGN( double a, double b)
30         { return ((b) >= 0.0 ? fabs(a) : -fabs(a)); }
31
32
33 typedef Triplet<double> TMatrixXd;
34
35
36 double pythag(double a, double b)
37 {
38     double absa,absb;
39     absa=fabs(a);
40     absb=fabs(b);
41     if (absa > absb) return absa*sqrt(1.0+SQR(absb/absa));
42     else return (absb == 0.0 ? 0.0 : absb*sqrt(1.0+SQR(absa/absb)));
43 }
44
45
46 // d diagonal elements
47 // e hopping elements
48 void tqli(double *d, double *e, int n)
49 {
50     int m,l,iter,i;
51     double s,r,p,g,f,dd,c,b;
52
53     for (i=1;i<n;i++) e[i-1]=e[i];
```

```
54      e[n-1]=0.0;
55      for (l=0;l<n;l++) {
56          iter=0;
57          do {
58              for (m=l;m<n-1;m++) {
59                  dd=fabs(d[m])+fabs(d[m+1]);
60                  if ((double)(fabs(e[m])+dd) == dd) break;
61              }
62              if (m != l) {
63                  g=(d[l+1]-d[l])/(2.0*e[l]);
64                  r=pythag(g,1.0);
65                  g=d[m]-d[l]+e[l]/(g+SIGN(r,g));
66                  s=c=1.0;
67                  p=0.0;
68                  for (i=m-1;i>=l;i--) {
69                      f=s*e[i];
70                      b=c*e[i];
71                      e[i+1]=(r=pythag(f,g));
72                      if (r == 0.0) {
73                          d[i+1] -= p;
74                          e[m]=0.0;
75                          break;
76                      }
77                      s=f/r;
78                      c=g/r;
79                      g=d[i+1]-p;
80                      r=(d[i]-g)*s+2.0*c*b;
81                      d[i+1]=g+(p=s*r);
82                      g=c*r-b;
83                  }
84                  if (r == 0.0 && i >= l) continue;
85                  d[l] -= p;
86                  e[l]=g;
87                  e[m]=0.0;
88              }
89          } while (m != l);
90      }
```

```
91 }
92
93
94 /*
95  * http://en.wikipedia.org/wiki/Tridiagonal_matrix_algorithm
96  */
97 void solve_tridiag_matrix (int n, const double *a, double *b,
98         const double *c, double *v, double *x)
99 {
100         /**
101          * n - number of equations
102          * a - sub-diagonal (means it is the diagonal
103          below the main diagonal)
104          * b - the main diagonal
105          * c - sup-diagonal (means it is the diagonal
106          above the main diagonal)
107          * v - right part
108          * x - the answer
109          */
110         for (int i = 1; i < n; i++)
111         {
112                 double m = a[i]/b[i-1];
113                 b[i] = b[i] - m*c[i-1];
114                 v[i] = v[i] - m*v[i-1];
115         }
116
117         x[n-1] = v[n-1]/b[n-1];
118
119         for (int i = n - 2; i >= 0; i--)
120                 x[i]=(v[i]-c[i]*x[i+1])/b[i];
121 }
122
123 int HeliumAtom_cmp(const void *a, const void *b)
124 {
125     return *((double *)a) > *((double *)b);
126 }
127 class Lanczos {
```

```
128     double SQR( double a ) { return (a == 0.0) ? 0.0 : a*a; }
129     double SIGN( double a, double b)
130             { return ((b) >= 0.0 ? fabs(a) : -fabs(a)); }
131
132     double pythag(double a, double b)
133     {
134        double absa,absb;
135        absa=fabs(a);
136        absb=fabs(b);
137        if (absa > absb) return absa*sqrt(1.0+SQR(absb/absa));
138        else return (absb == 0.0 ? 0.0 : absb*sqrt(1.0+SQR(absa/absb)));
139     }
140
141
142     void tqli(vectorg &d, vectorg &e, int n)
143     {
144         int m,l,iter,i;
145   double s,r,p,g,f,dd,c,b;
146
147   for (i=1;i<n;i++) e[i-1]=e[i];
148   e[n-1]=0.0;
149   for (l=0;l<n;l++) {
150     iter=0;
151     do {
152       for (m=l;m<n-1;m++) {
153         dd=fabs(d[m])+fabs(d[m+1]);
154         if ((double)(fabs(e[m])+dd) == dd) break;
155       }
156       if (m != l) {
157         g=(d[l+1]-d[l])/(2.0*e[l]);
158         r=pythag(g,1.0);
159         g=d[m]-d[l]+e[l]/(g+SIGN(r,g));
160         s=c=1.0;
161         p=0.0;
162         for (i=m-1;i>=l;i--) {
163           f=s*e[i];
164           b=c*e[i];
```

```
165             e[i+1]=(r=pythag(f,g));
166             if (r == 0.0) {
167               d[i+1] -= p;
168               e[m]=0.0;
169               break;
170             }
171             s=f/r;
172             c=g/r;
173             g=d[i+1]-p;
174             r=(d[i]-g)*s+2.0*c*b;
175             d[i+1]=g+(p=s*r);
176             g=c*r-b;
177           }
178           if (r == 0.0 && i >= l) continue;
179           d[l] -= p;
180           e[l]=g;
181           e[m]=0.0;
182         }
183       } while (m != l);
184     }
185       }
186
187
188
189       void eigen_tqli(VectorXd &d, VectorXd &e, int n)
190       {
191           int m,l,iter,i;
192           double s,r,p,g,f,dd,c,b;
193
194           for (i=1;i<n;i++)
195       e(i-1) = e(i);
196           e(n-1) = 0.0;
197           for (l=0;l<n;l++) {
198       iter=0;
199       do {
200           for (m=l;m<n-1;m++) {
201             dd=fabs(d(m))+fabs(d(m+1));
```

```
202             if ((double)(fabs(e(m))+dd) == dd) break;
203         }
204         if (m != l) {
205             g = (d(l+1)-d(l))/(2.0*e(l));
206             r = pythag(g,1.0);
207             g = d(m)-d(l)+e(l)/(g+SIGN(r,g));
208             s = c =1.0;
209             p = 0.0;
210             for (i=m-1;i>=l;i--) {
211         f = s*e(i);
212         b = c*e(i);
213         e(i+1) = (r=pythag(f,g));
214         if (r == 0.0) {
215             d(i+1) -= p;
216             e(m)=0.0;
217             break;
218         }
219         s=f/r;
220         c=g/r;
221         g=d(i+1)-p;
222         r=(d(i)-g)*s+2.0*c*b;
223         d(i+1)=g+(p=s*r);
224         g=c*r-b;
225             }
226             if (r == 0.0 && i >= l) continue;
227             d(l) -= p;
228             e(l)=g;
229             e(m)=0.0;
230         }
231     } while (m != l);
232         }
233      }
234
235
236      void eigen_load_rand_vector(VectorXd &v)
237      {
238         for (int i = 0; i < v.rows(); i++) {
```

```
239     v(i) = myrand();
240         }
241         double norm = v.norm();
242         v /= norm;
243     }
244
245     void eigen_load_rand_vector(VectorXcd &v)
246     {
247         for (int i = 0; i < v.rows(); i++) {
248     v(i) = myrand() + iii * myrand();
249         }
250         double norm = v.norm();
251         v /= norm;
252     }
253
254     complexg scalar_product(const VectorXcd &v1, const VectorXcd &v2) {
255         VectorXcd Z(1);
256         Z =  v1.adjoint() * v2;
257         return Z(0);
258     }
259
260
261     double scalar_product_real(const VectorXcd &v1, const VectorXcd &v2) {
262         double s = 0;
263         for (int i=0; i < v1.size(); i++) {
264     s += ( real(v1(i)) * real(v2(i)) + imag(v1(i)) * imag(v2(i)) );
265         }
266         return s;
267     }
268
269     double scalar_product(const VectorXd &v1, const VectorXd &v2) {
270         VectorXd Z(1);
271         Z =  v1.transpose() * v2;
272         return Z(0);
273     }
274
275
```

```
276
277     int find_evals(vectorg &evals, vectorg &d, double epsilon) {
278        int finsize = d.size();
279        int found = 0;
280        double foundval;
281        for (int ic = 0; ic < finsize-1; ic++) {
282     if (!found && abs(d[ic]-d[ic+1]) < epsilon) {
283        evals[found++] = foundval = d[ic];
284     } else if
285     ( abs(d[ic]- foundval) > 10.0 * epsilon  && abs(d[ic]-d[ic+1]) < epsilo
    ↪ ) {
286       evals[found++] = foundval = d[ic];
287     }
288        }
289        return found;
290     }
291
292
293
294     int find_eval_abs(vectorg &evals, vectorg &d, double epsilon) {
295        int finsize = d.size();
296        for (int i = 0; i < d.size(); i++) {
297     d[i] = abs(d[i]);
298        }
299
300        sort(d.begin(), d.end());
301
302        int found = 0;
303        double foundval;
304        for (int ic = 0; ic < finsize-1; ic++) {
305     if (!found && abs(d[ic]-d[ic+1]) < epsilon) {
306        evals[found++] = foundval = d[ic];
307     } else if ( abs(d[ic]- foundval) > 10.0 * epsilon
308             && abs(d[ic]-d[ic+1]) < epsilon  ) {
309       evals[found++] = foundval = d[ic];
310
311       if (found > evals.size()/2) {
```

```
312           double mindiff = abs(evals[1] - evals[0]);
313           int minj = 0;
314           for (int j = 1; j < found-1; j++) {
315         if ( abs(evals[j+1] - evals[j]) < mindiff ) {
316           mindiff = abs(evals[j+1] - evals[j]);
317           minj = j;
318         }
319           }
320
321           for (int j = minj+1; j < found-1; j++) {
322         evals[j] = evals[j+1];
323           }
324           found--;
325         }
326       }
327          }
328          for (int i = 0; i < found; i++) {
329       evals[2 * found - i -1] = evals[i];
330       evals[i] = -evals[i];
331          }
332
333          sort(evals.begin(), evals.end());
334
335          return 2*found;
336       }
337
338
339   public :
340
341       bool electron_hole_symmetry;
342
343       Lanczos(void) {
344            electron_hole_symmetry = false;
345       }
346
347
348     /*
```

```
349     * Lanczos diagonalization function for symmetric matrixes ...
350     * Z   : pointer to a vector of lists containing the column number of all
351     * non-zero elements for each line of the matrix.
352     * Res : eigenvalue vector
353     * niter: number of iterations
354     * epsilon : target error on eigenvalues
355     * returns: number of found eigenvales
356     */
357      int eigenvalues(SparseMatrixXd &Z, vectorg &Res,
358              int niter, double epsilon)
359      {
360         int n = Z.rows();
361
362
363         VectorXd W(n);
364         eigen_load_rand_vector(W);
365         VectorXd V = VectorXd::Zero(n);
366
367         int phi = 4;
368         int maxJ = phi * n;
369         vectorg B (maxJ+1);
370         B[0] = 1.0;
371         vectorg A (maxJ+1);
372         vectorg d(maxJ+1);
373         vectorg e(maxJ+1);
374
375         int j = 0;
376
377         int finsize;
378
379         for (int iter = 0; iter < niter; iter++) {
380           while (j < maxJ) {
381            if (j) {
382            // W <- Q_{j+1} = r_j / \beta_j  and V <- \beta_j Q_{j}
383              for (int i = 0; i < n; i++) {
384                double t = W(i);
385               W(i) = V(i)/B[j];
```

```
386                 V(i) = -B[j] * t;
387               }
388             }
389
390
391             // matrix vector multiplication : A Q_{j+1}
392             // V <- A Q_{j+1} - \beta_j Q_{j}
393             V += Z * W;
394
395             // \alpha_j =
396             //      =<Q_{j+1}, A Q_{j+1} - \beta_j Q_{j}> = <Q_{j+1}, A Q_{j+1
397             A[j] = scalar_product(W,V);
398
399             // V <- (A - \alpha_j) Q_{j+1} - \beta_j Q_{j}
400             V -= A[j] * W;
401
402             j++;
403
404          if (j >= B.size()) {
405            phi++;
406            A.resize(phi*n);
407            B.resize(phi*n);
408          }
409
410          if (j < B.size()) {
411            B[j] = V.norm();
412          }
413        }
414
415        finsize = j;
416          }
417
418
419          d.resize(finsize);
420          e.resize(finsize);
421
422          for (int q=0; q<finsize; q++) {
```

```
423         d[q] = A[q];
424         e[q] = B[q];
425          }
426          tqli (d , e, finsize);
427 
428          sort(d.begin(), d.begin()+finsize);
429 
430          int neval_found;
431          neval_found = find_evals(Res, d, epsilon);
432          return neval_found;
433      }
434 
435 
436 };
437 
438 
439 /*
440  * ( -d^2/d x^2 + (x - x_c)^2/2 ) \psi(x) = E \psi(x)
441  *
442  */
443 class HeliumAtom {
444      double *Diagonal;
445      double *Hopings;
446      double *Eigenvalues;
447 
448      double *prev_vec;
449      double *next_vec;
450 
451      double **zdip_eig;
452      double **psi_coefs;
453 
454      double Delta;
455      int N;
456      int N_Z;
457      double Edc;
458 
459 public :
```

```
460     HeliumAtom(void) {
461       N = 0;
462       N_Z = 0;
463     }
464
465     void set_N_Z(int newNz){
466       N_Z = newNz;
467       zdip_eig = new double* [N_Z];
468       Eigenvalues    = new double [N_Z];
469
470       for (int z = 0; z < N_Z; z++) {
471         zdip_eig[z] = new double [N_Z];
472       }
473     }
474
475
476
477
478     HeliumAtom(int newNz) {
479       N = 0;
480       set_N_Z(newNz);
481     }
482
483     void alloc(double delta, int n) {
484         delete Eigenvalues;
485         if (N) {
486        delete Diagonal;
487        delete Hopings;
488        delete next_vec;
489        delete prev_vec;
490     }
491         N = n;
492     Delta = delta;
493         Diagonal       = new double [N];
494         Hopings        = new double [N];
495     Eigenvalues    = new double [N];
496     next_vec       = new double [N];
```

```
497       prev_vec       = new double [N];
498
499       psi_coefs = new double* [N_Z];
500       for (int z = 0; z < N_Z; z++) {
501          psi_coefs[z] = new double [N];
502       }
503       }
504
505       HeliumAtom(double delta, int n) {
506           N = 0;
507       alloc(delta, n);
508       }
509
510   private :
511       double valx(int i) {
512           return Delta * (i+1.0);
513       }
514
515       double U(double x) {
516           return -1.0/x + Edc * x;
517       }
518
519       void normalize(int n, double *vec) {
520          double norm = 0.0;
521          for (int i = 0; i < n; i++) {
522         norm += sq(vec[i]);
523          }
524          double inv = 1.0 / sqrt(norm);
525          for (int i = 0; i < n; i++) {
526         vec[i] *= inv;
527          }
528       }
529
530       void eigenvector(int level) {
531          double lambda =  Ez(level);
532
533          for (int i = 0; i < N; i++) {
```

```
534         prev_vec[i] = 1.0;
535          }
536          normalize(N, prev_vec);
537
538          for (int count = 0; count < 10; count++) {
539         create_matrix(Edc);
540         for (int i = 0; i < N; i++) Diagonal[i] -= lambda;
541         solve_tridiag_matrix(N, Hopings, Diagonal,
542               Hopings, prev_vec, next_vec);
543         for (int i = 0; i < N; i++) prev_vec[i] = next_vec[i];
544         normalize(N, prev_vec);
545          }
546
547          for (int i = 0; i < N; i++) psi_coefs[level][i] = prev_vec[i];
548
549          double sum = 0.0;
550          for (int i = 0; i < N; i++) sum += sq(psi_coefs[level][i])*Delta;
551
552          double inorm = 1.0/sqrt(sum);
553          for (int i = 0; i < N; i++) {
554        psi_coefs[level][i] *= inorm;
555          }
556
557      }
558
559
560      double z_dip(int level_1, int level_2) {
561      double s = 0.0;
562      for (int i = 0; i < N; i++)
563          {s += psi_coefs[level_1][i]*psi_coefs[level_2][i] * Delta * valx(i)
564      return s;
565      }
566
567  public :
568      int Nz(void) { return N_Z; }
569
570      void create_matrix(double newEdc) {
```

```
571          Edc = newEdc;
572          for (int i = 0; i < N; i++)
573          Diagonal[i] = 1.0/(Delta*Delta) + U(valx(i)) ;
574       for (int i = 0; i < N; i++)
575          Hopings[i] = -1.0/(2.0*Delta*Delta);
576       }
577
578
579
580       void create_matrix(double newEdc, double Bpar, double kx) {
581          Edc = newEdc;
582          for (int i = 0; i < N; i++) {
583          Diagonal[i] = 1.0/(Delta*Delta) + U(valx(i)) ;
584          Diagonal[i] += sq(kx - Bpar * valx(i))/2.0;
585       }
586       for (int i = 0; i < N; i++)
587          Hopings[i] = -1.0/(2.0*Delta*Delta);
588       }
589
590
591
592       void diag(void) {
593           tqli(Diagonal, Hopings, N);
594       qsort((void *)Diagonal, N, sizeof(double), HeliumAtom_cmp);
595       for (int i = 0; i < N; i++) {
596          Eigenvalues[i] = Diagonal[i];
597       }
598       for (int l = 0; l < N_Z; l++) {
599          eigenvector(l);
600       }
601
602       for (int l1 = 0; l1 < N_Z; l1++) {
603          for (int l2 = 0; l2 < N_Z; l2++) {
604             zdip_eig[l1][l2] = z_dip(l1, l2);
605          }
606       }
607       }
```

```
608
609     double z_field(void) { return Edc; }
610
611     double Ez(int n) {  return Eigenvalues[n]; }
612
613     double zdip_field(int i, int j) {
614        return zdip_eig[i][j];
615     }
616
617     double scalar(int level_1, int level_2) {
618     double s = 0.0;
619     for (int i = 0; i < N; i++) s += psi_coefs[level_1][i]*psi_coefs[level_
620     return s;
621     }
622
623     void write_dip_matrix(const char *name) {
624        ofstream file;
625        file.open(name);
626        for (int i = 0; i < N_Z; i++) {
627           for (int j = 0; j <  N_Z; j++) {
628          file << zdip_eig[i][j] << endl;
629       }
630        }
631        file.close();
632     }
633
634     void write_spectrum(const char *name) {
635        ofstream file;
636        file.open(name);
637        for (int i = 0; i < N_Z; i++) {
638       file << Eigenvalues[i] << endl;
639        }
640        file.close();
641     }
642
643     void read_dip_matrix(const char *name) {
644        ifstream file;
```

```
645         file.open(name);
646         for (int i = 0; i < N_Z; i++) {
647       for (int j = 0; j <  N_Z; j++) {
648           file >> zdip_eig[i][j];
649        }
650         }
651         file.close();
652     }
653
654
655      void read_spectrum(const char *name) {
656         ifstream file;
657         file.open(name);
658         for (int i = 0; i < N_Z; i++) {
659        file >> Eigenvalues[i];
660         }
661         file.close();
662     }
663
664 };
665
666
667
668 class HeliumAtomWithCavity {
669 private :
670       typedef double dense_matrix_type;
671       typedef Matrix<dense_matrix_type, Dynamic, Dynamic> MatrixHe;
672       typedef Matrix<dense_matrix_type, Dynamic, 1> VectorHe;
673
674       double Eshift;
675       Lanczos lanczos_diag;
676       vectorg lanczos_eval;
677       int size;
678 public :
679       double Edcz;
680       double By;
681       double Bz;
```

```
682       int Nz;
683       int NL;
684       double dzhe;
685       int Ndzhe;
686       HeliumAtom ha;
687       MatrixHe Hbzby;
688       VectorHe Heval;
689       SparseMatrixXd Hsp;
690
691       HeliumAtomWithCavity(void) {
692       }
693
694
695
696       void find_atom_levels(void) {
697        ha.set_N_Z(Nz);
698        ha.alloc(dzhe, Ndzhe);
699        ha.create_matrix(Edcz, By, 0);
700        ha.diag();
701
702       }
703
704
705
706       void full_diag(void) {
707         SelfAdjointEigenSolver< MatrixHe > eigensolver(Hbzby);
708         if (eigensolver.info() != Success) abort();
709         Heval = eigensolver.eigenvalues();
710         for (int i = 0; i< size;i++) {
711          Heval[i] -= Eshift;
712         }
713       }
714
715        void diag(void) {
716          int niter = 3;
717          int n_found = lanczos_diag.eigenvalues(Hsp, lanczos_eval, niter, 1e
    ↪ }
```

```
718
719     double eval(int i) {
720        return lanczos_eval[i];
721     };
722
723
724      void create_matrix(bool create_dense_matrix = true) {
725       find_atom_levels();
726       Eshift = 0.0;
727       size = NL * Nz;
728       lanczos_eval.resize(size);
729       if (create_dense_matrix) {
730         Hbzby = MatrixHe::Zero(size,size);
731       }
732
733       std::vector< TMatrixXd > coef;
734       coef.reserve(NL * Nz * (2*Nz+1));
735       Hsp.resize(size, size);
736       Hsp.setZero();
737
738
739       for (int ml = 0; ml < NL; ml++) {
740         for (int nz = 0; nz < Nz; nz++) {
741           int s = ml * Nz + nz;
742           coef.push_back( TMatrixXd(s, s, ha.Ez(nz) +
743                 Bz * (double) ml + Eshift)) ;
744           if (create_dense_matrix) {
745            Hbzby(s, s) = ha.Ez(nz) + Bz * (dense_matrix_type) ml +
746                 (dense_matrix_type) Eshift;
747           }
748         }
749       }
750
751       for (int ml = 0; ml < NL-1; ml++) {
752         for (int nz1 = 0; nz1 < Nz; nz1++) {
753           for (int nz2 = 0; nz2 < Nz; nz2++) {
754             int si = ml * Nz + nz1;
```

```
755             int sf = (ml+1) * Nz + nz2;
756             coef.push_back( TMatrixXd(sf, si, By * sqrt(Bz/2.) *
757                 sqrt(ml + 1) * ha.zdip_field(nz1, nz2))) ;
758             coef.push_back( TMatrixXd(si, sf, By * sqrt(Bz/2.) *
759                 sqrt(ml + 1) * ha.zdip_field(nz1, nz2))) ;
760             if (create_dense_matrix) {
761               Hbzby(sf, si) = By * sqrt(Bz/2.) * sqrt(ml + 1) *
762                 ha.zdip_field(nz1, nz2);
763               Hbzby(si, sf) = By * sqrt(Bz/2.) * sqrt(ml + 1) *
764                 ha.zdip_field(nz1, nz2);
765             }
766           }
767         }
768       }
769       Hsp.setFromTriplets(coef.begin(), coef.end());
770
771     }
772 };
```

Bibliography

[1] J. D. Myers and J. Xue, "Organic semiconductors and their applications in photovoltaic devices," *Polymer Reviews*, vol. 52, no. 1, pp. 1–37, 2012.

[2] A. Tsumura, H. Koezuka, and T. Ando, "Macromolecular electronic device: Field-effect transistor with a polythiophene thin film," *Applied Physics Letters*, vol. 49, no. 18, pp. 1210–1212, 1986.

[3] H. Yan, Z. Chen, Y. Zheng, C. Newman, J. R. Quinn, F. Dötz, M. Kastler, and A. Facchetti, "A high-mobility electron-transporting polymer for printed transistors," *Nature*, vol. 457, no. 7230, p. 679, 2009.

[4] C. D. Dimitrakopoulos and P. R. Malenfant, "Organic thin film transistors for large area electronics," *Advanced materials*, vol. 14, no. 2, pp. 99–117, 2002.

[5] J. A. Rogers, Z. Bao, K. Baldwin, A. Dodabalapur, B. Crone, V. Raju, V. Kuck, H. Katz, K. Amundson, J. Ewing *et al.*, "like electronic displays: Large-area rubber-stamped plastic sheets of electronics and microencapsulated electrophoretic inks," *Proceedings of the National Academy of Sciences*, vol. 98, no. 9, pp. 4835–4840, 2001.

[6] G. H. Gelinck, H. E. A. Huitema, E. Van Veenendaal, E. Cantatore, L. Schrijnemakers, J. B. Van Der Putten, T. C. Geuns, M. Beenhakkers, J. B. Giesbers, B.-H. Huisman *et al.*, "Flexible active-matrix displays and shift registers based on solution-processed organic transistors," *Nature materials*, vol. 3, no. 2, p. 106, 2004.

[7] C. Sheraw, L. Zhou, J. Huang, D. Gundlach, T. N. Jackson, M. Kane, I. Hill, M. Hammond, J. Campi, B. Greening *et al.*, "Organic thin-film transistor-driven polymer-dispersed liquid crystal displays on flexible polymeric substrates," *Applied physics letters*, vol. 80, no. 6, pp. 1088–1090, 2002.

[8] D. Voss, "Cheap and cheerful circuits," 2000.

[9] P. Baude, D. Ender, M. Haase, T. Kelley, D. Muyres, and S. Theiss, "Pentacene-based radio-frequency identification circuitry," *Applied Physics Letters*, vol. 82, no. 22, pp. 3964–3966, 2003.

[10] Z.-T. Zhu, J. T. Mason, R. Dieckmann, and G. G. Malliaras, "Humidity sensors based on pentacene thin-film transistors," *Applied Physics Letters*, vol. 81, no. 24, pp. 4643–4645, 2002.

[11] B. Crone, A. Dodabalapur, R. Sarpeshkar, A. Gelperin, H. Katz, and Z. Bao, "Organic oscillator and adaptive amplifier circuits for chemical vapor sensing," *Journal of Applied Physics*, vol. 91, no. 12, pp. 10 140–10 146, 2002.

[12] S. G. Bucella, A. Luzio, E. Gann, L. Thomsen, C. R. McNeill, G. Pace, A. Perinot, Z. Chen, A. Facchetti, and M. Caironi, "Macroscopic and high-throughput printing of aligned nanostructured polymer semiconductors for mhz large-area electronics," *Nature communications*, vol. 6, p. 8394, 2015.

[13] Y. Liang, Y. Jing, S. Gheytani, K.-Y. Lee, P. Liu, A. Facchetti, and Y. Yao, "Universal quinone electrodes for long cycle life aqueous rechargeable batteries," *Nature materials*, vol. 16, no. 8, p. 841, 2017.

[14] H. Alt, H. Binder, A. Köhling, and G. Sandstede, "Investigation into the use of quinone compounds-for battery cathodes," *Electrochimica Acta*, vol. 17, no. 5, pp. 873–887, 1972.

[15] X. Yu, T. J. Marks, and A. Facchetti, "Metal oxides for optoelectronic applications," *Nature materials*, vol. 15, no. 4, p. 383, 2016.

[16] X. Yu, J. Smith, N. Zhou, L. Zeng, P. Guo, Y. Xia, A. Alvarez, S. Aghion, H. Lin, J. Yu *et al.*, "Spray-combustion synthesis: Efficient solution route to high-performance oxide transistors," *Proceedings of the National Academy of Sciences*, vol. 112, no. 11, pp. 3217–3222, 2015.

[17] M. Yilmaz, E. Babur, M. Ozdemir, R. L. Gieseking, Y. Dede, U. Tamer, G. C. Schatz, A. Facchetti, H. Usta, and G. Demirel, "Nanostructured organic semiconductor films for molecular detection with surface-enhanced raman spectroscopy," *Nature materials*, vol. 16, no. 9, p. 918, 2017.

[18] M. Giordani, M. Berto, M. Di Lauro, C. A. Bortolotti, M. Zoli, and F. Biscarini, "Specific dopamine sensing based on short-term plasticity behavior of a whole organic artificial synapse," *ACS sensors*, vol. 2, no. 12, pp. 1756–1760, 2017.

[19] V. F. Curto, B. Marchiori, A. Hama, A.-M. Pappa, M. P. Ferro, M. Braendlein, J. Rivnay, M. Fiocchi, G. G. Malliaras, M. Ramuz *et al.*, "Organic transistor platform with integrated microfluidics for in-line multi-parametric in vitro cell monitoring," *Microsystems & nanoengineering*, vol. 3, p. 17028, 2017.

[20] S. Inal, G. G. Malliaras, and J. Rivnay, "Benchmarking organic mixed conductors for transistors," *Nature communications*, vol. 8, no. 1, p. 1767, 2017.

[21] J. Rivnay, S. Inal, A. Salleo, R. M. Owens, M. Berggren, and G. G. Malliaras, "Organic electrochemical transistors," *Nature Reviews Materials*, vol. 3, no. 2, p. 17086, 2018.

[22] T. Ritz, P. Thalau, J. B. Phillips, R. Wiltschko, and W. Wiltschko, "Resonance effects indicate a radical-pair mechanism for avian magnetic compass," *Nature*, vol. 429, no. 6988, p. 177, 2004.

[23] W. Baker, D. McCamey, K. Van Schooten, J. Lupton, and C. Boehme, "Differentiation between polaron-pair and triplet-exciton polaron spin-dependent mechanisms in organic light-emitting diodes by coherent spin beating," *Physical Review B*, vol. 84, no. 16, p. 165205, 2011.

[24] W. Lubitz, F. Lendzian, and R. Bittl, "Radicals, radical pairs and triplet states in photosynthesis," *Accounts of chemical research*, vol. 35, no. 5, pp. 313–320, 2002.

[25] A. Rao, P. C. Chow, S. Gélinas, C. W. Schlenker, C.-Z. Li, H.-L. Yip, A. K.-Y. Jen, D. S. Ginger, and R. H. Friend, "The role of spin in the kinetic control of recombination in organic photovoltaics," *Nature*, vol. 500, no. 7463, p. 435, 2013.

[26] T. D. Nguyen, E. Ehrenfreund, and Z. V. Vardeny, "Spin-polarized light-emitting diode based on an organic bipolar spin valve," *Science*, vol. 337, no. 6091, pp. 204–209, 2012.

[27] C. Ronda, "Luminescent materials with quantum efficiency larger than 1, status and prospects," *Journal of luminescence*, vol. 100, no. 1-4, pp. 301–305, 2002.

[28] R. T. Wegh, H. Donker, K. D. Oskam, and A. Meijerink, "Visible quantum cutting in ligdf4: Eu3+ through downconversion," *Science*, vol. 283, no. 5402, pp. 663–666, 1999.

[29] P. Vergeer, T. Vlugt, M. Kox, M. Den Hertog, J. Van der Eerden, and A. Meijerink, "Quantum cutting by cooperative energy transfer in yb x y 1- x p o 4: Tb 3+," *Physical Review B*, vol. 71, no. 1, p. 014119, 2005.

[30] A. J. Nozik, M. C. Beard, J. M. Luther, M. Law, R. J. Ellingson, and J. C. Johnson, "Semiconductor quantum dots and quantum dot arrays and applications of multiple exciton generation to third-generation photovoltaic solar cells," *Chemical reviews*, vol. 110, no. 11, pp. 6873–6890, 2010.

[31] S. Singh, W. Jones, W. Siebrand, B. Stoicheff, and W. Schneider, "Laser generation of excitons and fluorescence in anthracene crystals," *The Journal of Chemical Physics*, vol. 42, no. 1, pp. 330–342, 1965.

[32] C. Swenberg and W. Stacy, "Bimolecular radiationless transitions in crystalline tetracene," *Chemical Physics Letters*, vol. 2, no. 5, pp. 327–328, 1968.

[33] H. L. Stern, A. Cheminal, S. R. Yost, K. Broch, S. L. Bayliss, K. Chen, M. Tabachnyk, K. Thorley, N. Greenham, J. M. Hodgkiss *et al.*, "Vibronically coherent ultrafast triplet-pair formation and subsequent thermally activated dissociation control efficient endothermic singlet fission," *Nature chemistry*, vol. 9, no. 12, p. 1205, 2017.

[34] M. B. Smith and J. Michl, "Singlet fission," *Chemical reviews*, vol. 110, no. 11, pp. 6891–6936, 2010.

[35] ——, "Recent advances in singlet fission," *Annual review of physical chemistry*, vol. 64, pp. 361–386, 2013.

[36] G. D. Scholes, "Correlated pair states formed by singlet fission and exciton–exciton annihilation," *The Journal of Physical Chemistry A*, vol. 119, no. 51, pp. 12 699–12 705, 2015.

[37] R. D. Pensack, E. E. Ostroumov, A. J. Tilley, S. Mazza, C. Grieco, K. J. Thorley, J. B. Asbury, D. S. Seferos, J. E. Anthony, and G. D. Scholes, "Observation of two triplet-pair intermediates in singlet exciton fission," *The journal of physical chemistry letters*, vol. 7, no. 13, pp. 2370–2375, 2016.

[38] S. L. Bayliss, A. D. Chepelianskii, A. Sepe, B. J. Walker, B. Ehrler, M. J. Bruzek, J. E. Anthony, and N. C. Greenham, "Geminate and nongeminate recombination of triplet excitons formed by singlet fission," *Physical review letters*, vol. 112, no. 23, p. 238701, 2014.

[39] J. J. Burdett, A. M. Müller, D. Gosztola, and C. J. Bardeen, "Excited state dynamics in solid and monomeric tetracene: The roles of superradiance and exciton fission," *The Journal of chemical physics*, vol. 133, no. 14, p. 144506, 2010.

[40] J. C. Johnson, A. J. Nozik, and J. Michl, "High triplet yield from singlet fission in a thin film of 1, 3-diphenylisobenzofuran," *Journal of the American Chemical Society*, vol. 132, no. 46, pp. 16 302–16 303, 2010.

[41] M. W. Wilson, A. Rao, J. Clark, R. S. S. Kumar, D. Brida, G. Cerullo, and R. H. Friend, "Ultrafast dynamics of exciton fission in polycrystalline pentacene," *Journal of the American Chemical Society*, vol. 133, no. 31, pp. 11 830–11 833, 2011.

[42] S. T. Roberts, R. E. McAnally, J. N. Mastron, D. H. Webber, M. T. Whited, R. L. Brutchey, M. E. Thompson, and S. E. Bradforth, "Efficient singlet fission discovered in a disordered acene film," *Journal of the American Chemical Society*, vol. 134, no. 14, pp. 6388–6400, 2012.

[43] C. Wang and M. J. Tauber, "High-yield singlet fission in a zeaxanthin aggregate observed by picosecond resonance raman spectroscopy," *Journal of the American Chemical Society*, vol. 132, no. 40, pp. 13 988–13 991, 2010.

[44] W. Shockley and H. J. Queisser, "Detailed balance limit of efficiency of p-n junction solar cells," *Journal of applied physics*, vol. 32, no. 3, pp. 510–519, 1961.

[45] M. Hanna and A. Nozik, "Solar conversion efficiency of photovoltaic and photoelectrolysis cells with carrier multiplication absorbers," *Journal of Applied Physics*, vol. 100, no. 7, p. 074510, 2006.

[46] M. C. Beard, J. M. Luther, O. E. Semonin, and A. J. Nozik, "Third generation photovoltaics based on multiple exciton generation in quantum confined semiconductors," *Accounts of chemical research*, vol. 46, no. 6, pp. 1252–1260, 2012.

[47] J. Xia, S. N. Sanders, W. Cheng, J. Z. Low, J. Liu, L. M. Campos, and T. Sun, "Singlet fission: Progress and prospects in solar cells," *Advanced Materials*, vol. 29, no. 20, p. 1601652, 2017.

[48] N. Monahan and X.-Y. Zhu, "Charge transfer–mediated singlet fission," *Annual review of physical chemistry*, vol. 66, pp. 601–618, 2015.

[49] W.-L. Chan, M. Ligges, A. Jailaubekov, L. Kaake, L. Miaja-Avila, and X.-Y. Zhu, "Observing the multiexciton state in singlet fission and ensuing ultrafast multielectron transfer," *Science*, vol. 334, no. 6062, pp. 1541–1545, 2011.

[50] W.-L. Chan, M. Ligges, and X. Zhu, "The energy barrier in singlet fission can be overcome through coherent coupling and entropic gain," *Nature chemistry*, vol. 4, no. 10, p. 840, 2012.

[51] W.-L. Chan, T. C. Berkelbach, M. R. Provorse, N. R. Monahan, J. R. Tritsch, M. S. Hybertsen, D. R. Reichman, J. Gao, and X.-Y. Zhu, "The quantum coherent mechanism for singlet fission: Experiment and theory," *Accounts of chemical research*, vol. 46, no. 6, pp. 1321–1329, 2013.

[52] K. Aryanpour, A. Shukla, and S. Mazumdar, "Theory of singlet fission in polyenes, acene crystals, and covalently linked acene dimers," *The Journal of Physical Chemistry C*, vol. 119, no. 13, pp. 6966–6979, 2015.

[53] A. A. Bakulin, S. E. Morgan, T. B. Kehoe, M. W. Wilson, A. W. Chin, D. Zigmantas, D. Egorova, and A. Rao, "Real-time observation of multiexcitonic states in ultrafast singlet fission using coherent 2d electronic spectroscopy," *Nature chemistry*, vol. 8, no. 1, p. 16, 2016.

[54] T. Zeng, R. Hoffmann, and N. Ananth, "The low-lying electronic states of pentacene and their roles in singlet fission," *Journal of the American Chemical Society*, vol. 136, no. 15, pp. 5755–5764, 2014.

[55] J. N. Schrauben, J. L. Ryerson, J. Michl, and J. C. Johnson, "Mechanism of singlet fission in thin films of 1, 3-diphenylisobenzofuran," *Journal of the American Chemical Society*, vol. 136, no. 20, pp. 7363–7373, 2014.

[56] D. N. Congreve, J. Lee, N. J. Thompson, E. Hontz, S. R. Yost, P. D. Reusswig, M. E. Bahlke, S. Reineke, T. Van Voorhis, and M. A. Baldo, "External quantum efficiency above 100% in a singlet-exciton-fission–based organic photovoltaic cell," *Science*, vol. 340, no. 6130, pp. 334–337, 2013.

[57] N. J. Thompson, D. N. Congreve, D. Goldberg, V. M. Menon, and M. A. Baldo, "Slow light enhanced singlet exciton fission solar cells with a 126% yield of electrons per photon," *Applied Physics Letters*, vol. 103, no. 26, p. 244, 2013.

[58] S. Lee, D. Hwang, S. I. Jung, and D. Kim, "Electron transfer from triplet state of tips-pentacene generated by singlet fission processes to ch3nh3pbi3 perovskite," *The journal of physical chemistry letters*, vol. 8, no. 4, pp. 884–888, 2017.

[59] N. J. Davis, J. R. Allardice, J. Xiao, A. J. Petty, N. C. Greenham, J. E. Anthony, and A. Rao, "Singlet fission and triplet transfer to pbs quantum dots in tips-tetracene carboxylic acid ligands," *The journal of physical chemistry letters*, vol. 9, no. 6, pp. 1454–1460, 2018.

[60] J. Allardice, A. Thampi, S. Dowland, J. Xiao, V. Gray, Z. Zhang, P. Budden, A. Petty II, N. J. Davis, N. C. Greenham *et al.*, "Engineering molecular ligand

shells on quantum dots for quantitative harvesting of triplet excitons generated by singlet fission," *Journal of the American Chemical Society*, 2019.

[61] M. Einzinger, T. Wu, J. F. Kompalla, H. L. Smith, C. F. Perkinson, L. Nienhaus, S. Wieghold, D. N. Congreve, A. Kahn, M. G. Bawendi *et al.*, "Sensitization of silicon by singlet exciton fission in tetracene," *Nature*, vol. 571, no. 7763, p. 90, 2019.

[62] B. D. Ravetz, A. B. Pun, E. M. Churchill, D. N. Congreve, T. Rovis, and L. M. Campos, "Photoredox catalysis using infrared light via triplet fusion upconversion," *Nature*, vol. 565, no. 7739, p. 343, 2019.

[63] V. Gray, D. Dzebo, M. Abrahamsson, B. Albinsson, and K. Moth-Poulsen, "Triplet–triplet annihilation photon-upconversion: towards solar energy applications," *Physical Chemistry Chemical Physics*, vol. 16, no. 22, pp. 10 345–10 352, 2014.

[64] Q. Liu, M. Xu, T. Yang, B. Tian, X. Zhang, and F. Li, "Highly photostable near-ir-excitation upconversion nanocapsules based on triplet–triplet annihilation for in vivo bioimaging application," *ACS applied materials & interfaces*, vol. 10, no. 12, pp. 9883–9888, 2018.

[65] G. W. Bryant, "Biexciton binding in quantum boxes," *Physical Review B*, vol. 41, no. 2, p. 1243, 1990.

[66] G. Chen, T. Stievater, E. Batteh, X. Li, D. Steel, D. Gammon, D. Katzer, D. Park, and L. Sham, "Biexciton quantum coherence in a single quantum dot," *Physical review letters*, vol. 88, no. 11, p. 117901, 2002.

[67] Y. Hu, S. Koch, M. Lindberg, N. Peyghambarian, E. Pollock, and F. F. Abraham, "Biexcitons in semiconductor quantum dots," *Physical review letters*, vol. 64, no. 15, p. 1805, 1990.

[68] M. A. Baldo, C. Adachi, and S. R. Forrest, "Transient analysis of organic electrophosphorescence. ii. transient analysis of triplet-triplet annihilation," *Physical Review B*, vol. 62, no. 16, p. 10967, 2000.

[69] V. Klimov, D. McBranch, N. Barashkov, and J. Ferraris, "Biexcitons in π-conjugated oligomers: Intensity-dependent femtosecond transient-absorption study," *Physical Review B*, vol. 58, no. 12, p. 7654, 1998.

[70] K. Masui, H. Nakanotani, and C. Adachi, "Analysis of exciton annihilation in high-efficiency sky-blue organic light-emitting diodes with thermally activated delayed fluorescence," *Organic Electronics*, vol. 14, no. 11, pp. 2721–2726, 2013.

[71] T. N. Singh-Rachford and F. N. Castellano, "Photon upconversion based on sensitized triplet–triplet annihilation," *Coordination Chemistry Reviews*, vol. 254, no. 21-22, pp. 2560–2573, 2010.

[72] M. J. Tayebjee, S. N. Sanders, E. Kumarasamy, L. M. Campos, M. Y. Sfeir, and D. R. McCamey, "Quintet multiexciton dynamics in singlet fission," *Nature Physics*, vol. 13, no. 2, p. 182, 2017.

[73] L. R. Weiss, S. L. Bayliss, F. Kraffert, K. J. Thorley, J. E. Anthony, R. Bittl, R. H. Friend, A. Rao, N. C. Greenham, and J. Behrends, "Strongly exchange-coupled triplet pairs in an organic semiconductor," *Nature Physics*, vol. 13, no. 2, p. 176, 2017.

[74] D. Lubert-Perquel, E. Salvadori, M. Dyson, P. N. Stavrinou, R. Montis, H. Nagashima, Y. Kobori, S. Heutz, and C. W. Kay, "Multiple quintets via singlet fission in ordered films at room temperature," *arXiv preprint arXiv:1801.00603*, 2018.

[75] D. Kondakov, T. Pawlik, T. Hatwar, and J. Spindler, "Triplet annihilation exceeding spin statistical limit in highly efficient fluorescent organic light-emitting diodes," *Journal of Applied Physics*, vol. 106, no. 12, p. 124510, 2009.

[76] B. Dick and B. Nickel, "Accessibility of the lowest quintet state of organic molecules through triplet-triplet annihilation; an indo ci study," *Chemical Physics*, vol. 78, no. 1, pp. 1–16, 1983.

[77] E. Zavoisky, "Spin-magnetic resonance in paramagnetics," *J. Phys USSR*, vol. 9, pp. 211–245, 1945.

[78] H. Zhang, C. Belvin, W. Li, J. Wang, J. Wainwright, R. Berg, and J. Bridger, "Little bits of diamond: Optically detected magnetic resonance of nitrogen-vacancy centers," *American Journal of Physics*, vol. 86, no. 3, pp. 225–236, 2018.

[79] A. Gruber, A. Dräbenstedt, C. Tietz, L. Fleury, J. Wrachtrup, and C. Von Borczyskowski, "Scanning confocal optical microscopy and magnetic resonance on single defect centers," *Science*, vol. 276, no. 5321, pp. 2012–2014, 1997.

[80] R. Hanson, L. P. Kouwenhoven, J. R. Petta, S. Tarucha, and L. M. Vandersypen, "Spins in few-electron quantum dots," *Reviews of modern physics*, vol. 79, no. 4, p. 1217, 2007.

[81] L. I. Childress, *Coherent manipulation of single quantum systems in the solid state*, 2007, vol. 68, no. 05.

[82] L. Childress, R. Walsworth, and M. Lukin, "Atom-like crystal defects," *Physics Today*, vol. 67, no. 10, p. 38, 2014.

[83] T. D. Ladd, F. Jelezko, R. Laflamme, Y. Nakamura, C. Monroe, and J. L. O'Brien, "Quantum computers," *nature*, vol. 464, no. 7285, p. 45, 2010.

[84] Y. Doi, T. Makino, H. Kato, D. Takeuchi, M. Ogura, H. Okushi, H. Morishita, T. Tashima, S. Miwa, S. Yamasaki *et al.*, "Deterministic electrical charge-state initialization of single nitrogen-vacancy center in diamond," *Physical Review X*, vol. 4, no. 1, p. 011057, 2014.

[85] J. Maze, P. L. Stanwix, J. Hodges, S. Hong, J. Taylor, P. Cappellaro, L. Jiang, M. G. Dutt, E. Togan, A. Zibrov *et al.*, "Nanoscale magnetic sensing with an individual electronic spin in diamond," *Nature*, vol. 455, no. 7213, p. 644, 2008.

[86] G. Balasubramanian, I. Chan, R. Kolesov, M. Al-Hmoud, J. Tisler, C. Shin, C. Kim, A. Wojcik, P. R. Hemmer, A. Krueger *et al.*, "Nanoscale imaging magnetometry with diamond spins under ambient conditions," *Nature*, vol. 455, no. 7213, p. 648, 2008.

[87] R. Schirhagl, K. Chang, M. Loretz, and C. L. Degen, "Nitrogen-vacancy centers in diamond: nanoscale sensors for physics and biology," *Annual review of physical chemistry*, vol. 65, pp. 83–105, 2014.

[88] J. Köhler, J. Disselhorst, M. Donckers, E. Groenen, J. Schmidt, and W. Moerner, "Magnetic resonance of a single molecular spin," *Nature*, vol. 363, no. 6426, p. 242, 1993.

[89] J.-M. Spaeth, J. R. Niklas, and R. H. Bartram, *Structural analysis of point defects in solids: an introduction to multiple magnetic resonance spectroscopy.* Springer Science & Business Media, 2012, vol. 43.

[90] M. W. Doherty, N. B. Manson, P. Delaney, F. Jelezko, J. Wrachtrup, and L. C. Hollenberg, "The nitrogen-vacancy colour centre in diamond," *Physics Reports*, vol. 528, no. 1, pp. 1–45, 2013.

[91] K. Jeong, A. J. Parker, R. H. Page, A. Pines, C. C. Vassiliou, and J. P. King, "Understanding the magnetic resonance spectrum of nitrogen vacancy centers in an ensemble of randomly oriented nanodiamonds," *The Journal of Physical Chemistry C*, vol. 121, no. 38, pp. 21 057–21 061, 2017.

[92] V. Dyakonov, G. Rösler, M. Schwoerer, and E. Frankevich, "Evidence for triplet interchain polaron pairs and their transformations in polyphenylenevinylene," *Physical Review B*, vol. 56, no. 7, p. 3852, 1997.

[93] A. Benfredj, F. Henia, L. Hachani, S. Romdhane, and H. Bouchriha, "Theoretical and experimental study of dynamic triplet-triplet annihilation in an organic one-dimensional motion system," *Phys. Rev. B*, vol. 71, p. 075205, Feb 2005. [Online]. Available: https://link.aps.org/doi/10.1103/PhysRevB.71.075205

[94] L. Hachani, A. Benfredj, S. Romdhane, M. Mejatty, J. L. Monge, and H. Bouchriha, "Fluorescence-detected magnetic resonance in organic systems: A pair-density matrix formalism approach," *Phys. Rev. B*, vol. 77, p. 035212, Jan 2008. [Online]. Available: https://link.aps.org/doi/10.1103/PhysRevB.77.035212

[95] D. Stich, F. Späth, H. Kraus, A. Sperlich, V. Dyakonov, and T. Hertel, "Triplet–triplet exciton dynamics in single-walled carbon nanotubes," *Nature Photonics*, vol. 8, no. 2, p. 139, 2014.

[96] M. Cai, Y. Chen, J. Shinar, O. Mitrofanov, C. Kloc, and A. P. Ramirez, "Photoluminescence-detected magnetic resonance (pldmr) study of rubrene and oxygen-doped rubrene films and powders," in *Organic Light Emitting Materials and Devices XIII*, vol. 7415. International Society for Optics and Photonics, 2009, p. 74151Y.

[97] A. A. Bakulin, D. S. Martyanov, D. Y. Paraschuk, M. S. Pshenichnikov, and P. H. van Loosdrecht, "Ultrafast charge photogeneration dynamics in ground-state charge-transfer complexes based on conjugated polymers," *The Journal of Physical Chemistry B*, vol. 112, no. 44, pp. 13 730–13 737, 2008.

[98] V. Gulbinas, D. Hertel, A. Yartsev, and V. Sundström, "Charge carrier photogeneration and recombination in ladder-type poly (para-phenylene): Interplay between impurities and external electric field," *Physical Review B*, vol. 76, no. 23, p. 235203, 2007.

[99] S. De, T. Pascher, M. Maiti, K. G. Jespersen, T. Kesti, F. Zhang, O. Inganäs, A. Yartsev, and V. Sundström, "Geminate charge recombination in alternating polyfluorene copolymer/fullerene blends," *Journal of the American Chemical Society*, vol. 129, no. 27, pp. 8466–8472, 2007.

[100] S. L. Bayliss, K. J. Thorley, J. E. Anthony, H. Bouchiat, N. C. Greenham, and A. D. Chepelianskii, "Localization length scales of triplet excitons in singlet fission materials," *Physical Review B*, vol. 92, no. 11, p. 115432, 2015.

[101] D. Eaton, S. Parkin, and J. Anthony, "Ccdc 962667: Experimental crystal structure determination," 2013.

[102] C. F. Macrae, P. R. Edgington, P. McCabe, E. Pidcock, G. P. Shields, R. Taylor, M. Towler, and J. Streek, "Mercury: visualization and analysis of crystal structures," *Journal of Applied Crystallography*, vol. 39, no. 3, pp. 453–457, 2006.

[103] W. R. Inc., "Mathematica, Version 11.3," champaign, IL, 2018.

[104] S. L. Bayliss, L. R. Weiss, A. Mitioglu, K. Galkowski, Z. Yang, K. Yunusova, A. Surrente, K. J. Thorley, J. Behrends, R. Bittl *et al.*, "Site-selective measurement of coupled spin pairs in an organic semiconductor," *Proceedings of the National Academy of Sciences*, vol. 115, no. 20, pp. 5077–5082, 2018.

[105] A. Schweiger and G. Jeschke, *Principles of pulse electron paramagnetic resonance*. Oxford University Press on Demand, 2001.

[106] T. Keevers and D. McCamey, "Theory of triplet-triplet annihilation in optically detected magnetic resonance," *Physical Review B*, vol. 93, no. 4, p. 045210, 2016.

[107] M. Wakasa, M. Kaise, T. Yago, R. Katoh, Y. Wakikawa, and T. Ikoma, "What can be learned from magnetic field effects on singlet fission: Role of exchange interaction in excited triplet pairs," *The Journal of Physical Chemistry C*, vol. 119, no. 46, pp. 25 840–25 844, 2015.

[108] T. Yago, K. Ishikawa, R. Katoh, and M. Wakasa, "Magnetic field effects on triplet pair generated by singlet fission in an organic crystal: Application of radical pair model to triplet pair," *The Journal of Physical Chemistry C*, vol. 120, no. 49, pp. 27 858–27 870, 2016.

[109] S. L. Bayliss, L. R. Weiss, A. Rao, R. H. Friend, A. D. Chepelianskii, and N. C. Greenham, "Spin signatures of exchange-coupled triplet pairs formed by singlet fission," *Physical Review B*, vol. 94, no. 4, p. 045204, 2016.

[110] M. Chen, M. D. Krzyaniak, J. N. Nelson, Y. J. Bae, S. M. Harvey, R. D. Schaller, R. M. Young, and M. R. Wasielewski, "Quintet-triplet mixing determines the fate of the multiexciton state produced by singlet fission in a terrylenediimide dimer at room temperature," *Proceedings of the National Academy of Sciences*, vol. 116, no. 17, pp. 8178–8183, 2019.

[111] M. Oxborrow, J. D. Breeze, and N. M. Alford, "Room-temperature solid-state maser," *Nature*, vol. 488, no. 7411, p. 353, 2012.

[112] S. Bogatko, P. D. Haynes, J. Sathian, J. Wade, J.-S. Kim, K.-J. Tan, J. Breeze, E. Salvadori, A. Horsfield, and M. Oxborrow, "Molecular design of a room-temperature maser," *The Journal of Physical Chemistry C*, vol. 120, no. 15, pp. 8251–8260, 2016.

[113] E. Wigner, "On the interaction of electrons in metals," *Physical Review*, vol. 46, no. 11, p. 1002, 1934.

[114] A. Radzvilavičius and E. Anisimovas, "Topological defect motifs in two-dimensional coulomb clusters," *Journal of Physics: Condensed Matter*, vol. 23, no. 38, p. 385301, 2011.

[115] Y. P. Monarkha and V. Shikin, "Theory of a two-dimensional wigner crystal of surface electrons in helium," *Zh. Eksp. Teor. Fiz*, vol. 68, pp. 1423–1433, 1975.

[116] V. Shikin, "Excitation of capillary waves in helium by a wigner lattice of surface electrons," *ZhETF Pisma Redaktsiiu*, vol. 19, p. 647, 1974.

[117] R. Crandall and R. Williams, "Properties of electron surface states on liquid helium," *Physical Review A*, vol. 5, no. 5, p. 2183, 1972.

[118] C. C. Grimes and G. Adams, "Evidence for a liquid-to-crystal phase transition in a classical, two-dimensional sheet of electrons," *Phys. Rev. Lett.*, vol. 42, pp. 795–798, Mar 1979. [Online]. Available: https://link.aps.org/doi/10.1103/PhysRevLett.42.795

[119] K. Shirahama and K. Kono, "Sliding wigner solid on liquid 4 he," *Journal of low temperature physics*, vol. 104, no. 3-4, pp. 237–264, 1996.

[120] L. Schubnikow and W. De Haas, "A new phenomenon in the change of resistance in a magnetic field of single crystals of bismuth," *Nature*, vol. 126, no. 3179, p. 500, 1930.

[121] L. Landau, "Diamagnetismus der metalle," *Zeitschrift für Physik*, vol. 64, no. 9-10, pp. 629–637, 1930.

[122] A. Gladun and V. RYZHY, "Mechanisms of absolute negative conductivity of thin films in a transverse quantized magnetic field," *Zh. Eksp. Teor. Fiz*, vol. 978, p. 982, 1969.

[123] V. Ryzhii, "Microwave-induced anisotropy of conductivity of semiconductors in quantizing magnetic fields," *Sov. Phys. Solid State*, vol. 11, no. 2078, pp. 125 415–15, 1970.

[124] A. Gladun and V. Ryzhii, "Instability in optically—pumped semiconductors in strong magnetic fields," *JETP*, vol. 19, p. 559, 1970.

[125] ——, "Zhetf 57, 978 (1969) sov. phys," *JETP*, vol. 30, p. 534, 1970.

[126] M. Zudov, R. Du, J. Simmons, and J. Reno, "Shubnikov–de haas-like oscillations in millimeterwave photoconductivity in a high-mobility two-dimensional electron gas," *Physical Review B*, vol. 64, no. 20, p. 201311, 2001.

[127] I. Dmitriev, A. Mirlin, D. Polyakov, and M. Zudov, "Nonequilibrium phenomena in high landau levels," *Reviews of Modern Physics*, vol. 84, no. 4, p. 1709, 2012.

[128] A. C. Durst, S. Sachdev, N. Read, and S. Girvin, "Radiation-induced magnetoresistance oscillations in a 2d electron gas," *Physica E: Low-dimensional Systems and Nanostructures*, vol. 20, no. 1-2, pp. 117–122, 2003.

[129] M. Vavilov and I. Aleiner, "Magnetotransport in a two-dimensional electron gas at large filling factors," *Physical Review B*, vol. 69, no. 3, p. 035303, 2004.

[130] I. Dmitriev, A. Mirlin, and D. Polyakov, "Cyclotron-resonance harmonics in the ac response of a 2d electron gas with smooth disorder," *Physical review letters*, vol. 91, no. 22, p. 226802, 2003.

[131] S. I. Dorozhkin, "Giant magnetoresistance oscillations caused by cyclotron resonance harmonics," *Journal of Experimental and Theoretical Physics Letters*, vol. 77, no. 10, pp. 577–581, 2003.

[132] I. Dmitriev, M. Vavilov, I. Aleiner, A. Mirlin, and D. Polyakov, "Theory of microwave-induced oscillations in the magnetoconductivity of a two-dimensional electron gas," *Physical Review B*, vol. 71, no. 11, p. 115316, 2005.

[133] I. Dmitriev, M. Khodas, A. Mirlin, D. Polyakov, and M. Vavilov, "Mechanisms of the microwave photoconductivity in two-dimensional electron systems with mixed disorder," *Physical Review B*, vol. 80, no. 16, p. 165327, 2009.

[134] M. Khodas and M. G. Vavilov, "Effect of microwave radiation on the nonlinear resistivity of a two-dimensional electron gas at large filling factors," *Physical Review B*, vol. 78, no. 24, p. 245319, 2008.

[135] I. Dmitriev, A. Mirlin, and D. Polyakov, "Microwave photoconductivity of a two-dimensional electron gas: Mechanisms and their interplay at high radiation power," *Physical Review B*, vol. 75, no. 24, p. 245320, 2007.

[136] M. Zudov, O. Mironov, Q. Ebner, P. Martin, Q. Shi, and D. Leadley, "Observation of microwave-induced resistance oscillations in a high-mobility two-dimensional hole gas in a strained ge/sige quantum well," *Physical Review B*, vol. 89, no. 12, p. 125401, 2014.

[137] R. Yamashiro, L. Abdurakhimov, A. Badrutdinov, Y. P. Monarkha, and D. Konstantinov, "Photoconductivity response at cyclotron-resonance harmonics in a nondegenerate two-dimensional electron gas on liquid helium," *Physical review letters*, vol. 115, no. 25, p. 256802, 2015.

[138] A. Bogan, A. Hatke, S. Studenikin, A. Sachrajda, M. Zudov, L. Pfeiffer, and K. West, "Microwave-induced resistance oscillations in tilted magnetic fields," *Physical Review B*, vol. 86, no. 23, p. 235305, 2012.

[139] A. Zadorozhko, Y. P. Monarkha, and D. Konstantinov, "Circular-polarization-dependent study of microwave-induced conductivity oscillations in a two-dimensional electron gas on liquid helium," *Physical review letters*, vol. 120, no. 4, p. 046802, 2018.

[140] T. Ye, H.-C. Liu, Z. Wang, W. Wegscheider, and R. G. Mani, "Comparative study of microwave radiation-induced magnetoresistive oscillations induced by circularly-and linearly-polarized photo-excitation," *Scientific reports*, vol. 5, p. 14880, 2015.

[141] E. T. Jaynes and F. W. Cummings, "Comparison of quantum and semiclassical radiation theories with application to the beam maser," *Proceedings of the IEEE*, vol. 51, no. 1, pp. 89–109, 1963.

[142] K. Fujii, "Introduction to the rotating wave approximation (rwa): Two coherent oscillations," *Journal of Modern Physics*, vol. 8, no. 12, p. 2042, 2017.

[143] D. Meekhof, C. Monroe, B. King, W. M. Itano, and D. J. Wineland, "Generation of nonclassical motional states of a trapped atom," *Physical Review Letters*, vol. 76, no. 11, p. 1796, 1996.

[144] M. Brune, F. Schmidt-Kaler, A. Maali, J. Dreyer, E. Hagley, J. Raimond, and S. Haroche, "Quantum rabi oscillation: A direct test of field quantization in a cavity," *Physical review letters*, vol. 76, no. 11, p. 1800, 1996.

[145] S. Haroche, "Nobel lecture: Controlling photons in a box and exploring the quantum to classical boundary," *Rev. Mod. Phys.*, vol. 85, pp. 1083–1102, Jul 2013. [Online]. Available: https://link.aps.org/doi/10.1103/RevModPhys.85.1083

[146] J. I. Cirac and P. Zoller, "Quantum computations with cold trapped ions," *Physical review letters*, vol. 74, no. 20, p. 4091, 1995.

[147] S. R. Jefferts, C. Monroe, E. Bell, and D. J. Wineland, "Coaxial-resonator-driven rf (paul) trap for strong confinement," *Physical Review A*, vol. 51, no. 4, p. 3112, 1995.

[148] D. J. Heinzen and D. Wineland, "Quantum-limited cooling and detection of radio-frequency oscillations by laser-cooled ions," *Physical Review A*, vol. 42, no. 5, p. 2977, 1990.

[149] C. Monroe, D. Meekhof, B. King, S. R. Jefferts, W. M. Itano, D. J. Wineland, and P. Gould, "Resolved-sideband raman cooling of a bound atom to the 3d zero-point energy," *Physical Review Letters*, vol. 75, no. 22, p. 4011, 1995.

[150] D. J. Wineland, "Nobel lecture: Superposition, entanglement, and raising schrödinger's cat," *Reviews of Modern Physics*, vol. 85, no. 3, p. 1103, 2013.

[151] M. Gross, P. Goy, C. Fabre, S. Haroche, and J. Raimond, "Maser oscillation and microwave superradiance in small systems of rydberg atoms," *Physical Review Letters*, vol. 43, no. 5, p. 343, 1979.

[152] J. Rydberg, "K. svenska vetensk akad," 1889.

[153] T. F. Gallagher, *Rydberg atoms*. Cambridge University Press, 2005, vol. 3.

[154] R. G. Hulet and D. Kleppner, "Rydberg atoms in" circular" states," *Physical review letters*, vol. 51, no. 16, p. 1430, 1983.

[155] C. Cohen-Tannoudji, "Théorie quantique du cycle de pompage optique. vérification expérimentale des nouveaux effets prévus," Ph.D. dissertation, 1962.

[156] A. Wallraff, D. I. Schuster, A. Blais, L. Frunzio, R.-S. Huang, J. Majer, S. Kumar, S. M. Girvin, and R. J. Schoelkopf, "Strong coupling of a single photon to a superconducting qubit using circuit quantum electrodynamics," *Nature*, vol. 431, no. 7005, p. 162, 2004.

[157] G. Yang, A. Fragner, G. Koolstra, L. Ocola, D. Czaplewski, R. Schoelkopf, and D. Schuster, "Coupling an ensemble of electrons on superfluid helium to a superconducting circuit," *Physical Review X*, vol. 6, no. 1, p. 011031, 2016.

[158] J. Chen, A. Zadorozhko, and D. Konstantinov, "Strong coupling of a two-dimensional electron ensemble to a single-mode cavity resonator," *Physical Review B*, vol. 98, no. 23, p. 235418, 2018.

[159] A. D. Chepelianskii, M. Watanabe, K. Nasyedkin, K. Kono, and D. Konstantinov, "An incompressible state of a photo-excited electron gas," *Nature communications*, vol. 6, p. 7210, 2015.

[160] Y. Monarkha and K. Kono, *Two-dimensional Coulomb liquids and solids*. Springer Science Business Media, 2013, vol. 142.

[161] M. Lea, P. Fozooni, A. Kristensen, P. Richardson, K. Djerfi, M. Dykman, C. Fang-Yen, and A. Blackburn, "Magnetoconductivity of two-dimensional electrons on liquid helium: Experiments in the fluid phase," *Physical Review B*, vol. 55, no. 24, p. 16280, 1997.

[162] T. Fromhold, L. Eaves, F. Sheard, M. Leadbeater, T. Foster, and P. Main, "Magnetotunneling spectroscopy of a quantum well in the regime of classical chaos," *Physical review letters*, vol. 72, no. 16, p. 2608, 1994.

[163] D. L. Shepelyansky and A. D. Stone, "Chaotic landau level mixing in classical and quantum wells," *Physical review letters*, vol. 74, no. 11, p. 2098, 1995.

[164] G. Boebinger, A. Passner, L. Pfeiffer, and K. West, "Measurement of fermi-surface distortion in double quantum wells from in-plane magnetic fields," *Physical Review B*, vol. 43, no. 15, p. 12673, 1991.

[165] W. Mayer, J. Kanter, J. Shabani, S. Vitkalov, A. Bakarov, and A. Bykov, "Magnetointersubband resistance oscillations in gaas quantum wells placed in a tilted magnetic field," *Physical Review B*, vol. 93, no. 11, p. 115309, 2016.

[166] W. Mayer, S. Vitkalov, and A. Bykov, "Quantum electron transport in magnetically entangled subbands," *Physical Review B*, vol. 96, no. 4, p. 045436, 2017.

[167] P. W. Milonni, "The quantum vacuum: an introduction to quantum electrodynamics," 2013.

[168] M. Dykman, K. Kono, D. Konstantinov, and M. Lea, "Ripplonic lamb shift for electrons on liquid helium," *Physical review letters*, vol. 119, no. 25, p. 256802, 2017.

université PARIS-SACLAY
ÉCOLE DOCTORALE
Physique en Île-de-France (EDPIF)

Titre : Résonance magnétique et spectroscopie de Stark des états liés de Coulomb

Mots clés : spintronique, semiconducteurs organiques, excitons, 2DES, physique atomique, électrodynamique quantique

Résumé : Dans cette thèse, nous présentons l'étude de deux systèmes de nature différente mais dont la physique dans les deux cas est dominée par les interactions coulombiennes: les excitons dans les photoconducteurs organiques dont le spin peut être manipulé par un champ magnétique et les électrons à 2 dimensions sur l'hélium liés à leur charge d'image et dont le moment dipolaire est fortement couplé au champ électrique. Nous montrerons dans les deux cas que des modèles simples de mécanique quantique permettent de bien comprendre leurs propriétés physiques. Cette thèse est divisée en deux parties. Dans la première partie, nous étudions la structure fine des bi-excitons et les aspects géométriques de leur formation dans les semi-conducteurs organiques. Dans la deuxième partie, nous démontrons une nouvelle façon de réaliser un système électrodynamique quantique (QED) d'un atome en interaction avec un oscillateur. En dépit des systèmes physiques différents explorés, les deux sujets sont liés par les méthodes spectroscopiques expérimentales développées dans cette thèse. Les matériaux présentant de la fission d'excitons singlets en deux excitons triplets présentent une grande richesse de phénomènes physiques, liés à la diffusion et l'annihilation, leur couplage par interactions dipolaires et d'échange. Nous présentons ici des études approfondies de la physique du spin du TIPS-tétracène liées à la formation de bi-excitons après la fission de singlets. Nous présenterons des études de couplage intra-triplet. Pour cela, nous avons utilisé la résonance magnétique détectée optiquement, afin de sonder les différentes espèces de spin et de suivre leur évolution en fonction des paramètres physiques pertinents. À partir de ces mesures, nous obtenons l'amplitude du couplage dipolaire magnétique pour les excitations de triplets et de quintets en fonction de la morphologie des échantillons et déterminons ainsi non seulement les orientations des excitons triplets dans les échantillons, mais également la géométrie interne de la formation de bi-excitons à partir de deux excitons de triplets couplés par échange. Ceci nous permet d'identifier spécifiquement les sites moléculaires sur lesquels résident les états du quintet via la corrélation existant entre la structure de spin extraite de manière expérimentale et la structure cristalline moléculaire. Le gaz d'électrons bidimensionnel (2DEG) à la surface de l'hélium liquide est intéressant à la fois pour la recherche fondamentale et les sciences appliquées. Dans les deux cas, il faut pouvoir manipuler le système et le régler avec précision. Nous profitons des caractéristiques extraordinaires de ce système pour réaliser un système fondamental QED, dans lequel un atome interagit avec une cavité électromagnétique. L'utilisation de la haute pureté du 2DEG est en effet une approche originale de la QED avec ses avantages et ses difficultés propres. Nous avons appliqué un champ électrique perpendiculairement à la couche pour confiner les électrons, induisant ainsi une série de niveaux d'énergie de Rydberg, présentant une analogie avec un atome. Un champ magnétique perpendiculaire donne lieu à la formation de niveaux de Landau équidistants - un oscillateur harmonique pour le système QED. Pour coupler l'atome à l'oscillateur, nous avons mélangé les degrés de liberté de mouvement parallèles et transverses au plan des électrons en appliquant un champ magnétique parallèle. Les niveaux d'énergie sont contrôlés à l'aide de mesures de spectroscopie Stark. Afin de décrire ce couplage nous avons utilisé un hamiltonien de type Jaynes-Cummings donnant un accord parfait avec les résultats expérimentaux. Ainsi, nous avons réalisé expérimentalement un couplage entre objets quantiques facilement ajustable via l'intensité du champ magnétique.

Université Paris-Saclay
Espace Technologique / Immeuble Discovery
Route de l'Orme aux Merisiers RD 128 / 91190 Saint-Aubin, France

université PARIS-SACLAY
ÉCOLE DOCTORALE
Physique en île-de-France (EDPIF)

Title : Magnetic resonance and Stark spectroscopy of Coulomb bound states
Keywords : spintronics, organic semiconductors, excitons, 2DES, atomic physics, quantum electrodynamics

Abstract : In this dissertation we present studies of two Coulomb bound systems of very different nature: triplet excitons which are neutral strongly bound states possesing a long lived spin which can addressed by magnetic field and electrons on helium bound to their image charge inside liquid helium owning large dipolar momentum and which are thus sensitive to electric field. In the sense these two systems are complementary and we will show that in both cases simple quantum mechanical models allow to gain a deep insight in the system structure. This Dissertation is divided in two parts. In the first part we investigate bi-exciton fine structure and geometrical aspects of their formation in organic semiconductors. In the second part we demonstrate a new way to realise a quantum electrodynamics system of an atom interacting with an oscillator. Thus we start with rather applied research and then continue with fundamental physics. Despite of very different physical systems explored, both subjects are linked by the experimental spectroscopic methods which we developed. Singlet fission materials exhibit great richness of such phenomena and combine processes and effects occurring in many various physical systems, like photoluminescence, spectral hole burning, excitons formation, diffusion and annihilation, dipolar and exchange coupling, photon up- and down-conversion etc. We present here careful studies of such an intrinsic spin property of TIPS-tetracene as the bi-exciton formation following singlet fission. We focused on two aspects of spin composition in TIPS-tetracene. First, we will present intra-triplet coupling studies. For that we used optically detected magnetic resonance, to probe different spin species and follow their evolution in varying conditions. From those measurements we obtain dipolar coupling parameters for triplet and quintet excitations, examine samples' morphology and determine not only triplet excitons orientations in the samples, but also establish inner geometry of bi-exciton formation by two exchange-coupled triplet excitons - identify specific molecular sites on which quintet (bi-exciton) states reside via correlating experimentally extracted spin structure with the molecular crystal structure. Then another aspect concerns the coupling actually forming a quintet state of two triplets - we present collaborative results on inter-triplet exchange coupling investigated by means of high field magneto-photoluminescence measurements. They allow us to assign certain exchange-coupling strength values to various triplet pairs and specify photoluminescence spectra corresponding to each pair. 2 dimensional electron gas (2DEG) on the liquid helium surface is interesting for fundamental research and applied science at the same time. For both interests one needs to be able to manipulate the system and to tune it finely. We profit from extraordinary characteristics of this system to realise a fundamental quantum electrodynamics (QED) system, in which an atom interacts with an electromagnetic field. Using high purity 2DEG is indeed an original approach to QED with its' proper advantages and difficulties we managed. We applied perpendicular electric field to confine the electrons, thus inducing Rydberg energy levels series, which then plays role of a hydrogen-like atom. Then perpendicular magnetic field quantized the electrons' in-plane motion, resulting in equidistant Landau levels - an oscillator for the QED system. Further to couple the atom to the oscillator we mixed perpendicular and in-plane motion degrees of freedom by applying parallel magnetic field. Energy levels are monitored using Stark spectroscopy measurements. In order to describe this coupling we derived Jaynes-Cummings type Hamiltonian with no fitting parameters and it showed perfect agreement with the experimental results. Thus we realised experimentally coupling between quantum objects easily tunable by the parallel magnetic field strength.

Université Paris-Saclay
Espace Technologique / Immeuble Discovery
Route de l'Orme aux Merisiers RD 128 / 91190 Saint-Aubin, France